

# **Modeling and Analysis of Scalable Arcless Micromechanical Switches for Power Applications**

**THESIS**

Submitted in partial fulfillment  
of the requirements for the degree of  
**DOCTOR OF PHILOSOPHY**

by

**FEMI R**

Under the Supervision of  
**Prof. Shibu Clement**  
and Co-Supervision of  
**Dr. Anita Agrawal**




**BIRLA INSTITUTE OF TECHNOLOGY AND SCIENCE  
PILANI (RAJASTHAN) INDIA**

**2017**

**BIRLA INSTITUTE OF TECHNOLOGY AND SCIENCE**  
**PILANI (RAJASTHAN)**  
**CERTIFICATE**

This is to certify that the thesis entitled “**Modeling and Analysis of Scalable Arcless Micromechanical Switches for Power Applications**” and submitted by **FEMI R**, ID No. **2012PHXF003G** for award of Ph.D. degree of the Institute, embodies original work done by her under my supervision.



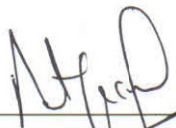
---

Signature of the Supervisor

Name: Prof. SHIBU CLEMENT

Associate Professor (Mechanical Engineering)

Date: 10/05/2017



---

Signature of the Co-Supervisor

Name: Dr. ANITA AGRAWAL

Assistant Professor (Electrical and Electronics Engineering)

Date: 10/05/2017

## ACKNOWLEDGEMENT

With immense pleasure and a deep sense of gratitude, I take this opportunity to thank several outstanding individuals and scholars who guided me throughout the period of my Ph.D. thesis.

First of all I would like to thank Almighty God for granting me the resources – physical, mental, emotional and spiritual – to carry out the work leading to this thesis.

I wish to record my sincere gratitude to my supervisor Prof. Shibu Clement (HOD, Department of Mechanical Engineering) and Co-supervisor Dr. Anita Agrawal (Assistant Professor, Department of EEE) for their guidance, encouragement and support right from the beginning of my thesis. I could achieve my research goals through their valuable suggestions and directions. I express my gratitude to the members of the Doctoral Advisory Committee, Prof. M. K. Deshmukh (HOD, Department of EEE) and Dr. Sachin Waigaonkar, for their guidance and co-operation. I also express my sincere thanks to Dr. Nitin Sharma, Convener, Departmental Research Committee, for his support.

I am extremely grateful to Prof. Souvik Bhattacharyya (Vice Chancellor, BITS- Pilani), Prof. G. Raghurama (Director, BITS-Pilani, K. K. Birla Goa Campus), Prof. Ashwin Srinivasan (Deputy Director, BITS-Pilani, K. K. Birla Goa Campus, Prof. S. K. Verma (Dean, Academic Research Division, BITS, Pilani) and Prof. P. K. Das (Associate Dean, Academic Research Division, BITS, Pilani -K. K. Birla Goa Campus) for providing me the facilities to conduct my research work at BITS-Pilani, K. K. Birla Goa Campus.

I extend my sincere thanks to Prof. K. E Raman, Prof. Sasikumar Punnekkat, Prof. K. R. Anupama, Prof. A. P. Koley, Prof. S.D Manjare, Prof. D.M. Kulkarni, Prof. Sunil Bhand and Dr. Gautam Bacher for their valuable advice, motivation and support at various phases of my work. I am also very thankful to my departmental colleagues for their help and support.

I am also thankful to mechanical engineering and chemical Engineering department colleagues for helping me to use COMSOL multiphysics tool. I express my sincere thanks to Mr. M. R. Iyer and Mr. T. Rajesh from FTD Infocom Pvt. Ltd, Bangalore, for the technical support on Coventor MEMS+. I also express my sincere gratitude to Prof. S. K. Shrivastava

(Co-ordinator), faculty and staff of Centre for Nano Science and Engineering (CeNSE), IISc Bangalore for their support through Indian Nanoelectronics users (INUP) program.

Collective and individual acknowledgements are due to all my colleagues and friends, within and outside of the BITS-Pilani community, who have directly or indirectly helped me in my work. I also thank the large number of persons, family and friends, who have been praying for me through the entire process and whose goodwill and moral support, have kept my morale high.

My husband has been instrumental in motivating me from time to time. I am indebted to him and my daughters for giving me a happy and joyous environment at home and for their silent sacrifices. I would forever be indebted to my parents and parents-in-law for their constant love, confidence, prayers, strong support and good wishes. Also, thanks are due to my brother, brother-in-law, sister-in law whose blessings and good wishes were always with me.

**Femi R**

## ABSTRACT

This thesis presents the modeling and analysis of scalable arcless micromechanical switches for power applications. The proposed switching system consists of Total Cross Tied (TCT) array of electrostatically actuated micromechanical switches, which operates under hot switching condition.

A conceptual model of scalable Total Cross Tied (TCT) array configuration of micromechanical switches has been introduced to enhance higher rating. Performance of mechanical switch, solid-state switch and micromechanical switch array are compared for 400V, 6A DC system and 230V, 6A AC system using MATLAB Simulink and literature data. This provides the voltage, current and power characteristics of the micromechanical switch array. The comparative study shows that the proposed switch array gives better performance in terms of voltage drop, leakage current and power loss. This work identifies four parts of the micromechanical switch at which arc might occur. Driving electrode is one of the arc occurring part, which is supplied with DC voltage. It is a non-touching electrode. Breakdown arc occurs in this electrode, which is due to breakdown voltage and electric field. This work presents breakdown voltage and breakdown electric field based on modified Paschen curve for Al, Cu, Au and Pt materials for the gap between 0.5 $\mu\text{m}$  and 30 $\mu\text{m}$ . This curve provides the boundary between the arc and arcless region. This work proposes to design and analyze arcless driving electrode using mathematical modeling and Finite Element Modeling (FEM) simulations. The electric field distribution across the driving electrode during ON-state and OFF-state of the micromechanical switch are obtained. The influences of contact gap and contact size are also simulated. The arc occurrences for driving electrodes at various voltages are also simulated and results are presented.

Further this work proposes to design arcless microelectrical contact based on electrothermal behavior using mathematical modeling and FEM simulations. The microelectrical contact is a touching electrode which is responsible for allowing and interrupting electric current. This work explores various parameters which are responsible for the ignition of arc. Pre-breakdown and breakdown arc occurs in microelectrical contact which is due to metal vapors and ionization of air gap respectively. The ON-state resistance and current carrying capability of the microelectrical contact are presented for smooth surface and rough surfaces.

Simulation has been carried out to estimate the steady state and transient temperature distributions for the design of arcless microelectrical contact. The OFF-state capacitance and electric field are calculated and simulated for the arcless microelectrical contact. The analysis is carried out for materials such as Al, Cu, Au and Pt. This analysis identifies the voltage, current and power rating of the arcless microelectrical contact.

This work also proposes to design micromechanical switch and analyze its electromechanical performance parameters using mathematical modeling and FEM simulations. The performance characteristics such as spring constant, driving voltage, force, switching speed, capacitance and Q factor are investigated. This work presents the influence of electromechanical parameters in the design of arcless micromechanical switch. The switching characteristics of a single switch with the rating of 12V, 0.2A are obtained. The arcless nature of the switch during hot switching is extensively analyzed. A scalable TCT array of 140V, 3A rating using  $15 \times 12$  switches has been designed. Simulation has been carried out to obtain the switching characteristics of the TCT array using MEMS+ and Cadence virtuoso tools. The results show the feasibility of using TCT array of micromechanical switches for arcless power switching applications.

# TABLE OF CONTENT

ACKNOWLEDGEMENT -----	i
ABSTRACT -----	iii
TABLE OF CONTENT -----	v
LIST OF FIGURES-----	ix
LIST OF TABLES-----	xiv
LIST OF ACRONYMS AND SYMBOLS-----	xv
<b>1. INTRODUCTION</b>	
1.1 Miniaturization -----	1
1.1.1 The third industrial revolution -----	1
1.1.2 Solid-state switches -----	2
1.1.3 Micromechanical switches -----	2
1.2 Micromechanical Switches for Power Applications-----	3
1.3 Arcless Switching -----	4
1.4 Scope for Applications-----	5
1.5 Research Objectives and Scope -----	6
1.6 Organization of Thesis-----	7
<b>2. LITERATURE SURVEY</b>	
2.1 Classification of Switches -----	10
2.1.1 Mechanical switches-----	10
2.1.2 Solid-state switches-----	12
2.1.3 Hybrid switches-----	13
2.1.4 Micromechanical switches-----	14
2.2 Micromechanical Switches for Power Applications-----	15
2.2.1 Challenges -----	16
2.3 Switching Modes -----	16
2.3.1 Cold switching -----	16
2.3.2 Hot switching -----	17
2.4 Modeling and Design Challenges -----	17
2.5 Methodology -----	18
2.6 Simulation Tools -----	19
2.6.1 MATLAB Simulink -----	19
2.6.2 COMSOL Multiphysics -----	20
2.6.3 Coventor MEMS+ -----	21
2.7 Research Gaps in the Literature -----	22
<b>3. CONCEPT OF SCALABLE TOTAL CROSS TIED MICROMECHANICAL SWITCH ARRAY</b>	
3.1 Introduction -----	24
3.2 Characteristic of DC Electrical System -----	25
3.2.1 Mechanical switches -----	26
3.2.2 Solid-state switches -----	28

3.2.3	Solid-state switch array -----	29
3.2.4	Proposed scalable TCT micromechanical switch array configuration -----	31
3.2.5	Comparative analysis of switches in DC system -----	34
3.3	Characteristics of AC System -----	35
3.3.1	Mechanical switch -----	36
3.3.2	Solid-state switch -----	37
3.3.3	Proposed scalable TCT micromechanical switch array -	38
3.3.4	Comparative analysis of switches in AC system -----	40
3.4	Actuation Techniques of Micromechanical Switch for Power Applications -----	41
3.4.1	Piezoelectric micromechanical switches -----	41
3.4.2	Thermally actuated micromechanical switches -----	41
3.4.3	Electromagnetic micromechanical switches -----	41
3.4.4	Electrostatic micromechanical switches -----	42
3.5	Proposed Electrostatically Actuated Micromechanical Switch -----	43
3.6	Arcless Switching -----	45
3.6.1	DC power switching -----	45
3.6.2	Arc occurring parts -----	46
3.7	Conclusions-----	47
<b>4.</b>	<b>MODELING AND ANALYSIS OF ARCLESS DRIVING ELECTRODE</b>	
4.1	Introduction -----	48
4.2	Structure of the Driving Electrode-----	49
4.3	Breakdown Arc Analysis -----	50
4.3.1	Breakdown arc analysis using Paschen curve -----	51
4.3.2	Breakdown arc analysis using modified Paschen curve -	52
4.3.3	Analysis of breakdown electric field as a function of electrode gap -----	55
4.4	Arc Analysis During OFF-State -----	56
4.4.1	Mathematical Modeling -----	56
4.4.2	Simulation -----	57
4.4.3	Effect of Voltage -----	61
4.5	Arc Analysis During ON-State -----	63
4.6	Discussion on Breakdown Arc -----	65
4.7	Conclusion -----	70
<b>5.</b>	<b>MODELING AND ANALYSIS OF ARCLESS MICROELECTRICAL CONTACT</b>	
5.1	Introduction -----	71
5.2	Structure of Microelectrical Contact -----	72
5.3	ON-State -----	74
5.3.1	Contact resistance -----	74
5.3.2	Effect of force on contact resistance -----	77
5.3.3	Effect of temperature on contact resistance -----	80
5.3.4	Current carrying capability -----	81
5.3.5	Contact voltage drop -----	87



5.4	Switching State -----	89
5.4.1	Steady state temperature -----	89
5.4.2	Transient temperature -----	90
5.5	OFF-State -----	92
5.5.1	OFF-state capacitance -----	92
5.5.2	Electric Field -----	94
5.6	Discussion on Contact Welding and Arc Occurrence -----	96
5.7	Conclusions-----	99
<b>6.</b>	<b>ELECTROMECHANICAL MODELING AND ANALYSIS OF ARCLESS MICROMECHANICAL SWITCHES</b>	
6.1	Introduction -----	101
6.2	Structural Design of Electrostatically Actuated Micromechanical Switches -----	102
6.2.1	Structure of electrostatically actuated micromechanical switch -----	103
6.2.2	Mathematical modeling -----	103
6.2.3	FEM modeling -----	105
6.2.4	Performance analysis -----	107
6.3	Effect of Q Factor -----	112
6.3.1	Deformation of the beam -----	113
6.3.2	Under-damped system -----	114
6.4	Switching Characteristics of a Micromechanical Switch -----	115
6.4.1	Transition of switch from OFF-state to ON-state -----	116
6.4.2	Transition of switch from ON-state to OFF-state -----	117
6.5	Arcless Switching of Micromechanical Switch -----	118
6.5.1	Arc analysis for the gap between driving electrodes -----	119
6.5.2	Arc analysis for the microelectrical contact -----	119
6.5.3	Arc analysis for the gap between anode and cathode ----	120
6.5.4	Arc analysis for the gap between driving electrode and anode -----	121
6.6	Switching characteristics of Scalable TCT array of Micromechanical Switches -----	121
6.6.1	Transition of TCT array from OFF-state to ON-state -----	123
6.6.2	Transition of TCT array from ON-state to OFF-state -----	123
6.6.3	Resistance of TCT array of micromechanical switches --	124
6.6.4	Scalability -----	125
6.7	Conclusion-----	126
<b>7.</b>	<b>CONCLUSIONS AND SCOPE FOR FUTURE WORK</b>	
7.1	Conclusions -----	128
7.2	Contributions of the Thesis-----	129
7.3	Limitations and Future Work-----	130
	<b>REFERENCES -----</b>	<b>131</b>

<b>APPENDIX A</b> -----	150
<b>APPENDIX B</b> -----	151
<b>APPENDIX C</b> -----	154
<b>APPENDIX D</b> -----	155
<b>APPENDIX E</b> -----	155
<b>APPENDIX F</b> -----	156
<b>LIST OF PUBLICATIONS</b> -----	158
<b>BRIEF BIOGRAPHY OF CANDIDATE AND SUPERVISOR</b> -----	160

## LIST OF FIGURES

<i><b>FIG No.</b></i>	<i><b>CAPTION</b></i>	<i><b>PAGE No.</b></i>
1.1	A die containing 400 micromechanical switches on the top of a US dime...	4
1.2	Micromechanical switch turning ON incandescent light bulb .....	4
3.1	Equivalent DC electrical system .....	25
3.2	DC system with mechanical switch .....	27
3.3	Simulated waveforms of DC system with mechanical switch .....	27
3.4	DC system with solid-state switch .....	28
3.5	Simulated waveforms of DC system with power MOSFET switch .....	28
3.6	DC system with solid-state switch array .....	29
3.7	Simulated waveforms of DC system with array of solid-state switch .....	30
3.8	DC system with scalable TCT $m \times n$ array configuration of micromechanical switches .....	32
3.9	Simulated waveforms of DC system with TCT array of micromechanical switch configuration .....	33
3.10	AC equivalent electrical system .....	35
3.11	Simulated waveforms of AC system with mechanical switch .....	37
3.12	AC system with GTO switch .....	37
3.13	Simulated waveforms of AC system with solid-state switch .....	38
3.14	Simulated waveforms of AC system with TCT array of micromechanical switch configuration .....	39

<b>3.15</b>	Electrostatically actuated micromechanical switch .....	44
<b>4.1</b>	Driving electrode during (a) OFF-state (b) ON-state .....	49
<b>4.2</b>	Paschen curve .....	51
<b>4.3</b>	Modified Paschen curve for the materials Al, Cu, Au and Pt .....	54
<b>4.4</b>	Breakdown electric field as a function of electrode gap .....	55
<b>4.5</b>	Capacitance of the driving electrode (a) Case 1: $L_d = 30\mu\text{m}$ , $W_d = 30\mu\text{m}$ , $t_d = 2\mu\text{m}$ , (b) Case 2: $L_d = 30\mu\text{m}$ , $W_d = 60\mu\text{m}$ , $t_d = 5\mu\text{m}$ (c) Case 3: $L_d = 50\mu\text{m}$ , $W_d = 50\mu\text{m}$ , $t_d = 10\mu\text{m}$ .....	58
<b>4.6</b>	Electric field across the driving electrodes (a) Case 1: $L_d = 30\mu\text{m}$ , $W_d = 30\mu\text{m}$ , $t_d = 2\mu\text{m}$ , (b) Case 2: $L_d = 30\mu\text{m}$ , $W_d = 60\mu\text{m}$ , $t_d = 5\mu\text{m}$ (c) Case 3: $L_d = 50\mu\text{m}$ , $W_d = 50\mu\text{m}$ , $t_d = 10\mu\text{m}$ .....	59
<b>4.7</b>	OFF-state FEM analysis (a) surface plot of capacitance (b) surface plot of voltage (c) slice plot of voltage (d) slice plot of electric field .....	60
<b>4.8</b>	Variations in electrode gap and voltage for the range A .....	61
<b>4.9</b>	Arc analysis during OFF-state for (a) case 1 (b) case 2 and (c) case 3 .....	63
<b>4.10</b>	ON-state FEM analysis results (a) surface plot of capacitance (b) surface plot of voltage (c) surface plot of voltage (c) surface plot of electric field..	65
<b>4.11</b>	Arc analysis during OFF-state using modified Paschen curve for 50V, 250V and 400V at $8\mu\text{m}$ .....	66
<b>4.12</b>	Arc analysis during OFF-state using breakdown electric field for 50V, 250V and 400V at $8\mu\text{m}$ .....	67
<b>4.13</b>	Arc analysis for 50V, 250V and 400V during ON-state .....	68

<b>4.15</b>	Arc analysis during ON-state for 50V, 250V and 400V using breakdown electric field .....	69
<b>5.1</b>	Structure of 3D microelectrical contact .....	72
<b>5.2</b>	Various states of the microelectrical contact .....	74
<b>5.3</b>	(a) ON-state microelectrical contact with smooth surface (b) Equivalent circuit model .....	75
<b>5.4</b>	Microelectrical contact with rough surface .....	76
<b>5.5</b>	Surface plot for resistance of Al contact (a) smooth surface (b) rough Surface .....	77
<b>5.6</b>	Radius of contact spot as a function of force .....	78
<b>5.7</b>	FEM Surface plot for Al microelectrical contact (a) at $F = 0 \mu\text{N}$ (b) structure deformation at $F = 130 \mu\text{N}$ (c) 2D surface plot (d) 3D surface plot .....	79
<b>5.8</b>	Force and contact resistance relationship .....	79
<b>5.9</b>	Temperature-resistance relationship and temperature-radius relationship of contact spot for (a) Al (b) Cu (c) Au and (d) Pt .....	80
<b>5.10</b>	ON-state anode temperature of the microelectrical contact with smooth surface for (a) Al (b) Cu (c) Au and (d) Pt .....	82
<b>5.11</b>	Simulation results of ON-state temperature of the microelectrical contact with smooth surface with the material properties as a function of temperature for (a) Al (b) Cu (c) Au and (d) Pt .....	83
<b>5.12</b>	Surface plot of temperature distribution for Al .....	84
<b>5.13</b>	Simulation results of ON-state anode temperature of the microelectrical	

	contact with rough surface for (a) Al (b) Cu (c) Au and (d) Pt .....	85
<b>5.14</b>	COMSOL surface plots of temperature flow directions of the microelectrical contact (a) with smooth surface (b) with rough surface .....	85
<b>5.15</b>	Surface plots of temperature distribution for rough surface (a) full view (b) projected view of contact area .....	86
<b>5.16</b>	(a) Current- voltage drop and current -resistance relationship for Al (b) voltage drop-temperature relationship for Al .....	88
<b>5.17</b>	FEM surface plot for voltage drop .....	89
<b>5.18</b>	Power- temperature relationship for (a)Al (b)Cu (c)Au and (d)Pt .....	90
<b>5.19</b>	Transient temperature for various power levels (a) Al (b) Cu (c) Au (d) Pt..	91
<b>5.20</b>	Temperature distribution for Al at (a) 0s (b) 5 $\mu$ s (c) 10 $\mu$ s (d) 35 $\mu$ s .....	92
<b>5.21</b>	(a) OFF-state microelectrical contact (b) Equivalent capacitance .....	93
<b>5.22</b>	OFF-state capacitance .....	94
<b>5.23</b>	OFF-state electric field .....	95
<b>5.24</b>	OFF-state FEM analysis results (a) surface plot of capacitance (b) surface plot of voltage (c) slice plot of voltage and slice plot of electric field .....	96
<b>6.1</b>	Micromechanical switch (a) side view (b) top view .....	103
<b>6.2</b>	Schematic of the micromechanical switch designed using MEMS+ .....	106
<b>6.3</b>	Mechanical movements of the micromechanical switch with respect to driving voltage .....	108
<b>6.4</b>	Deflection of point A, B and C with respect to driving voltage .....	109
<b>6.5</b>	Voltage across the driving electrode, deflection of point A, B and C with	

	respect to time .....	109
<b>6.6</b>	Transient switching states of the switch .....	110
<b>6.7</b>	Force with respect to voltage across driving electrodes .....	110
<b>6.8</b>	Capacitance with respect to voltage across the driving electrodes .....	111
<b>6.9</b>	Capacitance with respect to time .....	112
<b>6.10</b>	Deformation of beam for case X .....	113
<b>6.11</b>	Driving voltage and beam deflection with respect to time for case Y .....	114
<b>6.12</b>	Schematic of equivalent DC electrical system with the micromechanical switch .....	115
<b>6.13</b>	Transient switching from OFF-state to ON-state characteristics under load Condition (a) Voltage and current (b) Power .....	116
<b>6.14</b>	Transient switching from ON-state to OFF-state characteristics under load Condition (a) Voltage and current (b) Power.....	118
<b>6.15</b>	Schematic of TCT array of 15×12 micromechanical switches .....	122
<b>6.16</b>	Electrical circuit with micromechanical switch array .....	122
<b>6.17</b>	Transient switching of array from OFF-state to ON-state characteristics under load Condition .....	123
<b>6.18</b>	Transient switching of array from ON-state to OFF-state characteristics under load Condition .....	124
<b>F.1</b>	Mesh structure of 3D microelectrical contact .....	157

## LIST OF TABLES

<i>TABLE NO.</i>	<i>CAPTION</i>	<i>PAGE NO.</i>
3.1	Parameters of DC equivalent system .....	26
3.2	Simulation results and quantitative comparison for DC system .....	35
3.3	Parameters of AC system .....	36
3.4	Simulation results and quantitative comparison for AC system .....	40
3.5	Comparison of micromechanical switches on the basis of actuation technique .....	43
4.1	Capacitance and electric field during ON-state .....	64
4.2	Occurrence of arc during OFF-state .....	67
4.3	Electric field and arc occurrence during ON-state .....	69
5.1	ON-state resistance of the microelectrical contact .....	76
5.2	Time lag to reach melting and boiling temperature .....	91
5.3	Occurrence of arc due to various mechanism .....	98
6.1	Fabrication process step input used for MEMS+ simulations .....	106
6.2	Performance parameters .....	107
6.3	Switching speed and force with respect to voltage across the driving Electrodes.....	111
6.4	Performance parameters for case X and case Y .....	113
6.5	Comparison of Micromechanical switch with Mechanical, Semiconductor and RF switches .....	125



## LIST OF ACRONYMS AND SYMBOLS

2D	Two Dimensional
3D	Three Dimensional
AC	Alternating Current
BJT	Bipolar Junction Transistor
CMOS	Complementary Metal Oxide Semiconductor
DC	Direct Current
ESD	Electrostatic Discharge
FEM	Finite Element Method
FPGA	Field Programmable Gate Array
GTO	Gate Turn OFF Thyristor
HVAC	High Voltage Alternating Current
HVDC	High Voltage Direct Current
IC	Integrated Circuits
IGBT	Insulated Gate Bipolar Transistor
IGCT	Integrated Gate-Commutated Thyristor
MCT	MOS Controlled Thyristor
MOSFET	Metal Oxide Field Effect Transistor
NR	Not Reaching
Q	Quality factor
RF	Radio Frequency
SoC	System on Chip
SP	Series Parallel
TCT	Total Cross Tied
VLSI	Very Large Scale Integrated Circuits
YBCO	Yttrium Barium copper Oxide
K	Kelvin
A	Ampere
mA	Milliampere
nA	Nanoampere
V	Volt
W	Watt
mW	Milliwatt
$\mu$ s	Microsecond
ms	Millisecond
$\mu$ m	Micrometer
mm	Millimeter
$\mu$ N	Micronewton
F	Fared

H	Henry
$\Omega$	Ohm
m $\Omega$	Milliohm
ns	Nanosecond
rms	Root Mean Square
$E_s$	Voltage source
$R$	Resistance
$L$	Inductance
$R_L$	Load resistance
$i$	Current flowing through the circuit
$V_{sw}$	Switch voltage.
$V_L$	Load voltage
$i_L$	Load current
$t$	time
$i_{sw}$	Current flowing through the switch
$P_{sw}$	Power loss across the switch
$V_{swa}$	Voltage across the switch array
$V_j$	Voltage across each column switches.
$P_{swa}$	Power rating of the switch array
$E_m$	Maximum source voltage
$\omega$	Angular frequency
$g_d$	Gap between the driving electrodes
$L_d$	Length of driving electrode
$t_d$	Thickness
$W_d$	Width of the driving electrode
$g_{d1}$	Gap between the driving electrodes
$g_{d2}$	Gap between the driving electrodes
$p$	Pressure
$g$	Gap
$V_b$	Breakdown voltage
$j_{sec}$	Secondary emission current
$j_{ion}$	Incident ion current
$\gamma_i$	Townsend's second ionization coefficient
$\gamma_{eff}$	Effective secondary emission coefficient
$j_{sec}$	Secondary emission current
$j_{fld}$	Enhanced field emission current

$\gamma_{net}$	Net effective secondary emission coefficient
$C_d$	Capacitance of the driving electrode
$\epsilon_0$	Permittivity of air
$k$	Relative permittivity of air
$C_{df}$	Fringing field due to the finite dimensions of the electrodes
$C_{dft}$	Fringing field associated with the thickness of the electrical contacts
$Q_d$	Charge on the driving electrode
$E_d$	Electric field between the driving electrodes
$L_{Fc}$	Length of the fixed contact
$L_{Mc}$	Length of moving contact
$W_c$	Width of the contact
$t_c$	Thickness of the contact
$g_c$	Gap between the fixed contacts
$\rho_c$	Electrical resistivity of the contact material
$R_{cs}$	Contact resistance of the microelectrical contact
$a_c$	Radius of the contact spot
$Fc$	Force acting on the moving contact
$g_{cl}$	Gap between fixed and moving contacts
$R_{cr}$	Radius of the contact
$E_c$	Young's modulus
$p_c$	Poisson's ratio of the contact material
$J$	Source current density
$T$	Maximum anode temperature
$\dot{Q}_h$	Heat transfer rate
$P_c$	Contact power
$T_{am}$	Ambient temperature
$I_c$	Contact current
$w_m$	Width of moving electrode
$A$	Cross sectional area
$l$	Length
$h$	Height
$\sigma$	Electrical conductivity
$k$	Thermal conductivity of the material
$w_m$	Moving electrode width
$C_{OFF}$	OFF-state capacitance
$t_c$	Thickness of the contact

$W_c$	Width of the contact
$L_{Fc}$	Length of the fixed contacts
$L_{Mc}$	Length of the moving contact
$g_c$	Gap between fixed contacts
$d_c$	Gap between floating and fixed contact
$C_{F1}$	Fringing field due to the finite dimensions of the electrodes
$C_{F11}$	Fringing field associated with the height of the electrical contacts
$C_{F2}$	Fringing field due to the finite dimensions of the electrodes
$C_{F12}$	Fringing field associated with the height of the electrical contacts
$d_c$	OFF-state capacitance
$E_c$	Contact electric field
$Q$	Charge of the microelectrical contact
$V_c$	Contact voltage
$I_c$	Maximum is current flowing through the contact during ON-state
$P_c$	Maximum power appearing across the contact during switching state
$V_c$	Maximum voltage across the microelectrical contact
$g_c$	Gap between anode and cathode
$t_s$	Switching time
$L_b$	Length of the cantilever beam
$x_b$	Distance of the beam from anchor to end of the driving electrode
$t_b$	Thickness of the beam
$W_d$	Width of the driving electrode
$E_b$	Young's modulus of the beam
$V_{act}$	Actuation voltage
$g_d$	Gap across driving electrode
$L_d$	Length of the driving electrode
$A_d$	Area of the driving electrode
$T$	Temperature in Kelvin
$\rho_b$	Density of the beam

### **Materials**

Al	Aluminium
Cu	Copper
Au	Gold
Pt	Platinum

# CHAPTER 1

## INTRODUCTION

Switches are important components in electrical system, which are used to make and interrupt the electric current. The first manually operated mechanical switch was invented in 1884 by John Henry Holmes and was used for turning ON and OFF lights (Dummer et al., 1997). In 1889, mechanical switches were used to connect and disconnect telephone lines (Dryburgh et al., 2004). Manual operation became more complicated and impractical in applications such as electric power circuit protection and telecommunication systems. To overcome this challenge, automatically controllable mechanical switches were developed and operated magnetically. The magnetic field induced by current carrying coil was used for making mechanical contact which allows the electric current. These automatically controlled switches were also used as circuit breakers to protect the electrical circuits from short circuit and overcurrent fault. These switches can also be used as relays for isolating a particular region of the electrical circuit. These switches are used in vehicles, electric power distribution system, lighting systems and telecommunication systems. The low ON-state resistance and high isolation are the major advantages of these switches and have limitations with respect to size, speed, material usage, arc and scalability.

### 1.1 Miniaturization

Miniaturization is making of very small things with an excellent understanding of the deliberate application, scaling laws, material properties and diverse manufacturing options.

#### 1.1.1 The third industrial revolution

In 1765, invention of steam engine replaced human and animal power by machine power and led to the first industrial revolution. In 1850's, steam power was replaced by electric power and leads to second industrial revolution. In 1959, miniaturization concept was proposed by Feynman and the technological development was initiated with the invention of transistors by W. Shockley, J. Bardeen and W.H. Brattain in 1947. Microsystems technology was originated in 1982 that produces device components that range from one

micrometer to one millimeter. Microstructures have been manufactured using microfabrication techniques. This third industrial revolution led to a consecutive advancement of microelectronic devices, microsensors, microactuators, micromotors, micropumps and microswitches (Hsu, 2002). These microdevices have been successfully commercialized with the advantages of less material requirement, scalability, mass production, low production cost, easy transportation, less space requirements and packaging of more functional components in a single device.

### **1.1.2 Solid-state switches**

Microelectronic switches such as transistor, Metal Oxide Field Effect Transistor (MOSFET) are semiconductor based solid-state switches. These solid-state switches became more popular from 1960's. These switches have no moving mechanical parts and current flow is controlled by charge carrier movement. Compared to mechanical switches, solid-state switches have the advantages of longer life time, less noise, faster response, arcless and less weight. These switches hold huge market demand. The solid-state switches have the disadvantages of short channel effect, leakage current, voltage drop, sensitivity to ambient temperature and power loss (Song and Yoon, 2016; Steeneken et al., 2007). These are more suitable for frequent switching and very high speed applications.

### **1.1.3 Micromechanical switches**

Micromechanical switch uses mechanical moving structure to connect and disconnect the electrical circuit in order to control the current flow. These switches can be automatically controlled by electrostatic, thermal, magnetic and piezoelectric actuation techniques. These switches are faster than mechanical switches due to low mechanical inertia. Also these switches have less thermal distortion and less mechanical vibration due to low mass. The advantages of micromechanical switches are zero leakage current, freedom in selecting the substrate, insensitive to radiation, low ON-state resistance, fast switching, high isolation, low power loss, linearity and scalability. These switches have combined advantages of mechanical switches and solid-state switches (Song and Yoon, 2016). Micromechanical switches for Radio Frequency (RF) switching applications are well developed and commercialized. These switches have capacitive contact to achieve high isolation (Persano et al., 2016). For RF applications, these switches need to connect and

disconnect the signal with low power and high frequency in the range of 3kHz to 300GHz. These switches can also be used in logic circuits and memory devices.

## **1.2 Micromechanical Switches for Power Applications**

For power applications, the micromechanical switches should have metal to metal contact. The micromechanical switch has combined advantage of mechanical and solid-state switches in terms of fast switching, low ON-state resistance, high OFF-state isolation and smaller size. But, at the time of switching, power appears across the metal to metal contact and which leads to arc. This arc damages the metal contact and reduces the lifetime of the switch. Arc is an important factor which causes failure of the switch and reduces the life time. These switches can be commercialized for power applications, if the reliability and lifetime of the switch has been improved. Hence it is important to design an arcless micromechanical switch for power applications. These switches are more suitable for power applications in which non-frequent switching is required. They can be used as microcircuit breaker, microisolators, and microrelays. The most suitable application of these switches is battery life extension, overcurrent and short circuit protection. In addition, they can be also used for high power handling systems (General Electric, 2016).

General Electric lab has developed tiny micromechanical switches with unique material. These switches are thinner than a human hair and can control the flow of current. Keimel et al. (2012) reported that 200 micromechanical switches can able to withstand 350V and 10A. General Electric lab has designed 1kW rating relay using 400 micromechanical switches (General Electric, 2016). The micromechanical switch array handling 1kW power is shown in Figure 1.1. This research shows that the micromechanical switches can operate for billions of cycles under extreme operating conditions while maintaining low ON-state contact resistance.

Bachman et al. (2012) reported a magnetically actuated micromechanical switch, which is able to handle 0.97A, 10.2W at 10.6V DC and 15W at 110V AC. This micromechanical switch is capable of turning ON and OFF 15W incandescent lamp at 120V and is shown in Figure 1.2.

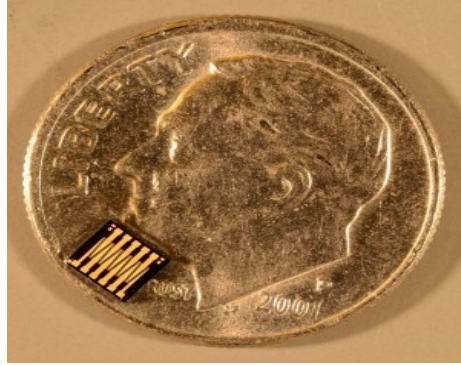


**Figure 1.1:** A die containing 400 micromechanical switches on the top of a US dime  
(General Electric, 2016)



**Figure 1.2:** Micromechanical switch turning ON incandescent light bulb  
(Bachman et al., 2012)

### **1.3 Arcless Switching**

Arcs in mechanical switches are well researched, but arc analysis in micromechanical switches attracts the attention of researchers (Slade, 2013). In micromechanical switches, the arcless switching is achieved by cold switching. Micromechanical switches connected in parallel with solid-state devices result an arcless switching and is called cold switching. In cold switching, the switch is actuated without applying DC or AC power across the contact during actuation. That is, power across the contact forcefully made to zero at the time of switching. Hence switch failures such as mechanical structural fatigue, contact stiction, thermomechanical damage etc., can be avoided (Yang et al., 2010). Although cold switching of micromechanical switch has enriched advantages in some aspect, they also have some concerns, such as increase in number of devices and device



size (Karady et al, 2006). Use of parallel connected solid-state devices, increases the resistance of the switching system and leads to increase in losses and heat. This may lead to additional requirement of heat sink units. Because of solid-state devices, the leakage current problem is still present. The leakage current leads to OFF-state power losses. In cold switching, arcless switching is achieved with compromising the ON-state resistance and isolation.

Hot switching is less researched for micromechanical switches. In this arcless switching can be achieved while maintaining low ON-state resistance and high OFF-state isolation. Arcless switching through hot switching in micromechanical switch is an interesting area which can improve the lifetime of the power switching system.

To design an arcless micromechanical switch, the various parts of the switch which produce arc and the parameters influence on the ignition of arc have to be analyzed for various states of the switch. Arc analysis for micromechanical switch during hot switching is challenging. Scalable micromechanical switch array needs to be designed to achieve the required rating for high power applications. The arcless scalable switching array can be achieved for higher rating with individual arcless micromechanical switches. The fundamental challenges of switch miniaturization and arcless switching will be solved by interdisciplinary research of device modeling, design, analysis and materials.

## **1.4 Scope for Applications**

One of the most important applications of micromechanical switches are replacement of automotive relays. A car uses approximately 15 relays for the basic operations like lighting headlamps, intermittent wipers, horn etc. The number of relays increase from 50 to 150 because of increased sophistication like car antennas, power windows, power seats, car stereos, door locks, defoggers, power sunroofs, interior lighting etc. Hence there is a huge market demand for micromechanical switches so that the weight of the car, power loss can be reduced thereby improving efficiency with improved automobile performance (Wood et al., 1998; Takahashi et al., 2004). The absence of leakage current increases the battery life and is the promising application in battery operated electric vehicles. Also, the automated micromechanical switches can be used in handheld electronic devices, industrial equipments, protection devices, battery life extension

systems, industrial power control, satellite, aircrafts, space power system, shipboards, energy scavenging system, residential and commercial applications, high power distribution system and lighting systems etc., (Song and Yoon, 2016; General Electric, 2016). Such switches can be used in System on Chip (SoC) for power drain circuits, power quality and clock gating applications (Mathúna et al., 2012).

## **1.5 Research objectives and Scope**

This thesis presents the modeling and analysis of scalable arcless micromechanical switches for power application. The objectives of the thesis are as follows:

**Objective 1:** *To develop and analyze conceptual model of scalable Total Cross Tied (TCT) array of micromechanical switches for electric power applications and compare it's performance with the conventional mechanical switches and solid-state switches. To study various types of micromechanical switches and to identify the suitable micromechanical switch for power switching applications.*

The micromechanical switches suitable for power applications with required actuation principle has been identified. Using different device parameters, comparative study of mechanical, solid-state and TCT array of micromechanical switches has been carried out using MATLAB Simulink to understand the performance of micromechanical switches.

**Objective 2:** *To design an arcless driving electrode and to analyze its breakdown arc occurrence using mathematical modeling and FEM simulation.*

The driving electrode is the actuation electrode. The voltage across this electrode drives the micromechanical switch. This electrode is a non-touching electrode. The type of arc which occurs in these electrodes has been identified as breakdown arc and its characteristics have been presented. The critical parameters which induce the arc have been identified and the electric field is captured for various materials to design arcless driving electrodes.

**Objective 3:** *To design arcless microelectrical contact with floating electrode configuration and to analyze the pre-breakdown and breakdown arc occurrence using mathematical modeling and FEM simulation.*

The microelectrical contact with floating electrode is responsible for the current flow. The pre-breakdown arc and breakdown arc characteristics have been discussed. The parameters inducing these two types of arc have been identified. Extensive FEM based electrothermal analysis using COMSOL multiphysics simulation has been carried out for various materials to design arcless microelectrical contact. Along with this the ON-state resistance and current carrying capability have been predicted.

**Objective 4:** *To design an electrostatically actuated arcless micromechanical switch for power application and to analyze the electromechanical characteristic during hot switching. Also to develop scalable TCT micromechanical switch array configuration for achieving a high power rating.*

A complete electrostatically actuated micromechanical switch of rating 12V, 0.2A has been designed. The electromechanical characteristics such as actuation voltage, force, switching speed and quality (Q) factor has been obtained using mathematical modeling and Coventor MEMS+ FEM simulation. The system level simulation has been carried out to analyze the switching characteristics using Coventor MEMS+, Cadence virtuoso and MATLAB Simulink. Scalable TCT micromechanical switch array has been designed for the rating of 140V, 3A.

## **1.6 Organization of Thesis**

This research work is presented in seven chapters. The brief description is as follows:

Chapter 1 is an introduction to switch, miniaturization, solid-state and micromechanical switches. It discusses the motivation and scope for applications. An overview of micromechanical switches for power switching applications, challenges, microelectrical

contact, arcless switching through hot switching and scalability are discussed. Also, the objectives and scope of the thesis are presented.

Chapter 2 consists of a comprehensive literature review that further justifies the significance of the proposed work, particularly with respect to the research objectives presented in Chapter 1. Literature on related fields like mechanical switches, solid-state switches, types of micromechanical switches, actuation techniques, electrostatically actuated switch, breakdown arc, pre-breakdown arc (metal arc), contact physics, materials, scalability, resistance, isolation, switching speed, current carrying capability, cold & hot switching, electrothermal and electromechanical behaviors are presented. Discussion about the simulation tools such as MATLAB Simulink, COMSOL multiphysics, Coventor MEMS+, and Cadence virtuoso which have been used to achieve the objectives are also presented. Based on the literature review, the gaps are identified.

Chapter 3 proposes scalable TCT array configuration of micromechanical switches for power applications. The device parameters of mechanical switches, solid-state switches, and micromechanical switches are identified, and their performance characteristics are obtained for load conditions, and the results are compared. It gives an idea about the leakage current and power loss. In depth study of various micromechanical switches actuation techniques discusses the suitability of electrostatically actuated switches for power applications.

Chapter 4 describes a non-touching electrode which is used as driving electrode. The breakdown arc in microgap is discussed with respect to modified Paschen curve. The applicability of this concept in the design of arcless micromechanical switch has been discussed. The boundary to be maintained to achieve arcless driving electrode is identified. The importance of capacitance and electric field in achieving arcless driving electrode is also discussed.

Chapter 5 An FEM based electrothermal analysis has been carried out to predict the current carrying capability and power withstanding capability of the microelectrical contact. The FEM analysis results are validated using mathematical model. The possibility of occurrence of pre-breakdown arc and breakdown arc are also discussed.

The voltage, current, and power limit to achieve arcless switch through hot switching are extensively presented.

Chapter 6 presents the modeling and analysis of electrostatically actuated arcless micromechanical switch and analyze its electromechanical characteristics for power switching applications. The micromechanical switch uses the arcless driving electrode designed in chapter 4 and the arcless microelectrical contact designed in chapter 5. The influences of switching speed, Q factor on the design of arcless micromechanical switches are discussed. Scalability of microelectrical switches for various rating and the application areas are discussed in detail.

Conclusion and future work are presented in chapter 7.

## **CHAPTER 2**

### **LITERATURE SURVEY**

This chapter provides further justification to the significance of the research objectives presented in Chapter 1 for the modeling and analysis of scalable, arcless, electrostatically actuated micromechanical switches for power applications. On view of this, the literature survey is classified into following categories: classification of switches, micromechanical switches for power applications, challenges, switching modes of the micromechanical switches, methodology and simulation tools. Also the research gaps have been identified.

#### **2.1 Classification of Switches**

Switches are devices, which are capable of making, carrying and interrupting the electric current flow in an electrical system. These switches can be used to interrupt both AC and DC electrical signals. Since the invention of electricity, switches have been studied extensively. These switches are broadly classified into four categories: 1. mechanical switches (Burkes et al., 1978), 2. solid-state switches (Etal, 1967), 3. hybrid switches (Paice et al., 1984), and 4. micromechanical switches (Keimel et al., 2012). These switches also can be used as relays, circuit breakers, connectors and isolators. Switches were used in many applications such as industrial, commercial, residential and vehicles etc., (Leviton, 2016).

##### **2.1.1 Mechanical switches**

In early 19<sup>th</sup> century, mechanical switches are operated manually and are used for turn-ON and turn-OFF electrical lamps (Dummer et al., 1997). Mechanical switches use moving metal contact structures to make and interrupt current flow in the electrical circuit. The metal contact structure is called as electrical contact (Holm, 2000). During ON-state of the switch, these electrical contacts touch each other and allow the electric current. The current flow depends on the ON-state resistance of the electrical contact. The ON-state resistance is very low of the order of few milli ohms (Slade, 2013). During OFF-state of the switch, the contacts won't touch each other. This physical separation leads to infinite resistance and high isolation. These switches can be operated manually or automatically. Automatically controlled switches are mainly operated magnetically (Advameg, 2016).

During the switching period, arc occurs across the electrical contact and leads to contact erosion (Slade, 2013). Arc can be controlled by switching at the natural zero crossing point for AC current. Arc is a serious issue in DC switching.

### ***Arc in mechanical switches***

During opening of current carrying switch, the medium in between the electrical contacts become highly ionized. The interrupting current gets low resistive path through the medium. Hence, current continues to flow even when the contacts are physically separated. The path between contacts becomes heated and it glows due to current flow, this phenomenon is called arc (Slade, 2013). An arc is an electrical breakdown of medium between the contacts, which produces an electrical discharge. The current through a normally non-conductive media such as air produces plasma and the plasma may produce visible light. If the circuit carrying current is interrupted by a switch an arc occurs for the duration ranging from 10 to 100 milliseconds (Holm, 2000). The study on arc has been carried out extensively by the researchers for mechanical switches. Atalla (1958) presented the theory behind arc formation during opening and closing of the electrical contact of the mechanical switch. It is reported that for arc occurrence the temperature should rise to the boiling temperature of the metal contact. Atalla (1953) reported that for centimeter gaps, the breakdown arc is initiated when the electric field ranges between  $0.6 \times 10^6$  V/cm and  $30 \times 10^6$  V/cm. The electric field required to initiate breakdown arc are identified as  $2.4 \times 10^6$  V/cm,  $4.2 \times 10^6$  V/cm,  $3 \times 10^6$  V/cm,  $2 \times 10^6$  V/cm and  $4.9 \times 10^6$  V/cm for carbon, Nickel, Palladium, Silver and Tungsten metals. Boyle and Kisliuk (1955) presented the breakdown electric field of contacts separated by centimeter gap at high pressure. At high pressure the breakdown electric field of steel and Aluminium are  $1.1 \times 10^7$  V/cm and  $9.3 \times 10^6$  V/cm respectively. Abou-Seada (1984) reported that the breakdown voltage is 30kV for point to plane air gap of 6cm at 200kHz frequency. Sekikawa and Kubono (2004) investigated the voltage and current characteristics of breaking arc generated between opening contacts at constant velocity of 1 cm/s in air medium. The destructive effects of the arc are minimized by using multiple break contacts (Morel et al., 1991), contacts immersed in oil or gas (Czarnecki and Corporation, 2013), arc path deionization (Andronachi and Istrate, 2015), and magnetic blow out of arc (Sawa et al., 2015).

Wear occurs at the time of opening and closing of electrical contact. Due to the roughness of the surface, only a small portion of the contacts touches and entire current flows through this part of the contact. Switching high current leads to degradation or damage of electrical contact (Slade, 2013). Enough high voltage across the contact generate arc and destroy the electrical contact. Aluminium and copper are commonly used contact materials in mechanical switches (Holm, 2000). Li et al., (2015) presented non-contact arc study for DC electrical systems (Li et al., 2015). Arc model has been extensively studied for mechanical switches. Mayr arc model and casie arc model has been developed for AC switches (Tseng et al., 1997). Ammerman et al., (2010) developed arc models for DC switches with the gap of 1mm to 10mm.

### **2.1.2 Solid-state switches**

Solid-state switches are semiconductor based electronic devices, in which switching action has been carried out without the movement of electrical contact. Electric current flow is due to electron movement under certain operating conditions. Since it does not have any moving parts, there is no arc. These solid-state switches are called as static switches (Van, 1978; Etal, 1967)). Advanced power semiconductor based solid-state devices such as thyristors, Bipolar Junction Transistor (BJT), Gate Turn OFF thyristor (GTO) etc., have replaced the mechanical switches in the applications which were needed frequent switching. Boudreaux and Nelms (1996) examined MOSFET, Insulated Gate Bipolar Transistor (IGBT), and MOS-Controlled Thyristor (MCT) device for operation in the range of 200V to 400V and 1A to 50A. These solid-state switches are commonly used in power converters and power conditioning circuits (Rashid, 1993; Mohan et al., 2003). These solid-state switches are also used for relay and circuit breaking applications. Also these devices have been used from low voltage system of 12V to High Voltage Direct Current (HVDC) and High Voltage Alternating Current (HVAC) systems (Meyer et al., 2006). These switches provide more efficiency, easier control and faster switching. Kapoor et al., (2012) reported that solid-state switches have low power rating, high leakage current, high ON-state resistance and high power losses when compared to the mechanical switches. Since the ON-state conduction loss is more, heat sink is also needed (Mu et al., 2009). This increases the cost of the overall switching system. Arcless switching using power semiconductor switching devices increases the feasibility for



aircraft applications. But the power losses cause severe thermal problems for high current applications (Atmadji and Slood, 2005). The current and voltage rating, power losses, blocking voltage, turn-ON time, turn-OFF time, trigger mechanism, allowable transient overvoltage, maximum  $dV/dt$  and  $dI/dt$ , etc., has to be taken in to consideration while selecting solid-state switches for power applications (Rashid, 1993). These switches used for battery operated system, reduces the battery lifetime because of the leakage current and high ON-state resistance.

### **2.1.3 Hybrid switches**

Paice et al., (1984) presented the hybrid switch in which both mechanical and solid-state switches are connected in parallel. The mechanical switch provides a path for the continuous current. The solid-state switch operates to bypass the current only at the turn-ON and turn-OFF time of the main switch. This provides zero current or voltage across the mechanical switch during switching period and leads to arcless switching. This switch motivated technically by having the advantages of both mechanical and solid-state switches by eliminating the disadvantages. Hybrid switch uses mechanical switch and Integrated Gate-Commutated Thyristors (IGCTs) has been reported (Meyer and Rufer, 2006). Theisen et al., (1986) presented a 270V DC hybrid switch. A single phase AC hybrid switch has been successfully designed and tested with a rating of 240V/16A (Shammas, 1994). Atmadji and Slood (2005) discussed a hybrid switch that is capable of interrupting 20V/4A and 270 V/1500A. They have discussed the suitability of hybrid switches for aerospace applications. Also reported that, an arc appeared on the contacts for microseconds time and the contact erosion reported is very less when compared with mechanical switches. The hybrid switch cannot eliminate arcing completely due to the inductive nature of the circuits and contact bounce. Swingler and McBride (2008) reported the arcing and arc erosion reduction using hybrid switching. Bielinski et al., (1985) reported that these switches have the disadvantages such as large number of components, complex structure, leakage current in the OFF-state, power losses in the ON-state and inadequate switching performance. Shukla and Demetriades (2015) suggested that mechanical switches are more suitable than solid-state and hybrid switches for high power application.

#### **2.1.4 Micromechanical switches**

Recent technological developments have increased research opportunities in the field of micromechanics. Microfabrication technology allows batch manufacturing of microdevices, which reduces the production cost (Xia et al., 2014). Khoshnoud and de Silva (2012) reported the use of microdevices as sensors and actuators. Different actuation and sensing properties such as piezoelectric, electrostatic, thermal, electromagnetic and optical have been discussed by researchers for last 20 years. The choice of microdevices and actuation scheme depends on the requirement of the particular application (Baglio et al., 2008). More reported microdevices are microswitches, micromirrors, microsensors, micropumps, microvalves and microgrippers (Zhou, 2008). The microscale structures obey the physical phenomena of macroscale, but the influence changes relatively because of the variation in the weight (Baglio et al., 2008).

A micromechanical switch uses micromechanical movement to connect and disconnect the signals. These micromechanical switches are classified into series and shunt switches. The series configuration is commonly used to pass signals along the signal path when the micromechanical switch is actuated. But the shunt configuration is commonly used to connect the signal to the circuit ground (Rebeiz, 2003). Zavracky et al., (1999) discussed the use of micromechanical switches for microwave applications. The micromechanical switches have wide applications in the aerospace, military and commercial sectors and also have large potential market (Rebeiz et al., 2013). Capacitive and ohmic contacts are commonly used in micromechanical switches. In a capacitive contact, the signals are separated by a dielectric material and form a capacitor. These contacts allow only high frequency signals. Hence it is more suitable for RF applications such as mobile phone antennas, telecommunication systems, satellite communication and wireless ports (Rebeiz, 2003). Micromechanical switches for high frequency application are well explored. Dielectric charging and contact degradation are the challenges in capacitive contact switches (Souchon et al., 2013). Radant (2003) have developed and commercialized micromechanical switches for RF applications. This device is ideally suited for many applications, such as RF and microwave multi-throw switching, radar beam steering antennas, phase shifters, RF test instrumentation, telecommunications and

broadband wireless access. Arc problem is also present in RF microswitches and researchers working on arcless switching in RF applications (Ruan et al., 2016). Capacitive contacts cannot be used for DC and AC switching applications. Goggin et al., (2015) discussed about commercialization of micromechanical switch for power applications.

## **2.2 Micromechanical Switches for Power Applications**

Micromechanical switches can be used for AC and DC power switching applications. Ma et al. (2016) designed a microrelay with the switching time of  $180\mu\text{s}$  and contact resistance of  $1\Omega$ . This switch uses Au contact of thickness  $0.3\mu\text{m}$  and capable of carrying  $0.02\text{A}$  current. These switches have wide applications in aerospace, military, commercial sectors and lighting applications. Zavracky et al., (1997) presented the micromechanical switch with the size of  $30\mu\text{m}$  wide and  $65\mu\text{m}$  long, handling  $5\text{ nA}$  at  $200\text{V}$ . The OFF-state voltage withstanding capability of this switch is  $100\text{V}$  with the leakage current of  $20\text{fA}$ . Khushalani et al., (2016) presented  $20\text{mA}$ ,  $10\text{mW}$ ,  $170\text{m}\Omega$  micromechanical switch for power switching applications. Ma et al., (2015) presented  $50\text{mA}$ ,  $2\text{V}$  microrelay for space power system. Lewis et al., (2015) presented  $50\text{mA}$ ,  $4\text{V}$ ,  $5\Omega$ , switch for DC power switching. Keimel et al., (2012) designed  $1\Omega$ ,  $3\mu\text{s}$  switch for DC power switching applications. Beckman et al., (2012) presented  $0.97\text{A}$ ,  $10.6\text{V}$ ,  $15\text{W}$  and  $3\text{ms}$  micromechanical switch for lighting applications. Park et al., (2012) investigated the use of micromechanical switches for energy scavenging applications. Yeatman (2007) discussed about thermally actuated switch for circuit applications. Micromechanical switches can be used for battery life extension, power gating and clock gating in Very Large Scale Integrated (VLSI) circuits (Raychowdhury et al., 2013; Shobak et al., 2011; Kam et al., 2013). These switches can be used in Field Programmable Gate Array (FPGA) routing switches for leakage power reduction (Satish, 2012). In these switches microelectrical contact allows and interrupts DC and AC electrical signals. Song and Yoon (2016) reported that microswitches can also be used for logic and memory applications. Lifetime of these switches depends upon the lifetime of their electrical contacts (Basu et al., 2013a). But these switches are not commercialized because of reliability and lifetime.

### **2.2.1 Challenges**

There are many factors which can cause failure in micromechanical switches. The reliability and lifetime of the micromechanical switches has been mainly affected by both electrical and mechanical stress. The electrical stress causes welding, melting, arcing and degradation of the microelectrical contact which leads to failure of micromechanical switches. Mechanical stress causes deformation and wear of micromechanical switches (Song and Yoon, 2016). One or both mechanisms combined together may also lead to failure of the switch. The contact material, surrounding temperature and pressure also plays an important role in the reliability (Toler et al., 2013). One of the important parameter which lead to failure is arc in micromechanical switch. To commercialize the micromechanical switch it is required to design reliable and low loss switches with high contact force (Mckillop et al., 2007). Also the reliability mainly depends on the switching mode of operation. Designing an arcless switch for high power rating is not feasible. But we can design arcless low power switches and connect them in array to increase the power handling capability.

### **2.3 Switching Modes**

Irrespective of the actuation technique, microelectrical contact may undergo two switching modes. They are called cold switching and hot switching. These switching modes are applicable for DC, low frequency AC and RF switching applications (Kim et al., 2008). Both switching modes cause damage to the microelectrical contact. The reliability of the microelectrical contact is more in cold switching than hot switching (Basu et al., 2014).

#### ***2.3.1 Cold switching***

In cold switching, the switching action has been carried out with the absence of electrical signal across microelectrical contact. Electronic devices are used to bypass the electrical signal. At the time of switching these devices force zero power across the microelectrical contact (Hennessy et al., 2013). This is very much similar to hybrid switching. Cold switching leads to struck open failure and wear on the microelectrical contact (Basu et al., 2014). The reliability and lifetime of the micromechanical switches are discussed under

cold switching condition (Newman et al., 2008). Radant (2003) has commercialized cold switching micromechanical switches for DC applications.

### **2.3.2 Hot switching**

In hot switching, switching action has been carried out with the presence of electrical signal across the microelectrical contact (Hennessy et al., 2013). During hot switching, welding and material transfer of microelectrical contact leads to struck-close failure. Field evaporation, field emission, arc and metal bridge are responsible for material transfer (Basu et al., 2014). Lee et al., (2001) presented the arc discharge and erosion behavior of silver electric contacts between static microgap. Song et al., (2013) discussed the improvement of hot switching lifetime of DC micromechanical switches using a drain voltage sustaining capacitor. Reliability in hot switching ruthenium microcontacts has been discussed (Basu et al., 2013b). Lewis et al., (2015) evaluated the voltage transients during the switching of microrelay contacts. Rumbach and Go, (2012) discussed about breakdown of microgaps, field emission and microdischarges. Basu et al., (2014) presented hot switching damage mechanism of microswitches. The contact material plays a major role in hot switching. Microelectrical contact material should have good conductivity, low sensitivity to oxidation and chemical inertness (Mulloni et al., 2011). Coutu et al., (2004) discussed various possible contact materials for microelectrical contact. The force applied on the contact, gap and Q factor are some of the important parameters to be taken in to account while designing arcless micromechanical switches (Song and Yoon, 2016). Therefore, microwelding and arc would be eliminated, if the voltages, current and power are limited within the boundary (Jau, 2013).

## **2.4 Modeling and Design Challenges**

The view, understanding, prediction, visualization, control and behavior of microdevices in the microdimensions are challenging. Multiphysics modeling is required, because coupling among different domains such as solid mechanics, heat transfer, structural mechanics, electrothermal and electromechanical are involved (Batra et al., 2007). To realize the potential and growth of micromechanical switches, modeling, analysis, and design techniques are required to address electrical, mechanical and thermal behaviors.

The behavior of the overall switch is not limited to the analysis of separate mechanical and electrical behavior, but the simultaneous combination of mechanical, electrical and thermal behaviors (Dewey et al., 2001).

## **2.5 Methodology**

Microsystems fabrication technology has developed significantly in past ten years. But even now microsystem design is a challenging task. Micromechanical system design generally involves highly customized analyses, which are very complicated and often non-repeatable (Schwarz, 1998). Microsystem design and fabrication processes require experts from interdisciplinary research areas. Hence, there is a need for more structured design methodology and supporting tool set for micromechanical systems that promotes higher levels of abstraction and behavioral design (Dewey et al., 2001). In order to accurately describe the switch behavior, performance modeling has to be carried out (Zhu and Espinosa, 2004). In order to increase efficiency and effectiveness of the design process, appropriate models are needed. To generate new design solutions, models of certain level of abstraction are required. In addition to this, computer-aided models enable the prediction of electrical, thermal and mechanical performance of the micromechanical switches. At the same time, a Finite Element Model (FEM) is built in order to investigate the behavior of designed micromechanical switch.

Conceptual model is a model made of the composition of concepts and literature data, which are used to know and understand the physical structure and performance of the system. The conceptual model plays an important role in the overall system development. The conceptual model is not fully developed model. But if the conceptual model is implemented properly, it should satisfy the fundamental objectives (Sokolowski and Banks, 2010).

Modeling and simulation facilitate the designers to test whether the design specifications are met by using virtual rather than physical experiments. The designers can be able to predict the performance of particular system using modeling. This significantly reduces the design cycle and reduces the cost of design. It also provides the immediate feedback on design decisions which, in turn, promises more comprehensive exploration of design alternatives and a better performing final design. Simulation is particularly important for

the design of multidisciplinary, multiphysics systems in which components from different disciplines such as mechanical, electrical, thermal, plasma and material are tightly coupled to achieve required system performance (Sinha et al., 2001).

The field distribution can be evaluated using numerical techniques, such as Boundary Element Method, Charge Simulation Method, Finite Difference Method and FEM. FEM modeling is more suitable for electrostatic field, electrothermal and electromechanical problems because it involves accurate discretization of the domain. The FEM modeling is comparatively simple technique for predicting the field and temperature of the highly curved and thin contact surfaces with different materials (Shi et al., 2009). It is also a flexible method that is well suited to problems with complicated geometry (Eiser et al., 2016). The FEM analysis is a numerical technique used for finding approximate solutions to boundary value problems and has been widely used in magnetic and electric field analyses. It is a technique to solve partial differential equations. In this large problem is subdivided in to smaller parts called finite element. Simple equations are used to model the smaller parts. The simple equations that model these smaller parts are then assembled into a larger system of equations that models the entire problem. This method has the advantages of accurate representation of complex geometry, inclusion of material properties, easy representation of the total solution and captures the local effects (Johnson, 2009). FEM modeling can be used to predict the resistance for complex geometry (Toler et al., 2013). COMSOL multiphysics (COMSOL Inc, 2014), ANSYS (ANSYS, 2016), Coventor (Coventor Inc, 2016) are commonly used FEM tools. The system level simulation is required to validate the functional behaviors of micromechanical switches (Soul and Dey, 2013).

## **2.6 Simulation Tools**

The research objectives stated in chapter 1 are achieved using the following software simulation tools.

### **2.6.1 MATLAB Simulink**

MATLAB Simulink was developed by MathWorks, which block diagram environment is used to model, simulate and analyze multi-domain systems. It is customized with set of block libraries. To develop electrical system, Simscape Power Systems module of

Simulink can be used (MathWorks, 1994). Lee et al. (2016) has obtained the transient current interruption characteristics of circuit breaker using Simulink. Khan et al. (2015) investigated transient impedance and current interruption characteristics of hybrid circuit breaker for DC applications using MATLAB Simulink.

### **2.6.2 COMSOL Multiphysics**

COMSOL Multiphysics is a FEM based simulation tool used to model and simulate multiphysics based problems (COMSOL Inc, 2014). It is based on advanced numerical method and has more than 30 add-on products. This tool has modules and physical interfaces for mechanical, fluid, plasma, chemical and electrical applications. Geometry selection, assigning material, meshing, setting physics and boundary conditions, studies, solvers, post processing, and visualizations are the various steps involved in the modeling and simulation (COMSOL Inc, 2014). 2D and 3D analysis can be carried out for wide ranges from micrometer to meter scale. Batunlu and Albarbar (2016) carried out electrothermal analysis for IGBT using COMSOL to predict the heat distribution. Lu et al. (2016) computed the temperature profile and voltage dependence of temperature rise of the microchannel. Arnaud and Branco (2016) evaluated transient temperature characteristics and distribution subjected to sinusoidal field for Yttrium Barium Copper Oxide (YBCO) bulk magnet. Hajjaj et al. (2016) designed electrostatically actuated resonators using COMSOL multiphysics and simulated beam displacement and temperature corresponding to applied voltage. Li et al. (2016) carried out electrothermal co-simulation of 3D carbon based heterogeneous using COMSOL multiphysics FEM tool to obtain static and transient temperature profile. In this research work, COMSOL multiphysics are used for FEM modeling of driving electrode and microelectrical contact. This tool uses following work flow for the FEM modeling using multiphysics simulation.

1. Set up the model environment
2. Create geometrical object
3. Specify material properties
4. Define physics boundary conditions
5. Create the mesh
6. Run the Simulation and process results



To ensure the grid independence of the predicted values, the mesh has to be generated and the number of mesh elements needs to be increased (extremely course, extra course, courser, course, normal, fine, finer, extra fine and extremely fine in COMSOL) until no further noticeable change in the model prediction has been observed. At this point adding mesh is no longer beneficial and hence the result is grid (mesh) independent.

### **2.6.3 Coventor MEMS+**

Coventor MEMS+ is a higher order finite element software tool. This can be used to test and validate microphysics such as mechanics, eletrostatic, contact and piezoelectric models. It can be used for designing microsystem based devices such as microsensors, microphones, micromirrors, microswitches and energy harvesters etc. Fast microsystem simulation at system and device level can be carried out by MEMS+ (Coventor Inc, 2016). Model order reduction techniques are employed to reduce the complexity of the multi degree-of-freedom models, to speed up simulation time and to provide a path for designing microstructures together with electronic hardware (Schröpfer et al., 2016). MEMS+ designs can be directly imported in to MATLAB Simulink and Cadence Virtuoso. Muley, Naveed, and Shingare (2013) designed RF switch using Coventor MEMS+ tool. The static and transient characteristics of the RF switch such as actuation voltage, quality factor and switching time are also obtained using this tool.

#### ***MEMS+ for MATLAB Simulink***

Using MEMS+ for MATLAB and Simulink, the microstructure designed in MEMS+ can be interfaced with Simulink and MATLAB script. Hence external control and signal processing circuit can be connected and steady-state and transient analysis can be carried out. MATLAB Simulink results can be loaded back in to the MEMS+ Scene3D module for 3D viewing (Coventor Inc, 2016).

#### ***MEMS+ for Cadence***

Solution for coupled MEMS+IC design can be obtained using MEMS+ for Cadence Virtuoso. The microstructures designed in MEMS+ can be automatically converted in to Integrated Circuits (IC) compatible models and parametric layout (Pcells) for the Cadence Virtuoso design environment. The system level simulations can be carried out by this tool (Coventor Inc, 2016).

Ekwińska et al., (2015) presented the design of micromechanical system integrated with circuit components. Torri et al., (2015) carried out the design of a micromechanical switch based Complementary Metal Oxide Semiconductor (CMOS) autonomous switched oscillator and obtained transient response characteristics using MEMS+ and Cadence. Parent et al., (2015) designed a gyroscope using MEMS+ and Simulink. In this work this tool is used to design and analyze the micromechanical switch and to obtain its electromechanical characteristics.

## **2.7 Research Gaps in the Literature**

Micromechanical switches offer various advantages over mechanical, solid-state and hybrid switches. These switches can be integrated on chip with electrical and electronic devices. These switches can offer better battery life extension because of low resistance and high isolation. Commercializing such switches will be beneficial for less frequent AC and DC switching applications. These switches will find wide range of applications in satellites, aircraft, automobiles, handheld electronic devices, battery operated systems, electric vehicles and power distribution system. Arcless design of micromechanical switches place an important role in commercialization. In general the area of arcless micromechanical switches has been subject of intense research and novel application in recent years. Following are the research gaps identified through critical literature review.

1. Performance parameters of scalable array configuration of micromechanical switch needs to be compared with the mechanical, solid-state and solid-state switch array. The structure and actuation mechanism of the micromechanical switch more suitable for power switching applications needs to be presented through conceptual modeling and analysis. All the possible arc occurrence parts of the micromechanical switches have to be identified.
2. Occurrence of breakdown arc for microgap at the driving electrode of the micromechanical switch needs to be examined and analyzed.
3. Electrothermal analysis of microelectrical contact formed by the fixed and floating electrodes needs to be investigated to achieve arcless switching. The current carrying capability and voltage withstanding capability also needs to be investigated.

4. Electromechanical properties and arcless nature of micromechanical switches during hot switching needs to be investigated. Also the behavior of the micromechanical switch in TCT, scalable array configuration needs to be analyzed under load condition.

Research towards these gaps would help to identify the micromechanical switch suitable for power applications. And also would help to identify the arc ignition parts of the micromechanical switch. This would also help to design arcless micromechanical switch which can be further used in scalable array configuration to get the required power rating.

# CHAPTER 3

## CONCEPT OF SCALABLE TOTAL CROSS TIED MICROMECHANICAL SWITCH ARRAY

### 3.1 Introduction

Switches are important component in electrical system. Various types of switches such as mechanical, solid-state, hybrid and micromechanical switches have been used for power applications. In chapter 2, the types of switches, their performance characteristics and application areas are discussed in detail. The micromechanical switches can be commercialized, if their failure mechanisms are addressed (Spengen et al., 2010).

It is known that that micromechanical switches have the advantages of low ON-state resistance, very high OFF-state resistance, high isolation, no leakage current, less power loss, fast switching, high linearity, small size and low cost in bulk production (Park et al., 2012; Yeatman, 2007). They are capable of handling low power. The micromechanical switch can be designed for 150V, 100mA (Karady et al., 2005). We propose Total Cross Tied (TCT) array configuration of micromechanical switches to achieve higher power rating. The proposed array is a reliable structure which uses low rating switches to enhance the power rating.

The TCT array configuration has been explored for photovoltaic applications (Bastidas et al., 2013). Chakraborty et al., (2013) discusses the TCT array for solid-state electronic switches for renewable energy and distribution systems.

In order to investigate the behavior of the proposed TCT array configuration of micromechanical switches, the conceptual model has been developed. The performance of these switches needs to be compared with mechanical and solid-state switches. To compare the behavior of these switches, an equivalent DC power circuit is considered and results are obtained using MATLAB Simulink for the rating 400V/ 6A. Similarly, the performance characteristics are obtained for AC equivalent electrical system for 230V/6A rating. This analysis is required to know the behavior of the TCT array with DC and AC load conditions. This analysis would give more confident to proceed with the design of

arcless micromechanical switch for power applications, if the results are in agreement with the reported results.

Micromechanical switches are widely used for RF, low frequency, sensing and actuation applications. Micromechanical switches for power applications are reported for various ratings of 50mA, 2V (Ma et al., (2015), 50mA, 4V (Lewis et al., 2015) and 0.97A, 10.6V (Beckman et al., 2012). There are many actuation mechanisms used for the micromechanical switches. It is essential to carryout extensive analysis for selecting suitable actuation (driving) technique for power applications. Various parameters need to be considered while selecting the actuation technique. This chapter also discusses the micromechanical switch actuation technique suitable for power applications.

The structure of the micromechanical switches and the parts which are responsible for producing arc also needs to be analyzed. The structure of the switch suitable for power applications and the parts at which arc may occur is also presented in this chapter.

### 3.2 Characteristic of DC Electrical System

A DC electrical circuit considered to evaluate the characteristics of various switches is shown in Figure 3.1. The DC system contains a voltage source  $E_s$ , resistance  $R$  and inductance  $L$  are connected in series with a resistive load  $R_L$  through a switch.

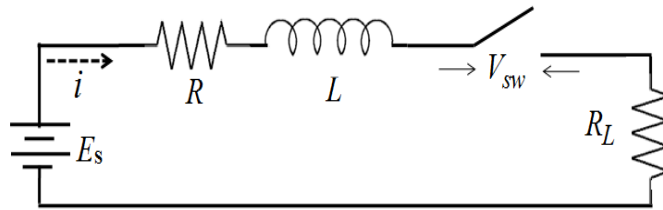


**Figure 3.1:** Equivalent DC electrical system

The circuit is described by the equation

$$E_s = Ri + L(di/dt) + V_{sw} + R_L i \quad (3.1)$$

Where  $i$  is the current flows through the circuit,  $t$  is the time and  $V_{sw}$  is the switch voltage

Before current interruption, the switch is in ON-state, hence  $V_{sw} = 0$  and  $i_{sw} = i$ . Since the switch is in series,  $i = i_{sw} = i_L$ . Where  $i_{sw}$  and  $i_L$  are the current flows through the switch

and load respectively. During switching period, the current is interrupted, thus the switch voltage  $V_{sw}$  increases from zero to maximum and switch current  $i_{sw}$  falls from  $i$  to zero. At the same time, the load voltage  $V_L$  and load current  $i_L$  become zero and the load is completely isolated from the supply. After current interruption, the switch is in OFF-state, hence  $V_{sw}$  is maximum and  $i_{sw} = 0$ . The power loss  $P_{sw}$  across the switch is given by  $P_{sw} = V_{sw} \times i_{sw}$ . The parameter values considered for the DC equivalent system is given in Table 3.1.

**Table 3.1:** Parameters of DC equivalent system

Parameter	Symbol	Value	Unit
Source Voltage	$E_s$	400	V
Load Resistance	$R_L$	67	$\Omega$
Resistance	$R$	1	$\Omega$
Inductance	$L$	0.01	H

The performance of the equivalent DC system is analyzed with mechanical, solid-state, solid-state array and proposed TCT array of micromechanical switches for the rating of 400V/6A. For this analysis the corresponding switch parameters are taken from the reported literatures as sample. The performance parameters are obtained through simulation using MATLAB Simulink. Simulation has been carried out for the time period of 0 to 0.01s. The switch is kept in ON-state for the time less than 0.005s. At 0.005s, control signal is given to the switch to make it OFF.

### 3.2.1 Mechanical switches

The DC equivalent circuit with mechanical switch is shown in Figure 3.2. The mechanical switches have fixed and moving contacts called anode and cathode. The gap forms between fixed and moving contact during OFF-state. The heavy mechanical structure reduces the controllability. Placing switches in parallel to increase the current rating is not efficient due to slow switching speed. The slow switching speed of these switches causes asynchronous switching problem and thus one switch may carry the entire current at the beginning of turn-ON state.

But it can be connected in series, in order to increase the voltage rating. The sample parameter of the mechanical switch is identified from the literature as 400V, 6A and ON-

state resistance  $0.03\Omega$  (MINIATURE, 2006). The simulations are carried out and the results are presented in Figure 3.3.

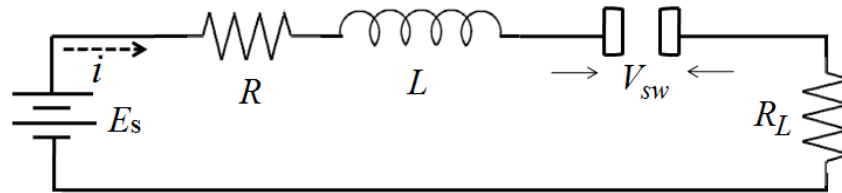


**Figure 3.2:** DC system with mechanical switch

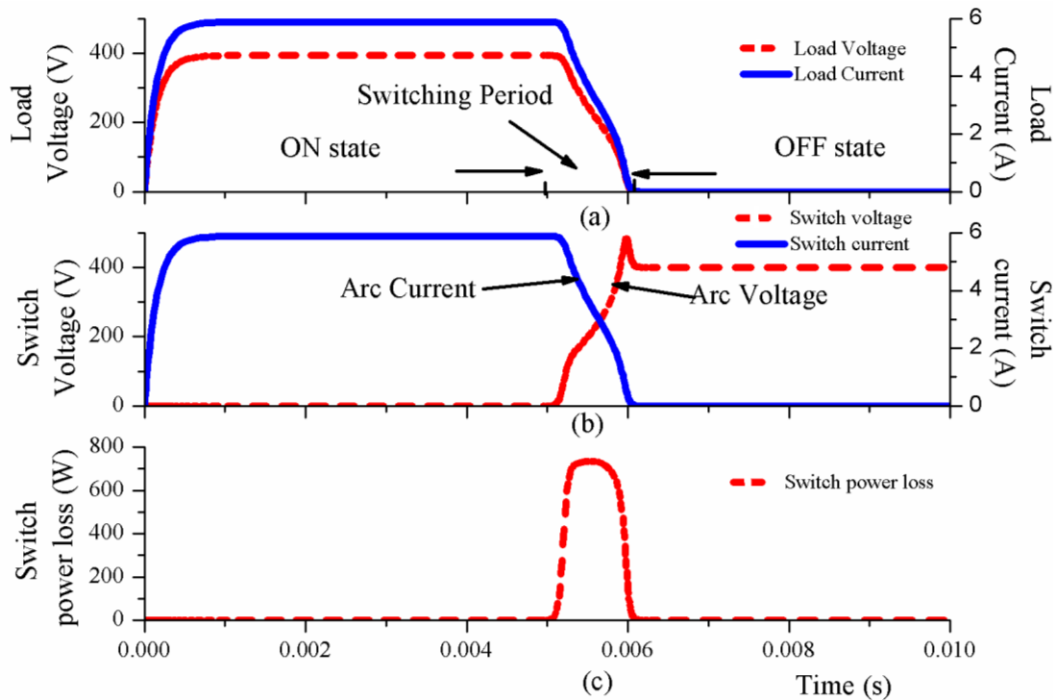


**Figure 3.3:** Simulated waveforms of DC system with mechanical switch

The simulation result in Figure 3.3(a) shows that, the voltage and current of the load starts reducing from 400V and 6A respectively at 0.005s. The load voltage and current reaches zero at 0.006s. Hence the switching period is 0.001s and the load is completely isolated from the supply. Figure 3.3(b) shows that the switch voltage increases from 0.18V to 400V and the switch current reduces from 6A to 0A. Hence it is found that the ON-state voltage drop is 0.18V and the OFF-state leakage current is zero. Figure 3.3(c) shows that the ON-state, switching period and OFF-state power losses are 1.05W, 740W and 0W respectively.

### 3.2.2 Solid-state switches

Power MOSFET, IGBT, IGCT and GTO are various solid-state switches. A DC system using power MOSFET is shown in Figure 3.4. The symbol D, S and G are the drain, source and gate terminals of the power MOSFET.  $R_s$  and  $C_s$  are the snubbers for power MOSFET.

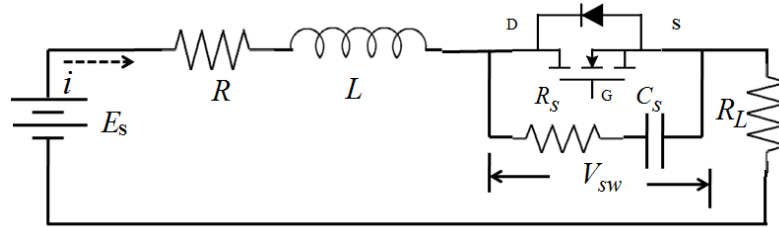


**Figure 3.4:** DC system with solid-state switch

The data of power MOSFET is taken as 400V, 6A, 1Ω from the literature (*IRF730A*) and simulation has been carried out and results are shown in Figure 3.5.

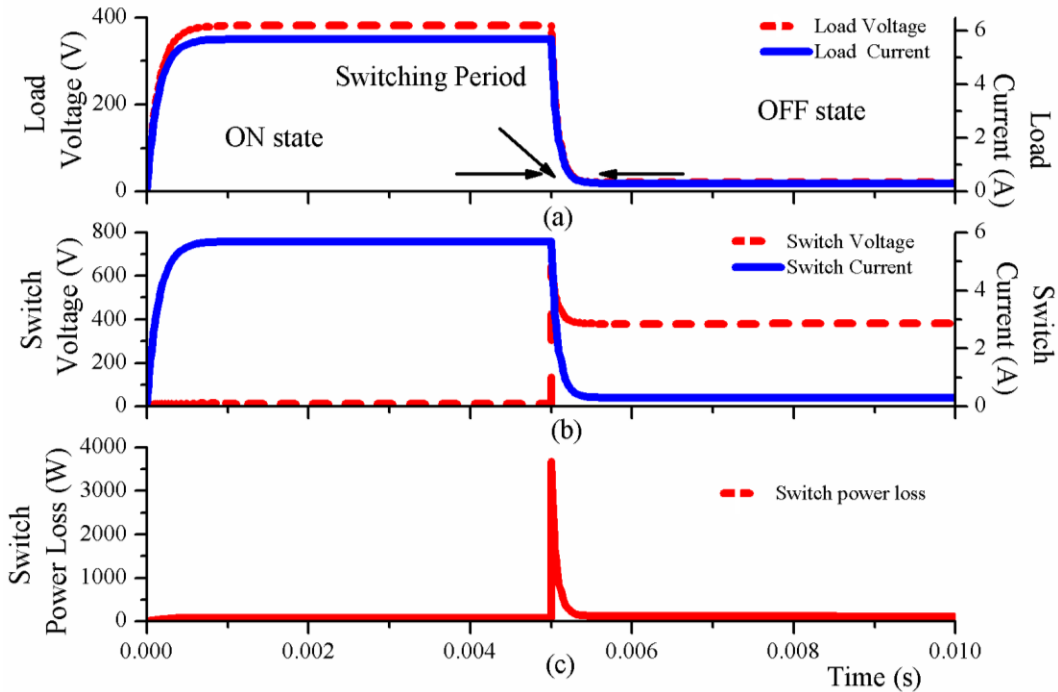


**Figure 3.5:** Simulated waveforms of DC system with power MOSFET switch

Figure 3.5(a) shows that, the load voltage and current starts reducing from 380V and 5.7A respectively at 0.005s. The load voltage and current reaches 20V and 0.3A at



0.0053s. Hence the switching speed is  $300\mu\text{s}$  and the load is not completely isolated from the supply side. Figure 3.5(b) shows that the switch voltage increases from 13.15V to 380V and the switch current reduces from 5.7A to 0.3A. It is found that the ON-state voltage drop is 13.15V and the OFF-state leakage current is 0.3A. Figure 3.5(c) shows that the ON-state, switching period and OFF-state power loss are 115W, 3700W and 75W respectively.

### 3.2.3 Solid-state switch array

The commonly available solid-state switch ratings are low. To reach the higher switch rating, solid-state switch array can be made by connecting low rating switches in array. During the operation, the operating voltage and current of the all switches must be evenly distributed and balanced across each of the individual solid-state switch. The low rating switches generally having high ON-state resistance, leads to high voltage drop and power loss. The OFF-state leakage current reduces the isolation and also causes power loss. During switching period, the peak voltages appear across each switch which increases the power loss of the switch array considerably. Hence the heat generated by the array has been increased significantly. The high power losses and negative temperature coefficients of semiconductor devices limit their scalability (Baek, Yoo and Kim, 2001. Modern electronic devices and controllers increase the controllability of solid state switches.

A DC system using  $m \times n$  array of MOSFET switches as a solid-state switch is shown in Figure 3.6. The sample data of MOSFET is taken as 40 V, 0.1A,  $8\Omega$  (EN6555A D, 2013) from the literature.  $60 \times 10$  array MOSFET switches are connected to scale up the rating 400V/ 6 A.

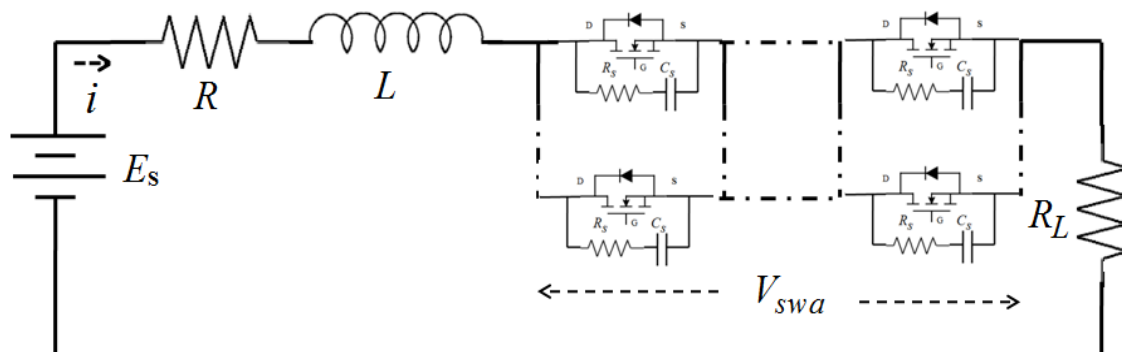


**Figure 3.6:** DC system with solid-state switch array

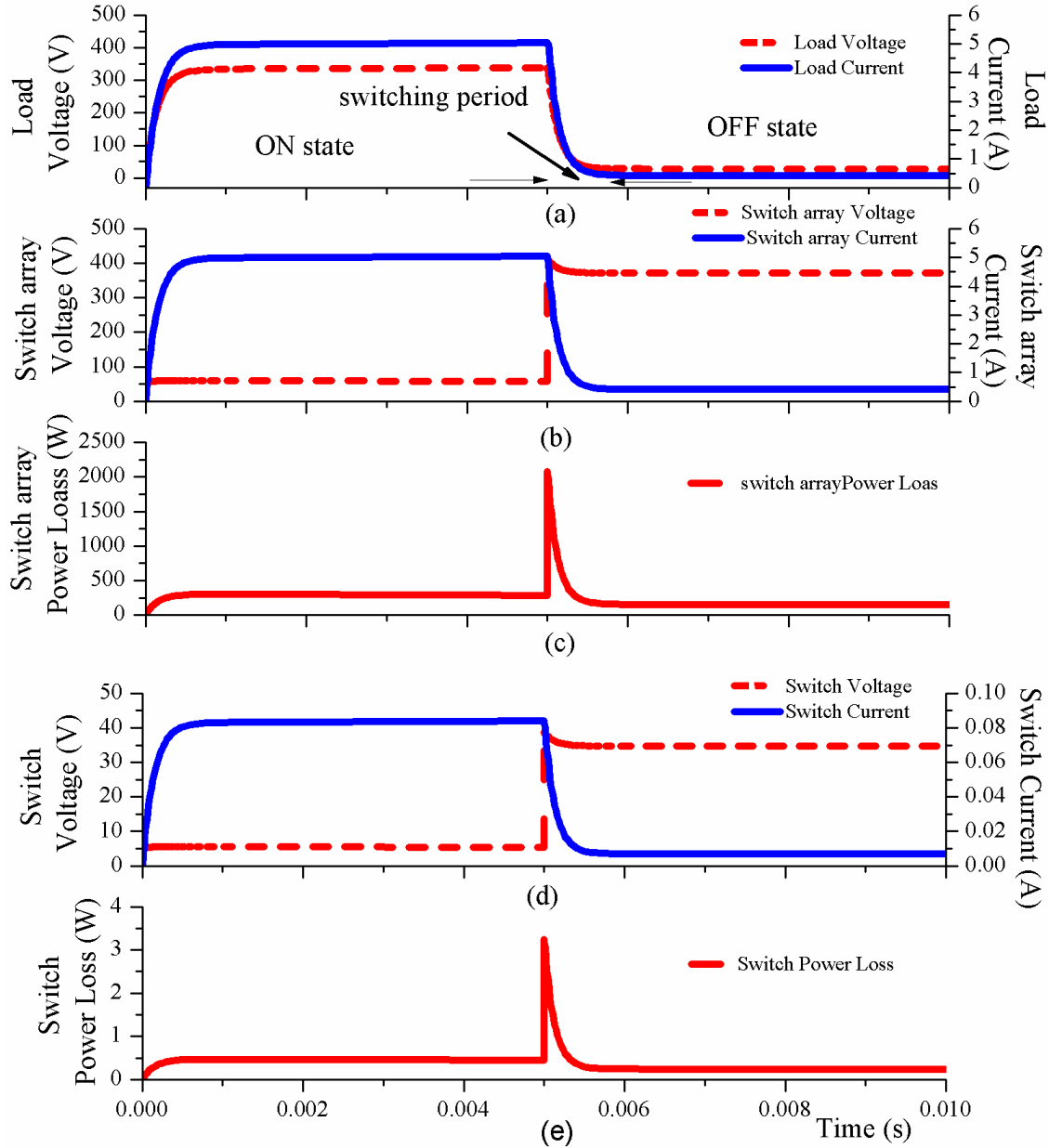


**Figure 3.7:** Simulated waveforms of DC system with array of solid-state switches

The simulation result in Figure 3.7(a) shows that, the load voltage and current are interrupted at 0.005s and reduces to 24V and 0.5A respectively. The switching time in solid-state array is also 0.0053s and the load is not isolated completely from the supply side. Figure 3.7(b) shows that, the switch array voltage increase from 55V to 372 V and the switch array current reduces from 5.5A to 0.4 A. Hence it is found that the ON-state voltage drop is 55V and the OFF-state leakage current is 0.4A. From Figure 3.7(c), ON-state, switching period and OFF-state power losses of the solid-state switch array are

found as 275W, 2250W and 155W respectively. The Figure 3.7(d) shows that the voltage across the single switch increase from 5.5 to 35V and the current flowing through the single switch reduces from 0.08A to 0.007A. Hence it is identified that the ON-state voltage drop across the single switch is 5.5V and the OFF-state leakage current is 0.007A. From Figure 3.7(e) the ON-state, switching period and OFF-state power loss of a single switch are found as 0.5W, 3.7W and 0.25W respectively.

### 3.2.4 Proposed scalable TCT micromechanical switch array configuration

Karady et al., (2005) explored Series-Parallel (SP) array topology of micromechanical switches. Photovoltaic, renewable and power distribution systems are using SP array (Bastidas et al., 2013; Chakraborty et al., 2013). In this topology, the switches are connected in series to form sub-modules (strings) and these sub-modules are connected in parallel. The disadvantage of this topology is that the failure of single switch may leads to the failure of the complete string. This is mainly implemented for cold switching conditions. Karady et al., (2005) proposes SP topology to achieve 8A, 4000V for AC power application through cold switching. Karady and Heydt (2006) designed 7.2 kV, 630A AC circuit breaker using SP array of 300×6300 micromechanical switches. Also suggested that 250×50 micromechanical switches can be fabricated in one wafer. Keimel et al., (2012) designed a 350V, 10A SP topology switching system for DC cold switching. The TCT array configuration has been explored in photovoltaic and solid-state switching applications (Bastidas et al., 2013; Chakraborty et al., 2013). Ramaraj et al., (2014) suggested that the TCT array almost doubles the life time of the system.

Figure 3.8 shows the proposed TCT micromechanical switch array configuration which is scalable to high power rating according to the requirement.  $S_{ij}$  is an individual switch and these switches are connected in series and parallel to create a switch array. All these switches are interconnected as shown in Figure 3.8. To meet the required current rating, the low current rating switches  $S_{11}, S_{21}, \dots, S_{m1}$  are connected in parallel. Thus the total current rating of switch array is equal to the sum of current ratings of all the parallel switches and is given by

$$I_{swa} = \sum_{i=1}^m I_i \quad (3.2)$$

Where  $I_i$  is the current flowing through each row switches. To reach the required voltage rating, low voltage rating switches  $S_{11}, S_{12}, \dots, S_{1n}$  are connected in series.

Now, the total voltage across the switch array  $V_{swa}$  is

$$V_{swa} = \sum_{j=1}^n V_j \quad (3.3)$$

Where  $V_j$  is the voltage across each column switches. In TCT array, the node points of the switch array are connected. Hence failure of one switch can not affect the performance of the array. The Power rating of the switch array  $P_{swa}$  is given by

$$P_{swa} = I_{swa} \times V_{swa} \quad (3.4)$$

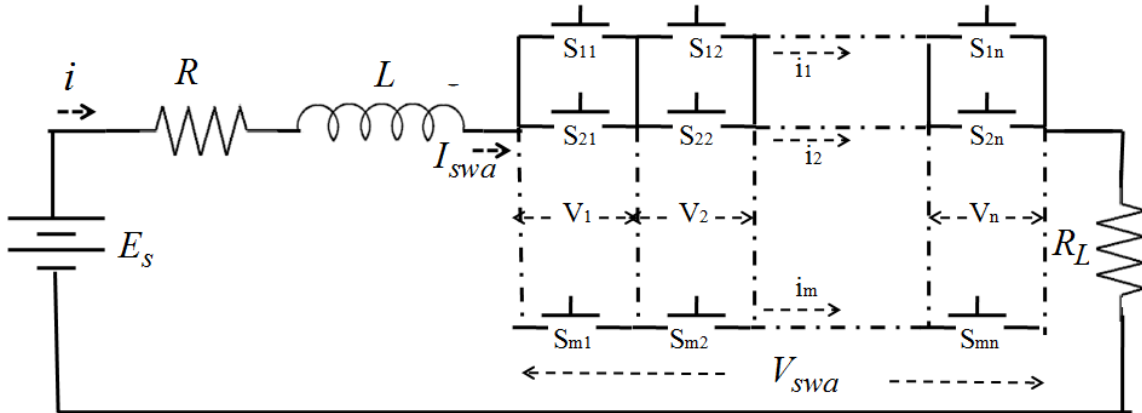


**Figure 3.8:** DC system with scalable TCT  $m \times n$  array configuration of micromechanical switches

Micromechanical switches can be designed with low rating. To achieve high rating and reliability they are connected in array. This array increases the number of devices. But the microsystem bulk fabrication technology is in favor of making many devices in a single wafer and leads to small size, weight, cost and less power consumption. The advantages of TCT micromechanical switch array is that failure of one switch will not affect the performance of the overall switch array.

The TCT micromechanical switch array is scalable to the required power rating. For example, 40V/0.1A micromechanical switches can be connected in the array of 30x5 to achieve 200V/ 3A rating and 15x10 to enhance 100V/ 6A rating.

To study the characteristics of TCT micromechanical switch array, simulation has been carried out using 40V, 0.1A, 0.01Ω micromechanical switches (Rebeiz, 2003; Hyman and Mehregany, 1999). 40 V/ 0.1A micromechanical switches are connected in 60×10 array configuration to achieve 400 V/ 6A.

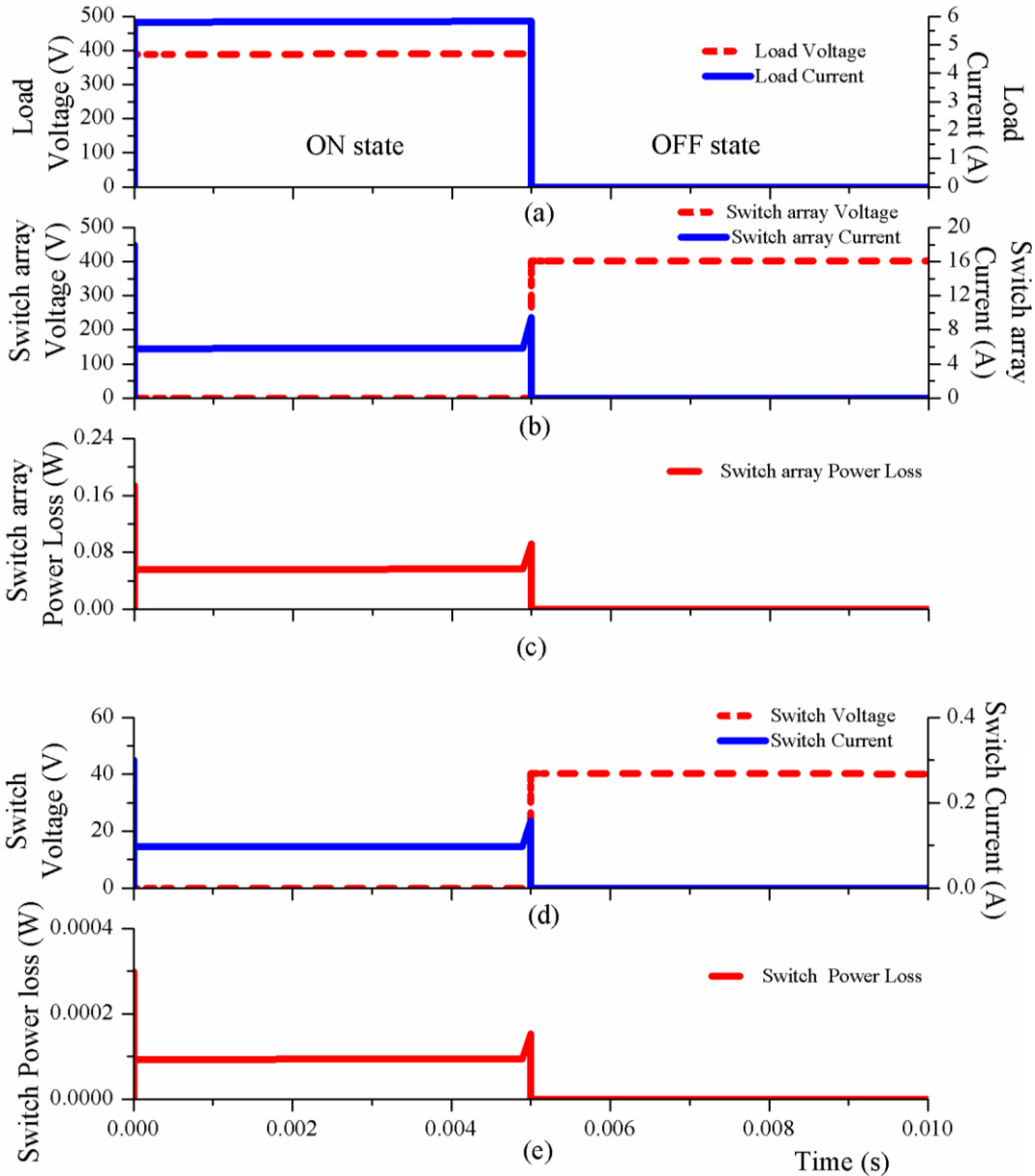


**Figure 3.9:** Simulated waveforms of DC system with TCT array of micromechanical switch configuration

From Figure 3.9(a), it is found that the load voltage and current are interrupted and reduces from 398V, 6A to 0V, 0A. It shows that the load is completely isolated from the supply side. Figure 3.9(b) shows that, the switch array voltage increases from 0.01V to 400V and the current reduces from 6A to 0A. Hence the ON-state voltage drop is 0.01V and the OFF-state leakage current is 0A. When the TCT array switches from OFF-state to ON-state, the peak current of 18A flows through the array at 0s. During transition from ON-state to OFF-state, peak current of 11A flows through the TCT array at 0.005s. From Figure 3.9(c) it is identified that the ON-state and OFF-state power losses of switch array are 0.055W and 0 W respectively. When the TCT array switches from OFF-state to ON-state, peak power of 0.18W appears across the array. Power of 0.09W appears across the array during the transition of array from ON-state to OFF-state. Figure 3.9(d) shows that the switch voltage increases from 0.001V to 40V and switch current reduces from 0.1A to 0A. Hence the ON-state voltage drop is 0.001V and the OFF-state leakage current is 0A. During the transition from OFF-state to ON-state of a single switch, peak current of 0.5A flows through the switch at 0s. During transition from ON-state to OFF-state, peak current of 0.18A flows through the switch at 0.005s. Figure 3.9(e) gives the ON-state and OFF-state power losses of each micromechanical switch as 0.0001W and 0W respectively. When the single switch switches from OFF-state to ON-state, peak power of 0.3mW appears across the switch. Power appears across each switch of the array during the transition from ON-state to OFF-state is 0.19mW.

### **3.2.5 Comparative analysis of switches in DC system**

The results obtained from above analysis are summarized and presented in Table 3.2. The ON-state and OFF-state parameters of the electromechanical switches, solid-state switch and solid-state switch array are compared with the proposed scalable TCT micromechanical switch array configuration. The voltage drop and power loss of micromechanical switch array in the ON-state is 0.01 and 0.055 respectively. The ON-state voltage drop of TCT micromechanical switch array is 18 times lesser than mechanical switch. The OFF-state current and power loss are equal to zero. Hence it is clear that the proposed system will give better performance in terms of voltage drop, leakage current and power loss. The simulation result shows the voltage, current and power characteristics of single switch and TCT array of switches. It also shows that, peak power

appears across the switch during switching period. The results obtained through the conceptual model are used for further analysis towards the design of scalable, arcless micromechanical switches for power applications.

**Table 3.2:** Simulation results and quantitative comparison for DC system

State	Parameters	Mechanical switch	Solid-state switch	Solid-state switch array	Proposed Scalable TCT micromechanical switch array
ON	Voltage drop (V)	0.18	13.15	55	0.01
	Power loss (W)	1.05	115	275	0.055
OFF	Leakage current (A)	0	0.3	0.4	0
	Power loss (W)	0	75	155	0

### 3.3 Characteristics of AC System

An equivalent AC system is considered to evaluate the characteristics of various switches, and is shown in Figure 3.10. The AC system contains a sinusoidal voltage source  $E_s$  (rms), resistance  $R$  and inductance  $L$  are connected in series with a resistive load  $R_L$  through a switch.

$$E_s = E_m \sin \omega t \quad (3.5)$$

Where  $E_m$  is the maximum source voltage,  $\omega$  is the angular frequency and  $t$  is the time.

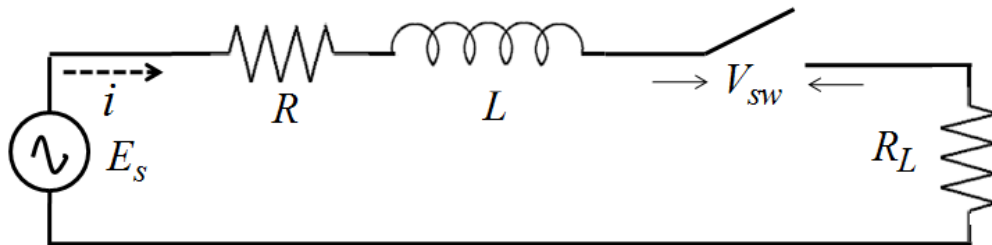


**Figure 3.10:** AC equivalent electrical system

The parameter values considered for the AC equivalent circuit is given in Table 3.3. The source voltage considered is  $E_s = 230V(rms)$ . The simulation has been carried out using MATLAB Simulink tool for analyze the characteristics of various switches. The simulation carried out between 0 and 0.06s. The control signal is given to open the switch at 0.025s.

**Table 3.3:** Parameters of AC system

Parameter	Symbol	Value	Unit
Source Voltage	$E_m$	325	V
Load Resistance	$R_L$	67	$\Omega$
Resistance	$R$	1	$\Omega$
Inductance	$L$	0.01	H

This equivalent AC system is analyzed with mechanical, solid-state and proposed scalable TCT array of micromechanical switches for the rating of 230V (rms), 6A. This supply has the maximum voltage of 325V. The performance parameters are obtained through simulation using MATLAB Simulink. Simulation has been carried out for the time period of 0 to 0.06s. The switch is kept in ON-state for the time period less than 0.25s. At 0.025s, control signal is given to the switch to make the switch OFF.

### 3.3.1 Mechanical switch

The switch parameter of 325V (max), 6A, 52.1m $\Omega$  (ABB, 2011) has been considered and simulation is carried out to evaluate the characteristics of mechanical switch. The simulation has been carried out for the circuit given in Figure 3.10 with the mechanical switch and the results are shown in Figure 3.11. Figure 3.11(a) shows the AC source voltage. Figure 3.11(b) shows that at 0.025s, the load voltage and load current starts reducing and become zero at 0.03s. The switching speed is obtained as 5ms. Figure 3.11(c) shows that the maximum switch voltage increases from 0.3V to 325V and the maximum switch current reduces from 6A to 0A. The maximum ON-state voltage drop is 0.3V and OFF-state leakage current is zero. Figure 3.11(d) shows the maximum ON-state, switching period and OFF-state power loss are 1.25W, 70W and 0W respectively.



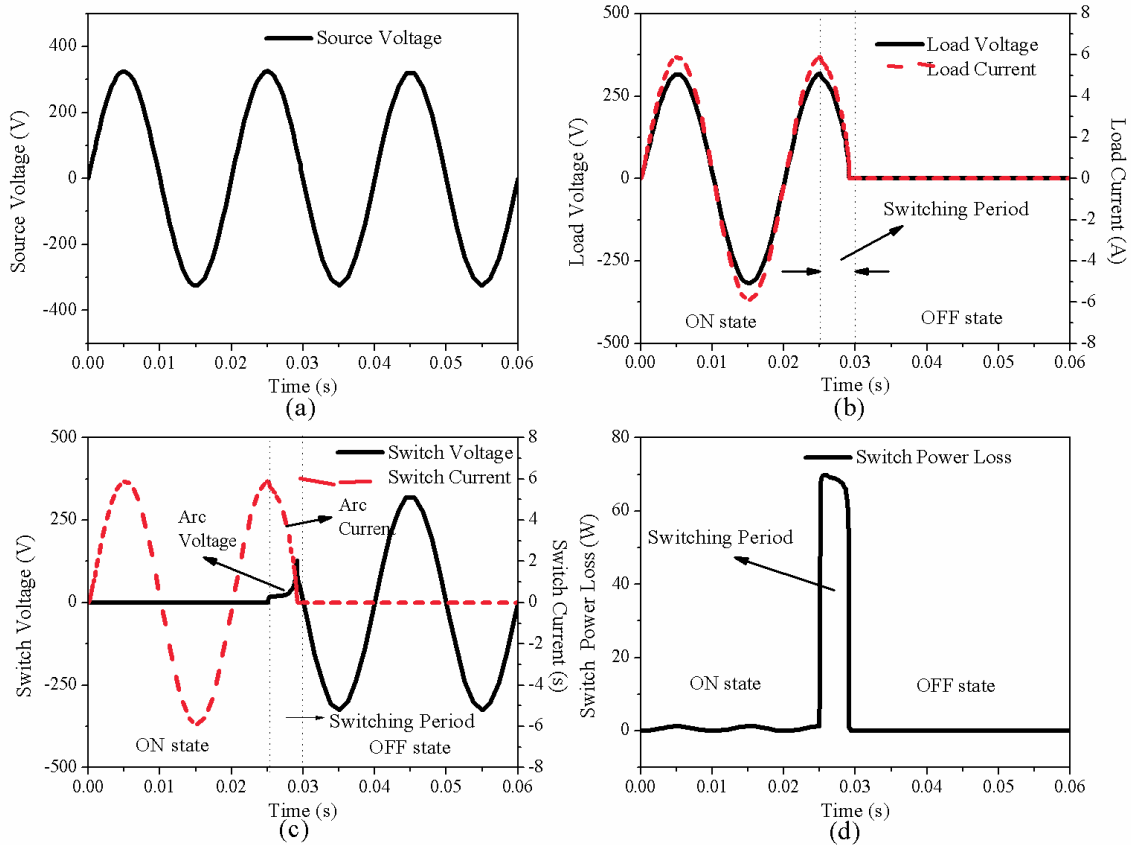


**Figure 3.11:** Simulated waveforms of AC system with mechanical switch

### 3.3.2 Solid-state switch

An AC system using GTO as a solid-state switch is shown in Figure 3.12. Two GTOs are connected in anti-parallel to block positive cycle and negative cycle voltages. A, K and G are the anode, cathode and gate terminals of the power GTO. The simulation uses power GTO parameters 325V, 6A, and  $5\Omega$  (Woodworth, 1981).

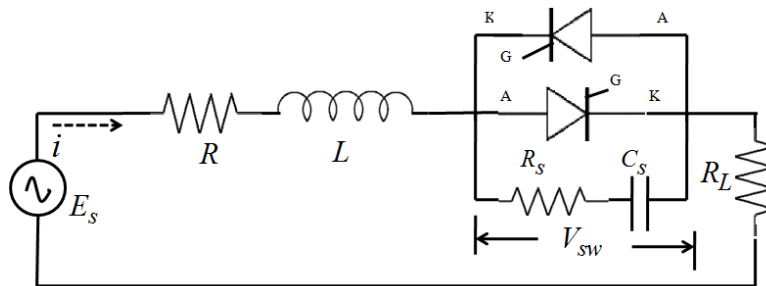


**Figure 3.12:** AC system with GTO switch

From Figure 3.13(b) it is identified that the load voltage and current are interrupted at 0.025s and reduce to non-zero value, hence the switching speed is 600 $\mu$ s. Figure 3.13(c) shows that the maximum switch voltage increases from 28V to 313V, the maximum switch current reduces from 5.4A to 0.2A. The maximum ON-state voltage drop and OFF-state leakage current are identified as 28V and 0.2A respectively. Figure 3.13(d) shows the maximum power loss during ON-state, switching period and OFF-state are 105W, 11300W and 26W respectively.

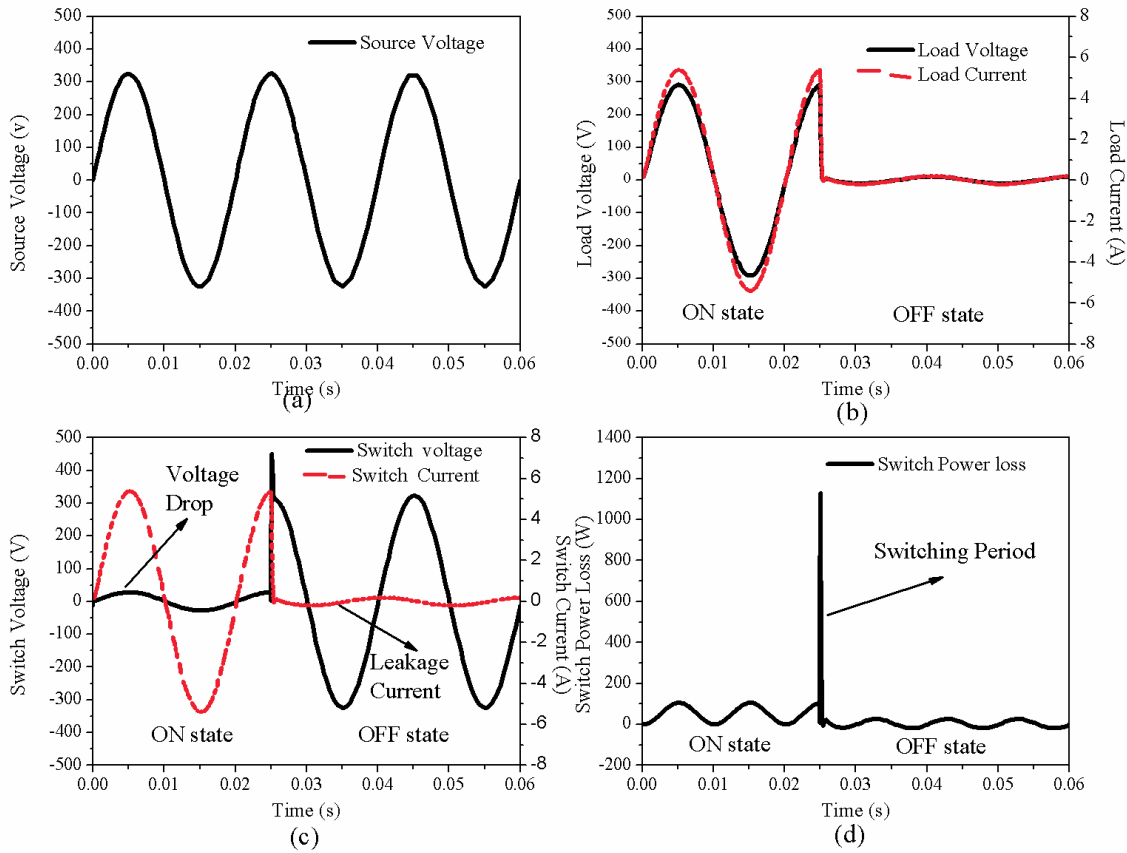


**Figure 3.13:** Simulated waveforms of AC system with solid-state switch

### 3.3.3 Proposed scalable TCT micromechanical switch array

For analysis a 33V, 0.4A (max), 0.01 $\Omega$  (Rebeiz, 2003; Hyman and Mehregany, 1999) micromechanical switch has been considered and 15 $\times$ 10 switches are connected as a TCT array to achieve the rating of 325V/6A. Simulation has been carried out for the proposed circuit shown in Figure 3.8 with the AC supply and results are shown in Figure 3.14.

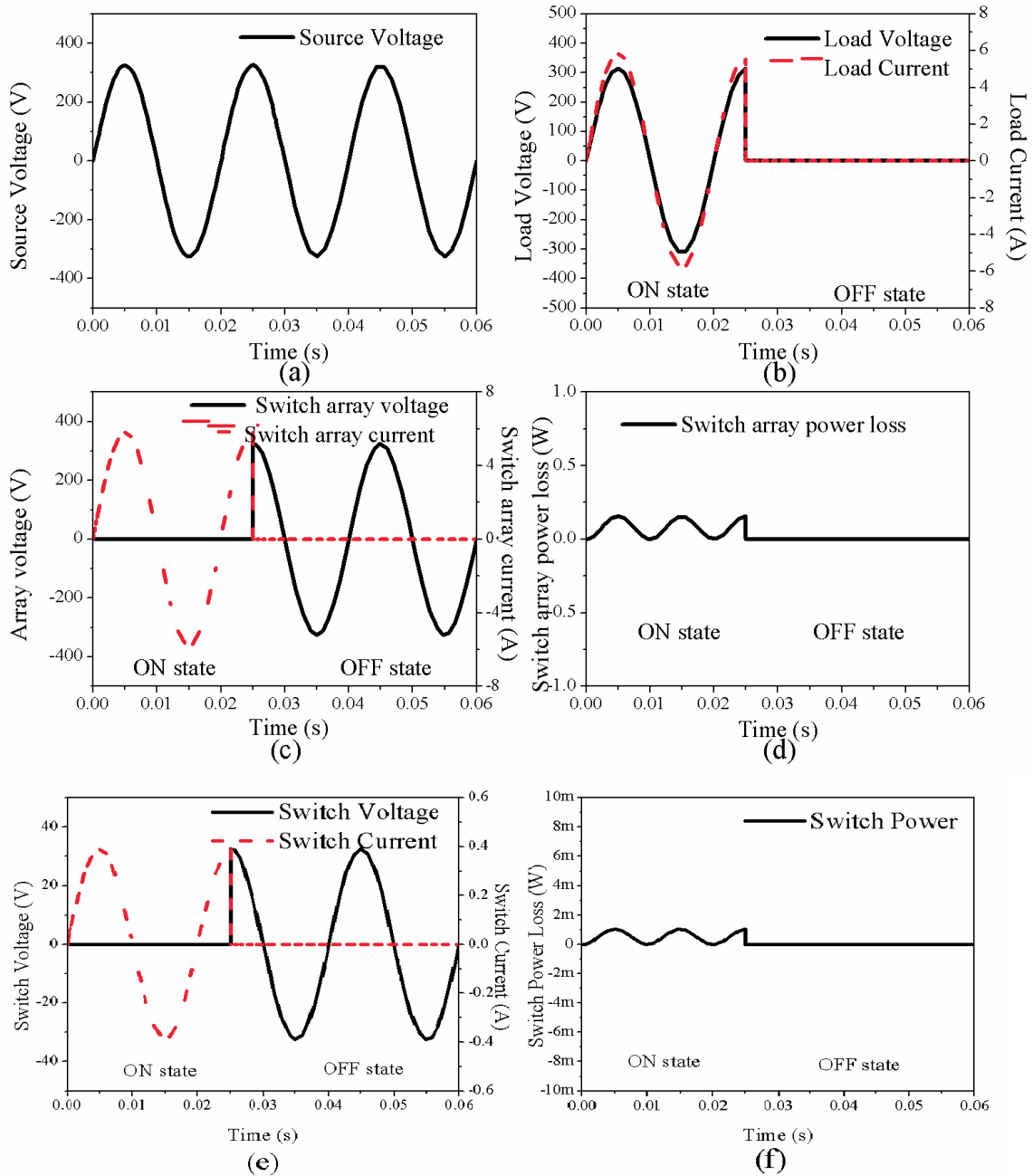


**Figure 3.14:** Simulated waveforms of AC system with TCT array of micromechanical switch configuration

Figure 3.14(a) shows the source voltage. Figure 3.14(b) shows that, maximum load voltage increases from 325V to 0V and the maximum load current reduces from 5.8 to 0A. Figure 3.14(c) shows that, the maximum array voltage increase from 0.03V to 325V and the maximum array current reduces from 5.8A to 0A. Hence the maximum ON-state

voltage drop is 0.03V and the maximum OFF-state leakage current is 0A. Figure 3.14(d) shows that the ON-state and OFF-state power loss of switch array are 0.16W and 0W respectively. Figure 3.14(e) shows that the switch voltage increases from 0.0035V to 32.5V and the switch current reduces from 0.39A to 0A. The switch voltage drop and leakage current are 0.0035V and 0A respectively. Figure 3.14(f) shows that the ON-state and OFF-state power losses are 1mW and 0W respectively.

### 3.3.4 Comparative analysis of switches in AC system

The results are summarized and presented in Table 3.4. The ON-state and OFF-state parameters of the mechanical and solid-state switches are compared with the proposed scalable TCT micromechanical switch array configuration. The voltage drop and power loss of micromechanical switch array in the ON-state is 0.03V and 0.16W. The voltage drop of micromechanical switch array is 10 times lesser than mechanical switch. The power loss of the micromechanical switch array is 7.8 times lesser than mechanical switches. For micromechanical switch array, the OFF-state current and power loss are zero. Hence it is clear that the proposed system will give good performance in terms of voltage drop, leakage current and power loss.

In micromechanical switches, the physical gap provides isolation and zero leakage current. But in case of solid-state switches, Absence of physical gap increases the resistance and reduces the isolation. Also the solid-state devices made up of semiconductor materials which have very high resistance. This leads to high voltage and power losses. In micromechanical switches the conducting parts are made up of conductive materials which have less resistance. This results in low voltage drop and power losses.

**Figure 3.4:** Simulation results and quantitative comparison for AC system

State	Parameters	Mechanical switch	Solid-state switch	Proposed Scalable TCT micromechanical switch array
ON	Voltage drop (V)	0.3	28	0.03
	Power loss (W)	1.25	105	0.16
OFF	Leakage current (A)	0	0.2	0
	Power loss (W)	0	26	0

### **3.4 Actuation Techniques of Micromechanical Switch for Power Applications**

A micromechanical switch has ON-state and OFF-state. Switching between these two states can be achieved through the movement of a free moving cantilever beam. The movement can be obtained using different types of actuation mechanisms like piezoelectric, thermal, magnetic and electrostatic.

#### **3.4.1 Piezoelectric micromechanical switches**

The piezoelectric effect was discovered by Piere and Jacques Curie. Certain materials such as quarts, piezoceramics, piezopolymers, piezocomposites and single-crystal materials produces mechanical stress on their surface on the application of electric charges and vice versa. This phenomenon is called the piezoelectric effect. Materials showing this phenomenon also conversely have a geometric strain proportional to an applied electric field. The Piezoelectric effect is extensively utilized in various devices such as transducers, sensors and actuators (Kanno, 2013). In piezoelectric micromechanical switches, very high driving voltage is required even for very small displacement  $1\mu\text{m}$  (Yoichi, 2006). This high voltage leads to occurrence of arc.

#### **3.4.2 Thermally actuated micromechanical switches**

Yeatman, (2007) developed thermally actuated micromechanical switches for power applications. In thermally actuated micromechanical switches, the beam movement is due to the thermal expansion. The thermal switches having large current handling capability but the switching speed is very low in the range of  $100\mu\text{s}$  to  $5000\mu\text{s}$ . This is due to the time required to heat the structure (Gear et al., 2004). If the switching speed is less, then the possibility for occurrence of arc is more (Kaiser, 2005).

#### **3.4.3 Electromagnetic micromechanical switches**

Magnetic micromechanical switches having the cantilever beam structure has the ability to bend in the application of a magnetic field. A permanent magnet is placed near the microstructure to actuate the beam and closes the switch. This creates closed current conduction path. A coil is used to open the switch by creating a magnetic field equal and opposite to the field produced by the permanent magnet, which restores the beam due to spring force and thereby creating a dynamic equilibrium. The switches are coupled by the permanent magnet in the normally closed position. Magnetically actuated switches have

relatively less switching speed in the range of 100 $\mu$ s to 2000 $\mu$ s. The ON-state current handling capability is 0.01A to 1A with a low contact resistance. The voltage handling capability is low when compared to electrostatic switches (Raychowdhury et al., 2013; Shobak et al., 2011). The structure of electromagnetic micromechanical switch is more complex. The size of these switches are comparatively 20 times more than piezoelectric, thermal and electrostatic micromechanical switches. These switches may lead to arc due to low switching speed.

#### **3.4.4 Electrostatic micromechanical switches**

Electrostatic switches need actuation (driving) electrodes, which are placed at the bottom of cantilever beam and top of silicon base. When an actuation signal is applied across the driving electrode, the beam is pulled down by induced electrostatic force. Hence, current flow is permitted by the connection of the microelectrical contact. Reducing the voltage across the driving electrode leads to opposing electrostatic force leads to upward movement of beam. Hence, current flow gets interrupted. Electrostatically actuated switches have dominated in many applications due to their linearity, very low OFF-state capacitance and relatively fast switching speed in the range of 0.1-200 $\mu$ s. The ON-state current handling capability is around 0.4A with a low contact resistance. The OFF-state isolation is higher and the voltage handling capability varies from 20 to 300V. ON-state resistance of electrostatic switch is in the range of 10-200m $\Omega$  and OFF-state capacitance is in femto Farad. The contact gap of these switches is from 2 $\mu$ m to 7 $\mu$ m (Raychowdhury et al., 2013, Shobak et al., 2011).

Electrostatic actuation does not consume current, hence the power consumed for actuation is zero. These switches are compatible with electronic chip fabrication. Ma et al., (2015) and Keimel et al., (2012) explored the use of electrostatically actuated micromechanical switches for power applications. Electrostatic micromechanical switches have simple, fabrication compatible structure and scalability supportive (Song, 2016).

Table 3.5 summarizes the characteristics for different types of micromechanical switches. The comparison clearly indicates that electrostatically switches are very promising for low ON-state resistance, fast switching speed, compatible manufacturability and integrability with VLSI circuits. From above mentioned switches, electrostatic actuated

switches have reliable design, good performance and are entering into volume production for commercial applications. The electrostatically actuated micromechanical switches also produces arc. But arcless switching can be achieved through proper design of the micromechanical switch.

**Table 3.5:** Comparison of micromechanical switches on the basis of actuation technique (Keimel et al., 2012; Lu et al., 2006; Shalaby et al., 2009; Song et al., 2012; Raychowdhury et al., 2013; Wong, Lang, and Schmidt, 2000; Shobak et al., 2011; Song, 2016)

Switch Criteria	Piezoelectric switch	Thermal switch	Magnetic switch	Electrostatic switch
ON-state resistance ( $\Omega$ )	500	0.05 - 0.25	50 m	10 - 200 m
Current handling (mA)	1 - 1000	10 - 2000	10 - 2000	0.1 - 400
Switching time ( $\mu$ s)	10 - 500	100 - 5000	100 - 5000	0.1 - 200
Actuation voltage (V)	5 - 50	0.5 - 5	1 - 5	5 - 100
Bias Current (mA)	0	0.5 - 5	20 - 150	0
Area ( $\mu\text{m}^2$ )	200 x 200	200 x 200	5000 x 4000	250 x 250
Size	Small	Small	Large	Medium
Manufacturability	Incompatible	Compatible	Incompatible	Compatible
Integrability to VLSI circuit	Incompatible	Incompatible	Incompatible	Compatible

### 3.5 Proposed Electrostatically Actuated Micromechanical Switch

Micromechanical switches use mechanical movement to achieve ON-state and OFF-state in the electrical system. Micromechanical switches are categorized by their configuration as shunt and series. Based on the nature of the switching contact, these switches are classified in to capacitive and metal-metal contact. Usually shunt switches are based on fixed-fixed beam and are more suitable for capacitive switching for high frequency and RF applications. The series type switches uses cantilever beam fixed at one end and the other end is freely moving (Noel, 2016; Rebeiz, 2003). For power switching applications, the contact should be metal-metal contact type. Cantilever based switches are preferred

because of its simple configuration and easy wiring (Khushalani, Pande, and Patrikar, 2016). The proposed structure of electrostatically actuated micromechanical switch is shown in Figure 3.15.

The electrostatically actuated micromechanical switch has a silicon base. The micromechanical switch has a cantilever beam which is anchored at one end and the other end is freely moving. The electrostatic actuation is carried out by a set of driving electrode, one on the base and another is fixed on the bottom of the cantilever beam. The upper and lower driving electrodes are connected to the positive and negative terminal of the DC voltage source. The microelectrical contact is placed at the tip of the cantilever beam which allows and interrupts the electric current in a DC and AC system. The microelectrical contact has two fixed electrodes and a floating electrode. The bottom of the free end of the cantilever beam has floating electrodes. One of the fixed electrode connected to the source is anode and the electrode which is connected to the negative terminal of the source is cathode. Anode and cathode are fixed on the silicon base. The floating contact is neither connected to the positive nor to the negative of the source. When driving (actuation) voltage is applied between driving electrodes, driving force develops and pulls the cantilever beam down. Hence the floating electrode come in physical contact with the anode and cathode, the switch become ON-state. This creates a continuous current conduction path in the electrical system. The driving voltage can be reduced to move the beam up and the micromechanical switch become OFF-state and hence the current flow gets interrupted.

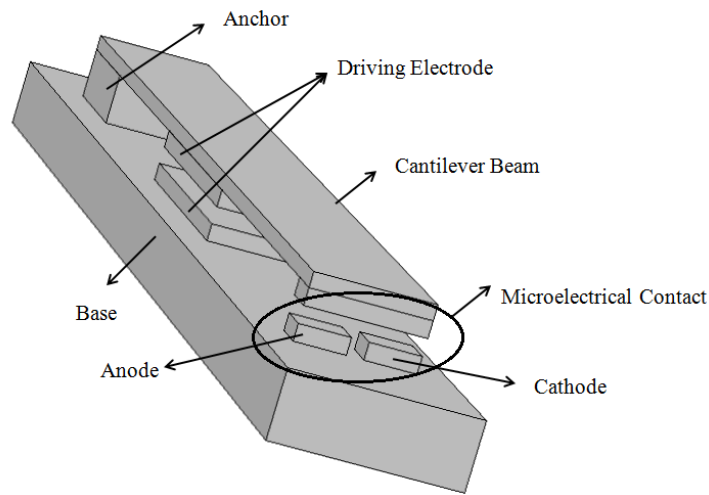


**Figure 3.15:** Electrostatically actuated micromechanical switch



This micromechanical switch can be used for both AC and DC power switching applications. During the switching operations, arc may occur in the micromechanical switch. Both AC and DC power can lead to arc. The presence of arc leads to damage and failure of the switch.

### **3.6 Arcless Switching**

In case of AC, switching at natural zero crossing of sinusoidal voltage or current waveform may lead to arcless switching. Arc occurs, if the switching has been carried out at non-zero point. But, the arc gets extinguished quickly at the next natural zero crossing point of the supply voltage or current (Meyer, Kowal, and De Doncker, 2006). Achieving arcless switching in DC electrical system is challenging because of the non-zero steady supply voltage (Saeedifard et al., 2010). Hence further analysis has been carried out for DC power switching.

#### **3.6.1 DC power switching**

The recent development of power electronic based converters, solar power generating systems and electrical energy storage devices increases the opportunities of DC electric power system. Shipboard power systems, electric aircrafts, battery operated systems, electric traction systems, battery protection, home appliances, smart grid and residential microgrid etc., are utilizing DC power in order to take advantage on efficiency, flexibility and quality. Hence, there has been ample attention to develop DC switching devices (Tabari and Yazdani, 2015; Huang et al., 2015; Meyer, Kowal, and De Doncker, 2006). In order to reduce the electric power consumption, the demand based switching of these applications is needed and has to be controlled automatically to make the system smarter. Therefore, a good functionality current interrupting device with high reliability is needed. Reliability depends on many factors. One of the important factor is occurrence of arc. For the micromechanical switch shown in Figure 3.15, arc occurs in four parts of the switch.

### **3.6.2 Arc occurring parts**

Arc can occur in four parts of the micromechanical switch.

#### ***Driving Electrode***

Driving electrode has non-touching contacts. The driving voltage is given across the electrode which moves the cantilever down. The driving voltage can cause ionization of air present between the driving electrodes. The detailed analysis is carried out in chapter 4.

#### ***Microelectrical contact***

The microelectrical contact is responsible for allowing and interrupting the electric current. During ON-state, it is a touching contact. As observed in Figure 3.9(d), section 3.2.4, the current flows through the microelectrical contact and the voltage across the contact is zero. Hence the current carrying capability needs to be analyzed. If the current flows through the microelectrical contact exceeds the current carrying capability, which leads to contact welding. Also, from Figure 3.9(e), section 3.2.4, it is observed that peak power appears across the microelectrical contact during switching. This power increases the temperature and leads to melting and evaporation of the microelectrical contact. This causes pre-breakdown (metal) arc. The detailed investigation has been carried out in chapter 5.

#### ***Anode-cathode***

During OFF-state, the floating electrode won't touch the anode and cathode. Hence, at this stage microelectrical contact is a non-touching contact. As observed in Figure 3.9(d), section 3.2.4, the voltage appears across the microelectrical contact and the current is zero. This voltage may cause arc across anode and cathode due to ionization of air. The arcless design of anode-cathode is also analyzed in chapter 5.

#### ***Driving electrode and microelectrical contact***

Arc may even occur between driving electrode and the microelectrical contact. As observed in Figure 3.9(d), section 3.2.4, voltage appears across the microelectrical contact. The potential difference between driving electrode and the microelectrical contact also may causes occurrence of arc. This is also due to ionization of air present between the contacts.

### 3.7 Conclusion

The following conclusions were made from the conceptual modeling and analysis of TCT array configuration of micromechanical switches.

- Scalable TCT array configuration using  $m \times n$  micromechanical switches has been proposed to increase the power rating.
- Micromechanical switches with the rating of 40V, 0.1A, 0.01 $\Omega$  are connected in 60 $\times$ 10 scalable TCT array configuration to achieve 400V, 6A DC system. The array gives voltage drop of 0.01V, power loss of 0.055W and leakage current of 0A. It is observed that peak power appears across the switch during switching period. The conceptual configuration of TCT array of micromechanical switch is compared with mechanical, solid-state and solid-state array switches. The proposed array gives 10 times less leakage current, voltage drop and power losses than mechanical switches.
- Micromechanical switches with the rating of 33V, 0.4A, 0.01 $\Omega$  are connected in 15 $\times$ 10 scalable TCT array configuration to achieve rating of 325V, 6A AC system. The maximum voltage drop, power loss and leakage current are obtained as 0.03V, 0.16W and 0A respectively.
- It is found that electrostatic switches are more suitable for power switching applications because of zero actuation power, switching speed in the order of microseconds and CMOS compatible fabricatability.
- The structure of the micromechanical switch suitable for the power application is presented. The arc occurrence parts of the micromechanical switch also has been presented. The detailed analysis in these arc producing contacts are presented in the following chapters.

# CHAPTER 4

## MODELING AND ANALYSIS OF ARCLESS DRIVING ELECTRODE

### 4.1 Introduction

TCT array configuration of micromechanical switch and the structure of electrostatically actuated micromechanical switches are described in chapter 3. For power switching applications, each switch present in the array should be arcless in order to enhance reliability. In an electrostatically actuated micromechanical switch, arc occurrence is very significant in the driving electrode and in the microelectrical contact. In order to achieve arcless switching both driving electrode and microelectrical contact should be arcless. In this chapter, the design of arcless driving electrode is discussed in detail.

Driving electrodes form a non-touching metal plate. Voltage applied across the driving electrode results in driving force. This force moves the cantilever beam downwards so that the switch become ON-state. Release of voltage moves the beam upward and the switch is in OFF-state. During OFF-state of the switch, the driving electrode has the parallel plate structure and in the ON-state, it forms a non-parallel plate structure. Since the driving electrode is a non-touching contact, no current flows through the contact. Hence the power consumed or dissipated across the electrode is zero (Sterner et al., 2010). But driving voltage appears across the driving electrodes.

The voltage applied across the non-touching electrodes creates electric field. This electric field ionizes the air between the electrodes and leads to breakdown arc. The voltage at which arc occurs is called as breakdown voltage and the electric field at which arc occurs is called breakdown electric field (Okawa et al., 1988). The breakdown voltage for centimeter and millimeter gap is extensively studied by Paschen curve (Kuffel et al., 2000). For micrometer gaps, the breakdown voltage is discussed using Paschen curve and modified Paschen curve (Go and Pohlman, 2010).

In this chapter, the structure of the driving electrode during OFF-state and ON-state are discussed. The modified Paschen curve is presented for Al, Cu, Au and Pt driving electrodes for air medium at room temperature and atmospheric pressure. The boundary

between arc and arcless region are identified. The capacitance and electric field during OFF-state and ON-state are obtained for various size of the driving electrode with various gaps. The capacitance and electric fields are obtained using mathematical modeling and the results are compared with FEM simulation. The electric field distribution is also obtained for different voltage levels. The occurrence of arc in the driving electrode is discussed. This analysis also can be applicable for the design of devices such as microactuators and microsensors in which micro gaps are present.

## 4.2 Structure of the Driving Electrode

The structure of driving electrode present in the proposed electrostatically actuated micromechanical switch is given in Figure 4.1. The driving electrode has parallel plate arrangement. One of the plate is fixed on the cantilever beam, along with cantilever movement, this plate also moves. Another plate of the driving electrode is fixed on the base. The driving electrode is a non-touching electrode and made up of conducting metal. It is considered that both plates are of same dimension and similar material. During OFF-state, the air gap of  $g_d$  is present between the driving electrodes as shown in Figure 4.1(a).  $L_d$  is the length,  $t_d$  is the thickness and  $W_d$  is the width of the driving electrode. During ON-state, the air gap of  $g_{d1}$  and  $g_{d2}$  is present between the driving electrodes as shown in Figure 4.1(b).

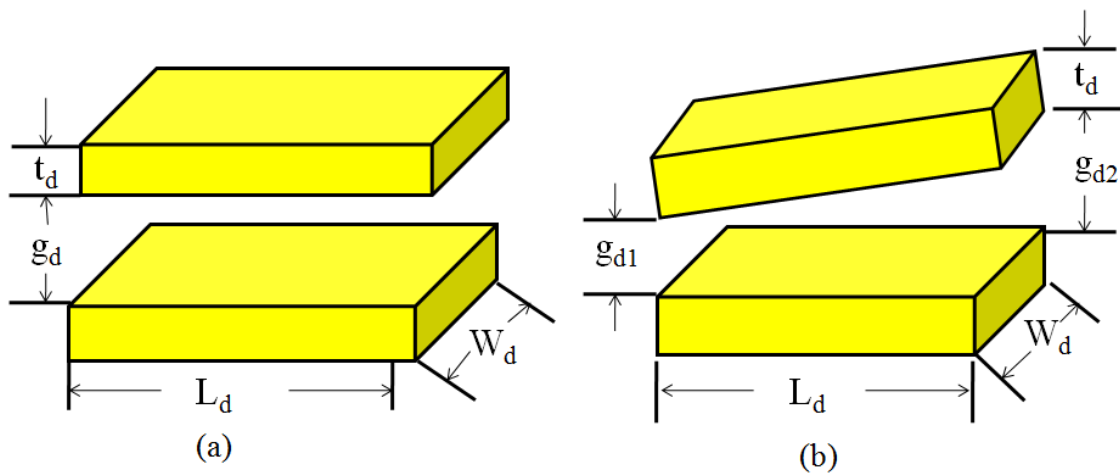


**Figure 4.1:** Driving electrode during (a) OFF-state (b) ON-state

The driving voltage applied across the electrodes produces electric field. This electric field depends on the capacitance of the driving electrode. Hence in order to design arcless driving electrode, the capacitance and electric field appears across the electrodes needs to be analyzed. This analysis is carried out for both OFF-state and ON-state of the micromechanical switch.

The capacitance and electric field of the driving electrode are obtained using mathematical modeling and the results are verified using FEM simulation. This analysis has been carried out for three cases with different size of the driving electrode. Also these three cases are analyzed for four different voltage levels and the occurrence of breakdown arc is discussed using modified Paschen curve. The dimensions of considered three cases are given as follows:

Case 1:  $L_d = 30\mu\text{m}$ ,  $W_d = 30\mu\text{m}$ ,  $t_d = 2\mu\text{m}$

Case 2:  $L_d = 30\mu\text{m}$ ,  $W_d = 60\mu\text{m}$ ,  $t_d = 5\mu\text{m}$

Case 3:  $L_d = 50\mu\text{m}$ ,  $W_d = 50\mu\text{m}$ ,  $t_d = 10\mu\text{m}$

### 4.3 Breakdown Arc Analysis

In general, air is an insulator. However, when high voltage appears across the electrodes, the air present between the electrodes becomes relatively conductive. This phenomenon is called as the electric breakdown of the air. If the voltage is sufficiently high, electrical breakdown of the air occurs and leads to electrical spark or arc which bridges the gap.

The electrical breakdown voltage is the voltage at which arc appears between two electrodes separated by gaseous medium. The breakdown voltage depends on the medium between electrodes, temperature, pressure and material of the electrode. In general, the electrical breakdown is based on Townsend (avalanche) breakdown in air. The application of voltage across the electrodes induces electric field. Due to this electric field, the electrons gain enough energy between successive collisions with neutral atoms to ionize the atoms. This ionization releases additional electrons which also accelerate, collide with atoms and cause more ionization. This resulting avalanche leads to arc. Paschen curve and modified Paschen curve gives the breakdown voltage, which is the voltage required to produce electric arc (Go and Pohlman, 2010).

### 4.3.1 Breakdown arc analysis using Paschen curve

The breakdown voltage has been explored for gap formed by sphere-sphere, needle-plate and plate-plate electrodes (Chen et al., 2006; Lee et al., Chung, 2001). The breakdown voltage for centimeter and millimeter gap is given by the Paschen's law. It states that the breakdown voltage  $V_b$  is the function of the product of the air pressure and the gap between the electrodes, and written as  $V_b = f(pg_d)$ , where  $p$  is the pressure and  $g_d$  is the gap between the electrodes (Kuffel et al., 2000). Paschen curve law has been successfully employed in millimeter scale gaps and centimeter gaps.

The Paschen curve describes the gaseous breakdown voltage across the gap between two contact electrodes. Breakdown voltage is the maximum voltage which the electrode can withstand without any arc. The  $V_b$  breakdown voltage for microgap is given by

$$V_b = \frac{Bpg_d}{(C + \ln(pg_d))} \quad (4.1)$$

$$C = \ln(A / \ln(1 + 1/\gamma)) \quad (4.2)$$

For air  $A = 15 \text{ cm}^{-1}\text{Torr}^{-1}$ ,  $B = 365 \text{ Vcm}^{-1} \text{ Torr}^{-1}$  and  $\gamma = 0.01$ (Tirumala, 2010). The Figure 4.2 shows the Paschen curve for microgap at the pressure of 1 atmospheric air.

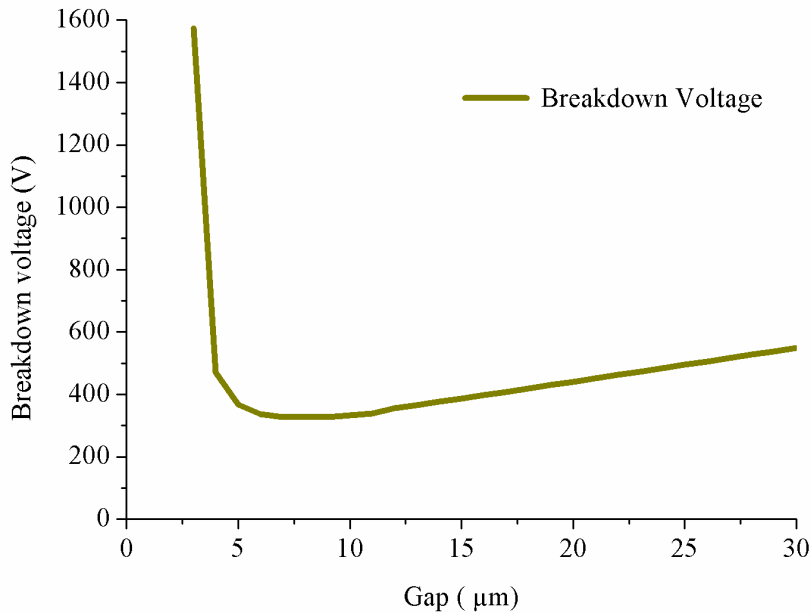


**Figure 4.2:** Paschen curve (Kuffel et al., 2000)

As the contact gap decreases from 30  $\mu\text{m}$ , the breakdown voltage decreases. However, at contact gap of 7.5 $\mu\text{m}$ , breakdown voltage reaches a minimum of 330V. As we scale down to smaller gaps below 6  $\mu\text{m}$ , the Paschen curve indicates the breakdown voltage to be very high. The Paschen curve failed to predict the behavior in gaps lower than 6 $\mu\text{m}$ .

#### 4.3.2 Breakdown arc analysis using modified Paschen curve

Modified Paschen curve presents the breakdown voltage for micrometer gap. Modified Paschen curve for various gas medium such as air, Neon, Argon are reported for various pressure (Go and Venkatraman, 2014). Strong et al., (2008) suggested that modified Paschen curve is a standard curve used to obtain the breakdown voltage. Since arc analysis is carried out for four materials such as Al, Cu, Au and Pt throughout, modified Paschen curve has to be obtained for these materials. In order to design an arcless driving electrode, the breakdown voltage of air for micrometer gaps are obtained for the metals Al, Cu, Au and Pt using numerical equations.

The voltage across the micro air gap  $g_d$  separated by electrode generates ions by electron impact, results in primary ionization. Go and Pohlman (2010) presented, Townsend's first ionization coefficient  $\alpha$  as follows

$$\alpha = Ap e^{-Bpg_d/V_b} \quad (4.3)$$

The secondary electron emission due to bombarding ions is given by Townsend's second ionization coefficient  $\gamma_i$ , which is defined as the ratio of secondary emission current  $j_{\text{sec}}$  and incident ion current  $j_{\text{ion}}$  (Storozhev and Surzhikov, 2015)

$$\gamma_i = j_{\text{sec}}/j_{\text{ion}} \quad (4.4)$$

$\gamma_i$  for the materials Al, Cu, Au and Pt are 0.035, 0.025, 0.02 and 0.017 respectively (Bell, 1991).

In microgaps, field-emitted electrons occurs due to an approaching ion causes ion-enhanced field emission results effective secondary emission coefficient  $\gamma_{\text{eff}}$  and this phenomena is absent in larger gaps.

The secondary emission current  $j_{\text{sec}}$  and enhanced field emission current  $j_{\text{fld}}$  forms the net emission current  $j_{\text{emit}}$

$$j_{\text{emit}} = j_{\text{sec}} + j_{\text{fld}} \quad (4.5)$$



The emission of an electron is enhanced by an incident ion and an approaching ion. The net effective secondary emission coefficient  $\gamma_{net}$  is given as the ratio of the current of field emitted electron current  $J_{emit}$  and incident ion current  $J_{ion}$

$$\gamma_{net} = J_{emit} / J_{ion} = J_{sec} + J_{fld} / J_{ion} = \gamma_i + \gamma_{eff} \quad (4.6)$$

The ratio of the current of field emitted electron current  $j_{fld}$  and incident ion current  $J_{ion}$  gives the effective secondary emission coefficient  $\gamma_{eff}$ . This is given by

$$\gamma_{eff} = j_{fld} / J_{ion} = K e^{-Eg_d/V_b} \quad (4.7)$$

Where constant  $K = 10^7$  and the coefficient  $E$  can be obtained in terms of apparent applied field

$$E = (6.85 \times 10^7) \phi^{3/2} / \beta \quad (4.8)$$

Where  $\phi = 4 eV$  is the work function of the cathode and  $\beta = 50$  is the geometrical enhancement factor, and hence  $E \approx 10^7$  (Boyle and Kisliuk, 1955).

The breakdown criterion is then based on the mathematical condition where the current increases to

$$\gamma_i (e^{\alpha g_d} - 1) = 1 \quad (4.9)$$

Using breakdown criterion and the solution of  $\alpha$ , the relation between breakdown voltage  $V_b$  and contact gap  $g_d$  is given by

$$(\gamma_i + K e^{-Eg_d/V_b}) \left[ e^{Apg_d e^{(-Bpg_d/V_b)}} - 1 \right] = 1 \quad (4.10)$$

The equation 4.10 is solved using Newton-Raphson method. This is a simple, iterative and powerful technique to solve the equations numerically. The Newton-Raphson equation used to solve the above equations is given in Appendix A. The MATLAB M-file program used to obtain modified Paschen curve using Newton-Raphson method is given in Appendix B. The analysis has been carried out for  $0.5\mu\text{m}$  to  $30\mu\text{m}$ . The resulting curve obtained is shown in Figure 4.3 and this is the modified Paschen curve which gives the breakdown voltage for Al, Cu, Au and Pt.

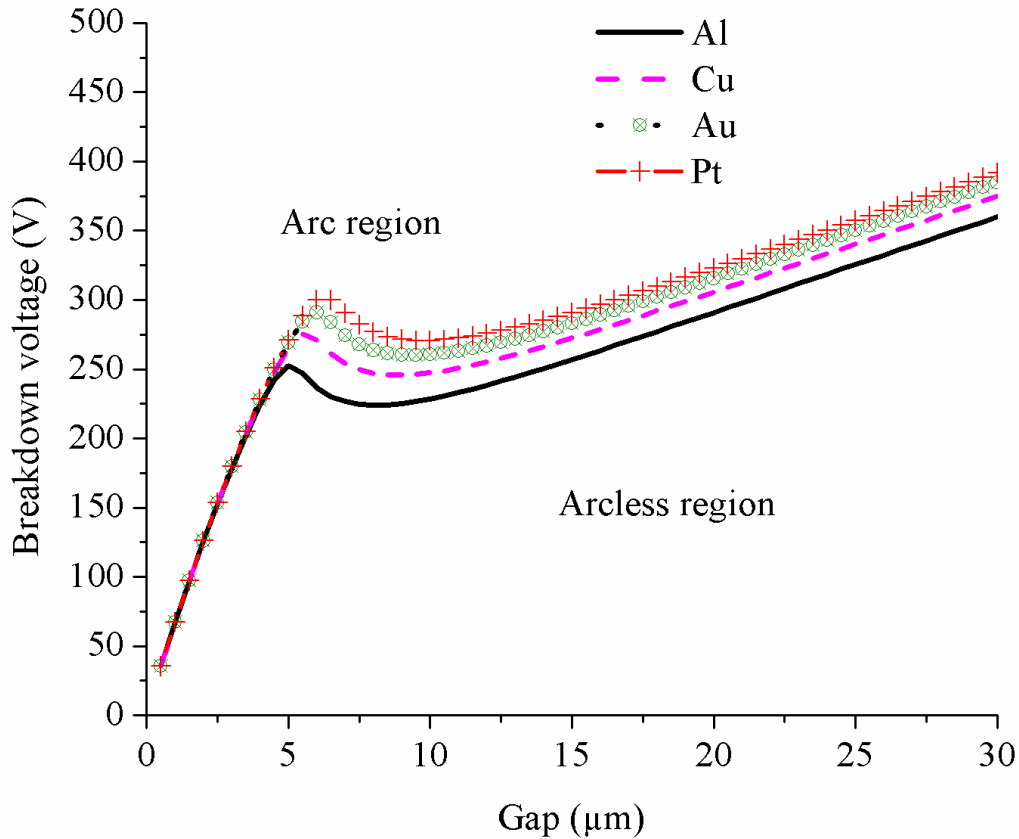


**Figure 4.3:** Modified Paschen curve for the materials Al, Cu, Au and Pt

Figure 4.3 shows that when contact gap increases from  $0.5\mu\text{m}$  to  $6\mu\text{m}$ , the breakdown voltage also gradually increases to 250V, 275V, 290 and 300 V for Al, Cu, Au and Pt respectively. When contact gap increases from  $6\mu\text{m}$  to  $30\mu\text{m}$ , breakdown voltage reduces and then again increases. Between  $7\mu\text{m}$  to  $10\mu\text{m}$  the drop in breakdown voltage occurs because transition of small gap to the large gap. Hence above  $9\mu\text{m}$ , the modified Paschen curve is similar to Paschen curve. The modified Paschen curve consists of three regions: Gaps greater than  $10\mu\text{m}$ , a plateau between  $5\mu\text{m}$  to  $10\mu\text{m}$  and a steep decline for gaps less than  $5\mu\text{m}$ . The contribution of ion-enhanced field emission  $\gamma_{eff}$  is considerable at small gaps and slowly decreases at large gaps. But in the larger gaps, the secondary emission  $\gamma_i$  is significant. Gap below  $5\mu\text{m}$  are influenced by ion enhanced field emission and is independent of material. Gaps above  $10\mu\text{m}$  are dominated by secondary electron emission which depends on material. The gap between  $5\mu\text{m}$  to  $10\mu\text{m}$  is the region which has influence of both ion enhanced field emission and secondary electron emission.

This curve gives the boundary between arc and arcless region. In electrostatically actuated micromechanical switch, the gap ranges between 1 $\mu\text{m}$  and 7 $\mu\text{m}$  (Rebeiz, 2003). For the contact gaps less than 5  $\mu\text{m}$ , the breakdown voltage is a linear function of gap.

$$V_b = S \times g_d \quad (4.11)$$

Where  $S$  is the slope of approximately 60V/ $\mu\text{m}$ . The breakdown arc analysis also can be carried out using breakdown electric field as a function of gap.

### 4.3.3 Analysis of breakdown electric field as a function of electrode gap

The breakdown electric field  $E_b$  is given as

$$E_b = V_b / g_d \quad (4.12)$$

$$(\gamma_i + K e^{-D/E_b}) \left[ e^{Apg_d e^{-Bp/E_b}} - 1 \right] = 1 \quad (4.13)$$

The curve obtained is shown in Figure 4.4, which gives, the breakdown electric field as the function of electrode gap ranges from 0.5 $\mu\text{m}$  to 30 $\mu\text{m}$ . The breakdown electric field obtained for the materials Al, Cu, Au and Pt. The electrode gap and material has sufficient influence on the breakdown electric field.

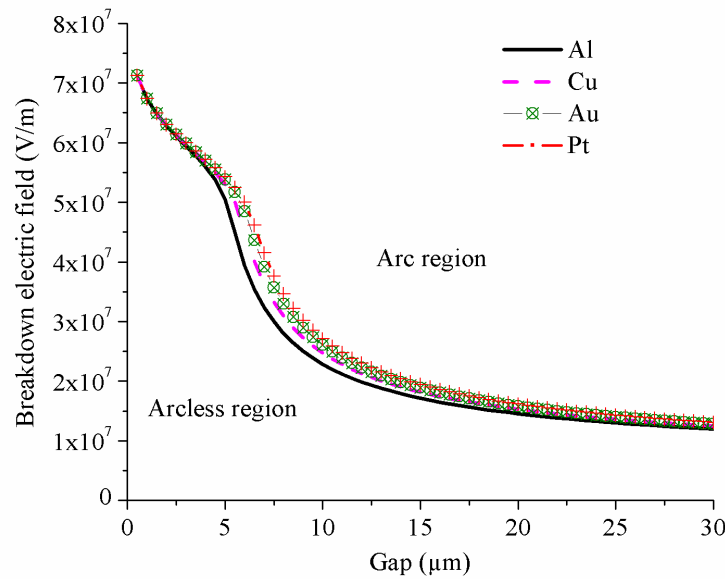


**Figure 4.4:** Breakdown electric field as a function of electrode gap

If the electric field across the contact gap is higher than breakdown electric field of air, an arc discharge begins. The breakdown electric field curve creates a boundary between arcing and arcless region. The area below the curve is arcless region and area above the

curve is arcing region. Platinum has higher breakdown electric field among the materials Al, Cu, Au and Pt. Aluminum has the least value of breakdown electric field. As gap increases from 0.5 $\mu\text{m}$  to 30 $\mu\text{m}$ , the electric field varies from  $7e^7\text{V/m}$  to  $1e^7\text{V/m}$ .

Figure 4.3 Shows that the smaller gap withstands less voltage without arc. But Figure 4.4 shows that smaller gap withstand high electric field. These curves provide the breakdown voltage and electric field as a function of gap and also provide the boundary between arc and arcless region. Now it is required to find the electric field appears across the driving electrodes and to check whether the electric field is in arcless region. The driving voltage appears across the driving electrodes produces electric field which depends on the electrode dimensions. Depends on the dimension of the driving electrode lower voltage can cause higher electric field and higher voltage can cause lower electric field. Hence it is important to analyze the voltage appearing across the driving electrode and electric field produced by the electrode. Both voltage and electric field should fall in the arcless region.

#### 4.4 Arc Analysis during OFF-State

During OFF-state, the driving electrode behaves as a parallel plate capacitor. The capacitance and electric field of the driving electrode are modeled to achieve arcless driving electrode. Also it is required to visualize the distribution of electric field.

##### 4.4.1 Mathematical Modeling

The capacitance of the driving electrode  $C_d$  during OFF-state is given as

$$C_d = \frac{k\varepsilon_0 L_d W_d}{g_d} [C_{df} + C_{dfi}] \quad (4.14)$$

$$C_{df} = 1 + \frac{g_d}{\pi L_d} + \frac{g_d}{\pi L_d} \ln \left( \frac{2\pi L_d}{g_d} \right) \quad (4.15)$$

$$C_{dfi} = \frac{g_d}{\pi L_d} \ln \left( 1 + \frac{2t_d}{g_d} + 2\sqrt{\frac{t_d}{g_d} + \frac{t_d^2}{g_d^2}} \right) \quad (4.16)$$

Where  $\varepsilon_0$  is the permittivity of air,  $k$  is the relative permittivity of air.  $k\varepsilon_0 L_d W_d / g_d$  is the normal capacitance of the parallel plate electrode,  $C_{df}$  is the fringing field due to the

finite dimensions of the driving electrodes and  $C_{dft}$  is the fringing field associated with the thickness of the driving electrode (Leus and Elata, 2004).

The amount of charge that can be placed on the plates is proportional to the voltage pushing the charge on to the positive plane. The charge on the driving electrode  $Q_d$  is given by

$$Q_d = C_d V_d \quad (4.17)$$

The electric field  $E_d$  between the driving electrodes is given by

$$E_d = \frac{Q_d}{L_d W_d \epsilon_0} \quad (4.18)$$

It is noted that the electric field appearing across the driving electrodes, depends on the size of the driving electrode and the voltage applied across the driving electrodes.

#### 4.4.2 Simulation

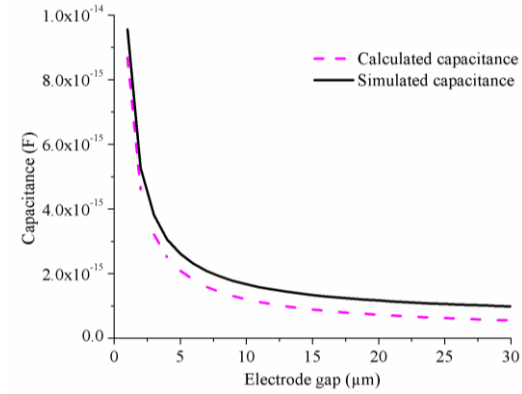
With the objective of comparing the calculated capacitance and electric field, the COMSOL Multiphysics FEM tool has been used. The FEM analysis uses Maxwell's equation to obtain the capacitance and electric field of the driving electrode. These are given in Appendix C. The surface plots obtained using COMSOL Multiphysics tool and the values are obtained from the plots.

The capacitance and electric field of the driving electrode for the gaps  $1\mu\text{m}$  to  $30\mu\text{m}$  are obtained using mathematical model and COMSOL FEM simulations. In order to obtain the electric field for various sizes of the driving electrode, the voltage across the driving electrode is kept at 1V.

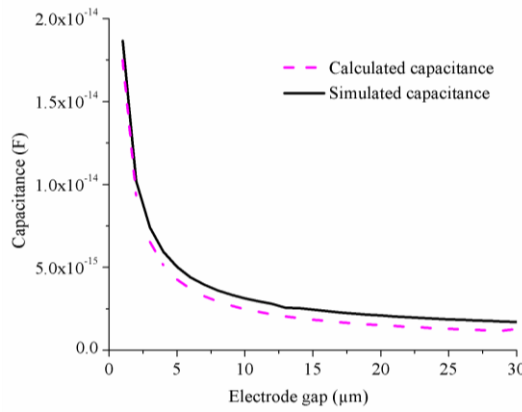
The capacitance considered for three cases considered are given in Figure 4.5. The capacitance varies between  $18.69e^{-15}\text{F}$  to  $5.488e^{-16}\text{F}$  for case 1,  $1.75e^{-14}\text{F}$  to  $1.27e^{-15}\text{F}$  for case 2, and  $5.03e^{-14}\text{F}$  to  $0.267e^{-14}\text{F}$  for case 3 as shown in Figure 4.5 (a), (b) and (c) respectively.

The maximum electric field at unit voltage (1V) for 3 cases of driving electrode are obtained using mathematical modeling and FEM simulation are given in Figure 4.6. For all 3 cases, when the electrode gap varied from  $1\mu\text{m}$  to  $30\mu\text{m}$ , the calculated electric field varies from  $1.09e^6 \text{ V/m}$  to  $0.68e^5 \text{ V/m}$  for case 1,  $1.12e^6 \text{ V/m}$  to  $0.7227e^5 \text{ V/m}$  for case 2 and  $1.05e^6 \text{ V/m}$  to  $0.559e^5 \text{ V/m}$  for case 3 are shown in Figure 4.6(a), (b) and (c)

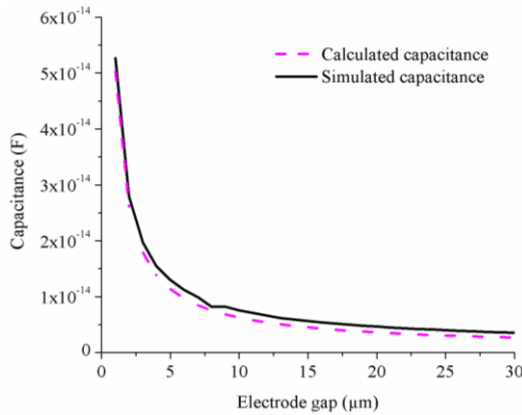
respectively. The results show that the driving electrode material does not have any influence on the capacitance and electric field across the electrodes.



(a)

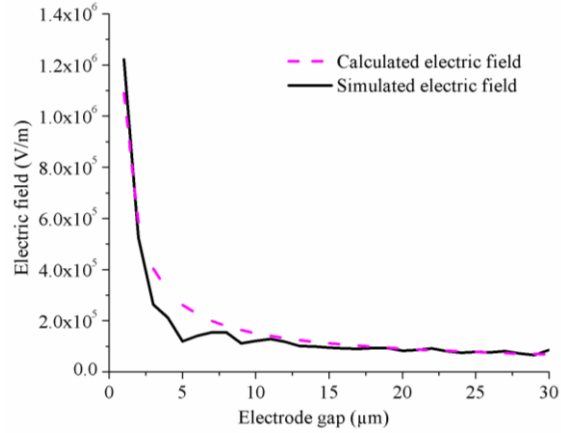


(b)

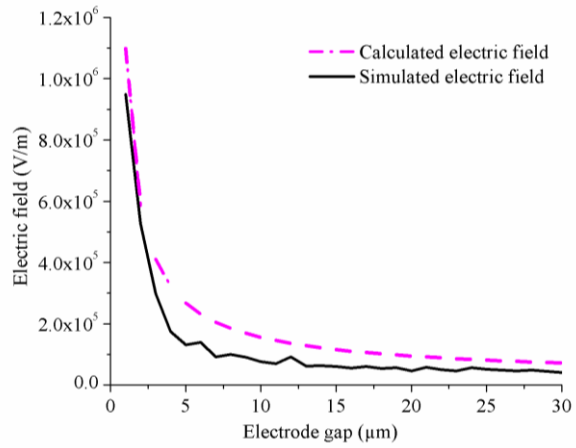


(c)

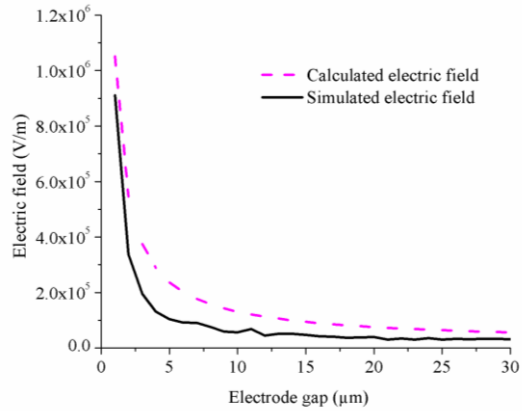
**Figure 4.5:** Capacitance of the driving electrode (a) Case 1:  $L_d = 30\mu\text{m}$ ,  $W_d = 30\mu\text{m}$ ,  $t_d = 2\mu\text{m}$ , (b) Case 2:  $L_d = 30\mu\text{m}$ ,  $W_d = 60\mu\text{m}$ ,  $t_d = 5\mu\text{m}$  (c) Case 3:  $L_d = 50\mu\text{m}$ ,  $W_d = 50\mu\text{m}$ ,  $t_d = 10\mu\text{m}$



(a)



(b)



(c)

**Figure 4.6:** Electric field across the driving electrode (a) Case 1:  $L_d = 30\mu\text{m}$ ,  $W_d = 30\mu\text{m}$ ,  $t_d = 2\mu\text{m}$ , (b) Case 2:  $L_d = 30\mu\text{m}$ ,  $W_d = 60\mu\text{m}$ ,  $t_d = 5\mu\text{m}$  (c) Case 3:  $L_d = 50\mu\text{m}$ ,  $W_d = 50\mu\text{m}$ ,  $t_d = 10\mu\text{m}$

In order to design an arcless driving electrode, it is important to visualize the electric field distribution in the 3D structure. To visualize the capacitance, voltage, and electric field distribution the surface and slice plots are obtained using FEM analysis for case three with the gap of  $8\mu\text{m}$  and are shown in Figure 4.7. The surface plot given in Figure 4.7(a) shows that the capacitance  $0.49\text{e}^{-14}\text{F}$  is equally distributed in the surface and Figure 4.7(b) shows the surface plot for the applied voltage of 1V. The slice plot shown in Figure 4.7(c) shows the distribution of applied 1V and Figure 4.7(d) shows the electric field distribution. The maximum electric field of  $1.53\text{e}^5\text{V/m}$  and the electric field are equally distributed across the gap of the driving electrode.

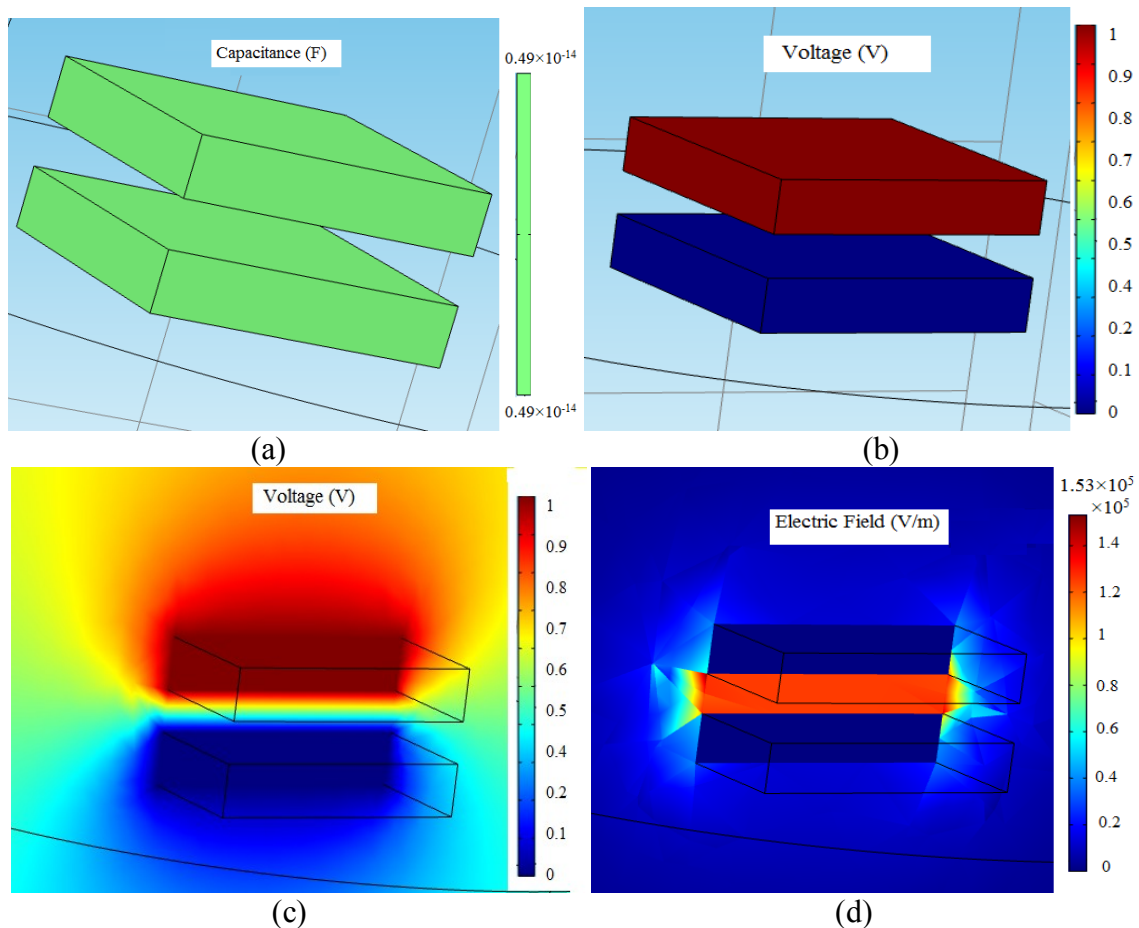


**Figure 4.7:** OFF-state FEM analysis (a) surface plot of capacitance (b) surface plot of voltage (c) slice plot of voltage (d) slice plot of electric field



#### 4.4.3 Effect of voltage

In order to analyze breakdown arc, the effect of voltage needs to be analyzed. This analysis is carried out for all the three cases stated in section 4.2 with four voltage ranges. The occurrence of arc across the driving electrode is analyzed for four voltage ranges and are given as follows:

Range A: 1 to 30 V

Range B: 1 to 150 V

Range C: 1 to 300 V

Range D: 1 to 450 V

The electric fields are obtained for all four voltage ranges by using Equation 4.16 and 4.17. The results are also obtained using simulation. The occurrence of arc in the driving electrode with various combinations of voltage and gaps are considered and analysis has been carried out. The electrode gap is varied from  $1\mu\text{m}$  to  $30\mu\text{m}$  in steps of  $1\mu\text{m}$ . At the same time the voltage across the electrode is varied from 1V to 30V in steps of 1V, 5V to 150V in steps of 5V, 10V to 300V in steps of 10V, and 15V to 450V in steps of 15V for the range A, B, C and D respectively. The variation in electrode gap and voltage for range A is shown in given in Figure 4.8

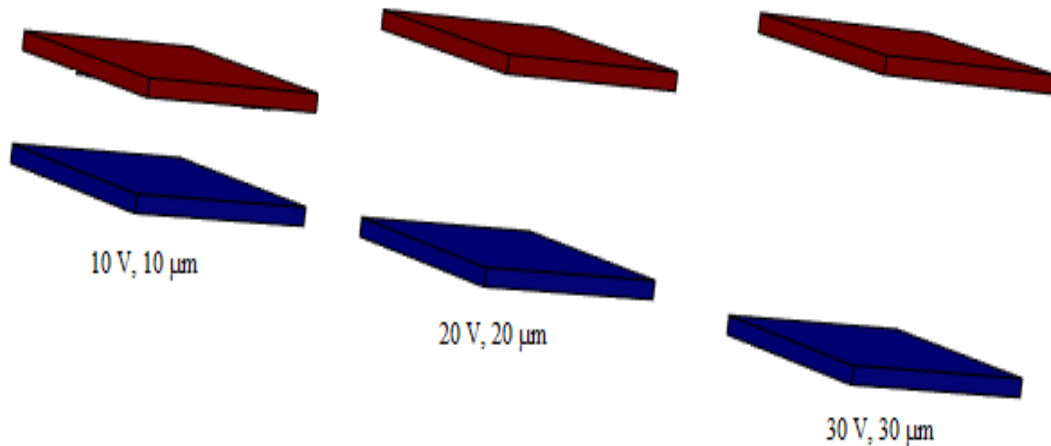
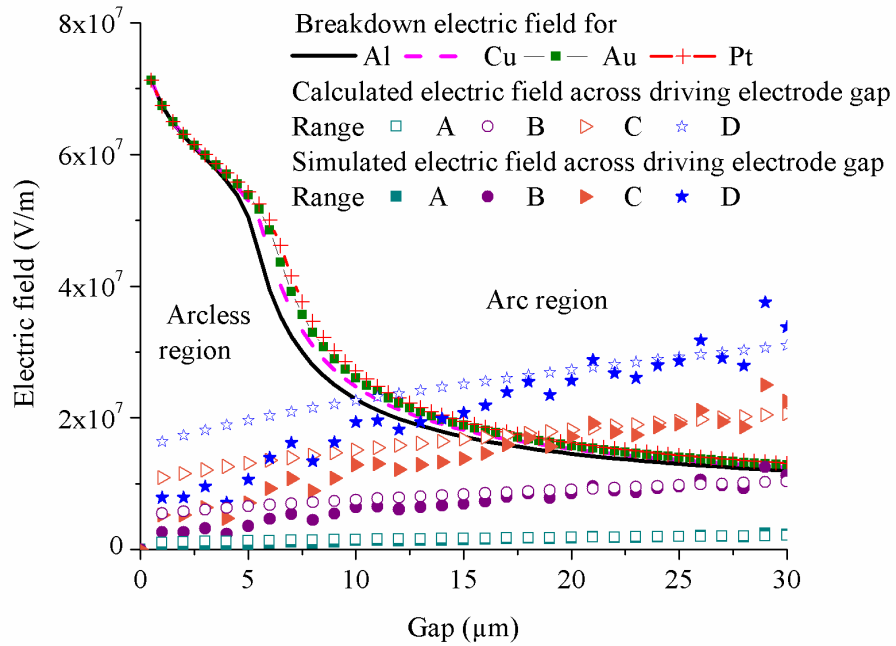
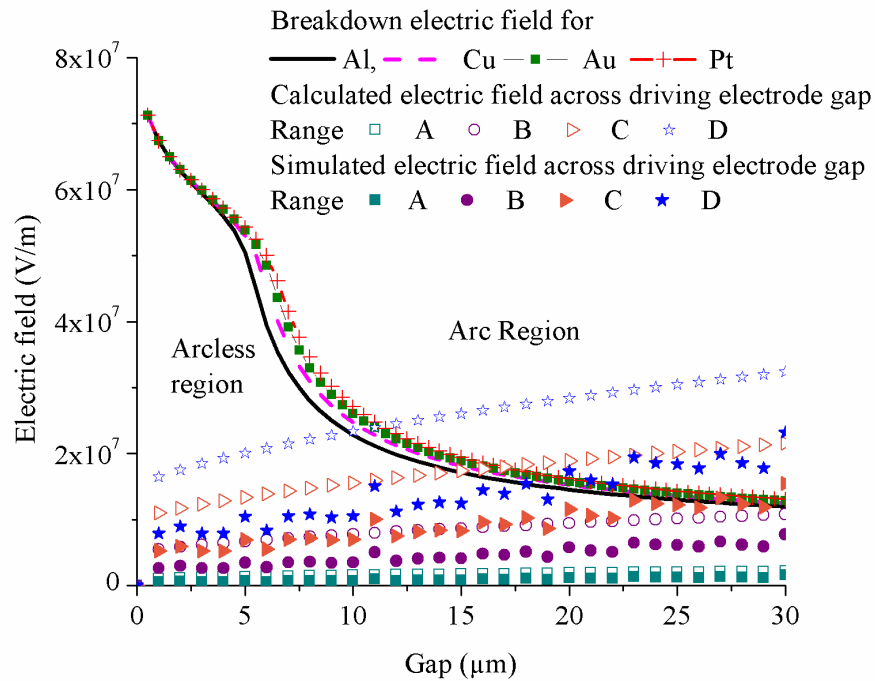


**Figure 4.8:** Variations in electrode gap and voltage for the range A

In order to analyze the arc occurrence in the driving electrode the electric fields obtained are superimposed on the breakdown electric field curve and is shown in Figure 4.9. This shows the calculated and simulated electric field across the contact gap for various voltage ranges and materials.



(a)



(b)

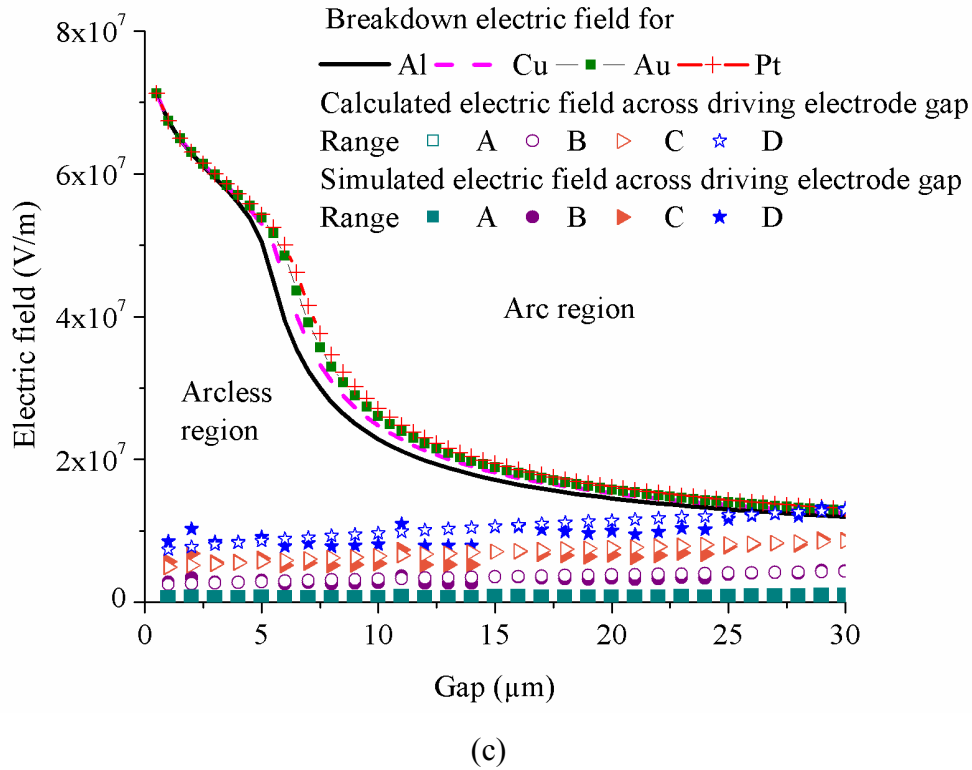


**Figure 4.9:** Arc analysis during OFF-state for (a) case 1 (b) case 2 and (c) case 3

Figure 4.9(a) shows that for case 1, the electric field for voltage range A and B are in the arcless region. For voltage range C and D, arc occurs above  $17\mu\text{m}$  and  $11\mu\text{m}$  respectively, since it is operating in the arc region. Similarly Figure 4.9(b) shows that for case 2, the electric field for voltage range A and B are in the arcless region. Arc occurs for voltage range C and D, because it is operating in the arc region. Figure 4.9(c) shows that for case 3, the electric field for voltage range A, B, C and D are in the arcless region. This contact works in the arcless region even at 450V.

It is noted that the size of the driving electrode and voltage applied across the driving electrode are responsible for arcless design of driving electrode. At particular voltage, higher the size of the driving electrode, chance of arc occurrence is less.

#### 4.5 Arc Analysis during ON-State

During ON-state, the driving electrode behaves as a non-parallel plate capacitor. During ON-state of the micromechanical switch the gap between the driving electrodes are not uniform. The structure of the non-parallel plate driving electrode is shown in Figure

4.1(b). The gap across one edge is  $g_{d1}$  and the other edge is  $g_{d2}$ . The capacitance and electric field of the driving electrode are simulated to achieve arcless driving electrode. In order to analyze the occurrence of arc in the driving electrode, case a, b and c with various gap between driving electrode are considered and are given by

Case a: case 1 with  $g_{d1} = 2 \mu\text{m}$  and  $g_{d2} = 10\mu\text{m}$

Case b: case 2 with  $g_{d1} = 0.5\mu\text{m}$  and  $g_{d2} = 12\mu\text{m}$

Case c: case 3 with  $g_{d1} = 3\mu\text{m}$  and  $g_{d2} = 13\mu\text{m}$

The slice plots are obtained using FEM analysis for case c are shown in Figure 4.10. The surface plot from Figure 4.10(a) shows that the capacitance of  $5.43e^{-15}\text{F}$  is equally distributed in the surface and Figure 4.10(b) shows the voltage distribution when 1V is applied between the electrodes. The slice plot shown in Figure 4.10(c) shows the voltage distribution of applied 1V and Figure 4.10(d) shows the electric field distribution. These visuals give a clear picture of the distribution of voltage and electric field.

The maximum electric field of  $2.89e^5\text{V/m}$  and the electric field are not equally distributed across the gap of the driving electrode. The maximum electric field appears across the smaller gap ( $g_{d1}$ ) and less in the larger gap ( $g_{d2}$ ). So the breakdown arc analysis for the smaller gap is sufficient. If arc doesn't occur in the smaller gap, arc would not occur in the larger gap due to the electric field. The capacitance and maximum electric field per unit voltage are obtained for the case a, b and c are given in Table 4.1. It is noted that in case 2, smaller gap results in high capacitance and less isolation. It is also observed that more electric field appears across the smaller gap.

**Table 4.1:** Capacitance and electric field during ON-state

Case	Capacitance (F)	Electric field (V/m)
1	$2.29e^{-15}$	$2.31e^5$
2	$6.45e^{-15}$	$1.13e^6$
3	$5.43e^{-15}$	$2.89e^5$

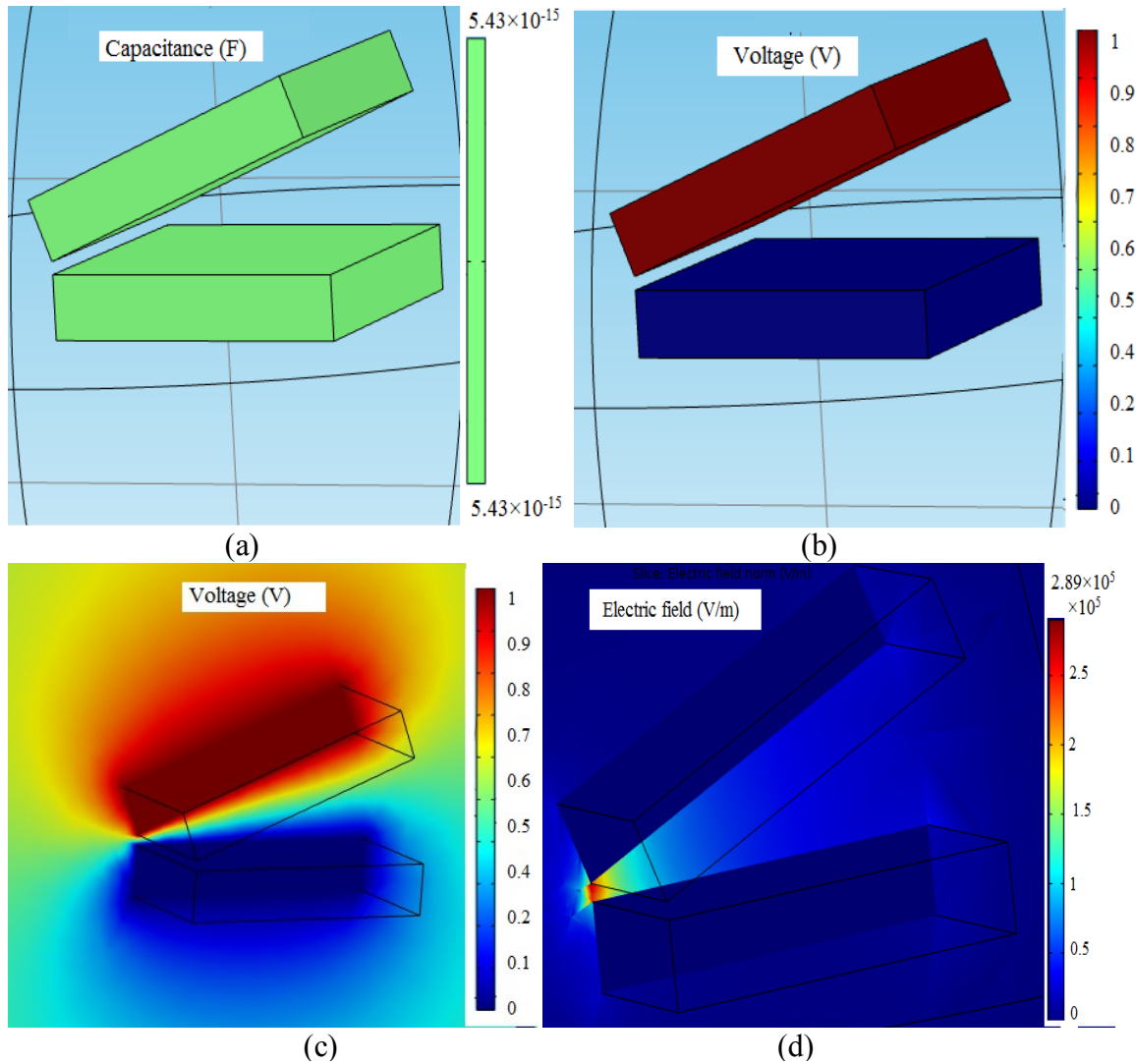


**Figure 4.10:** ON-state FEM analysis results (a) surface plot of capacitance (b) surface plot of voltage (c) surface plot of voltage (c) surface plot of electric field

## 4.6 Discussion on Breakdown Arc

This chapter considered the driving electrode during ON-state and OFF-state. Modified Paschen curve has been plotted for Al, Cu, Au and Pt. The boundary between arc and arcless region are identified. Analysis of electric field appears across the driving electrode is carried out for ON-state and OFF-state. Also the breakdown electric field has been plotted for the materials and detailed study for design of arcless driving electrode has been carried out. In order to analyze the occurrence of arc due to applied voltage and the electric field produced, detailed analysis is presented in this section.

During OFF-state, for the case three with the gap of  $8\mu\text{m}$  is considered. Voltage of 50V, 250V and 400V are applied across the driving electrode. These driving voltages are superimposed on modified Paschen curve and the results are given in Figure 4.11. It shows that, 50V won't cause arc since it is in arcless region. Arc occurs at 400V, because it is in the arc region for all the materials. For Au and Pt driving electrodes, arc won't occur at 250V because it falls in the arcless region. Arc occurs at 400V for Al and Cu driving electrode.

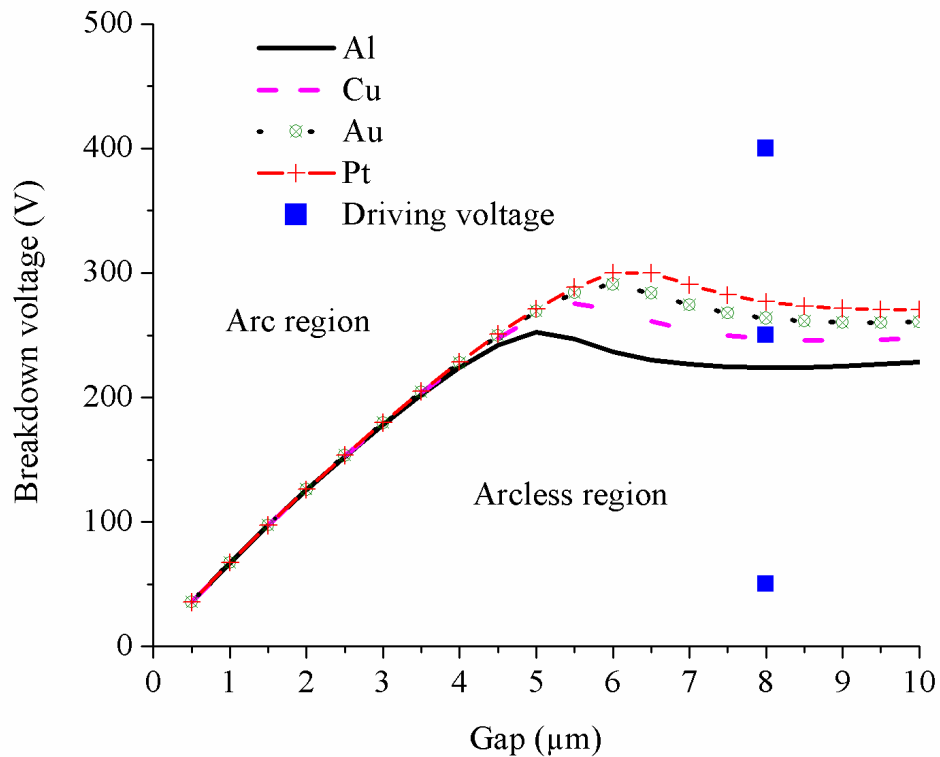


**Figure 4.11:** Arc analysis during OFF-state using modified Paschen curve for 50V, 250V and 400V at  $8\mu\text{m}$

At 50V, 250V and 400V, the electric field is obtained as  $0.38 \times 10^7 \text{V/m}$ ,  $1.9 \times 10^7 \text{V/m}$  and  $3.09 \times 10^7 \text{V/m}$  respectively. These are superimposed with breakdown electric field curve as shown in Figure 4.12. This shows that, the electric field produced by 50V and 250V may not lead to arc for all the materials. The electric field produced by 400V may not produce arc for Au and Pt, but arc may produce arc for Al and Cu.

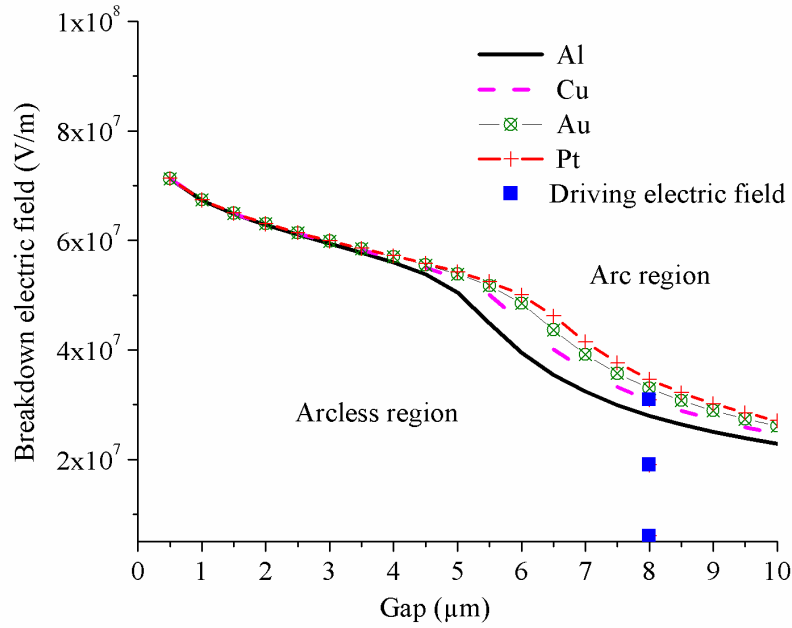


**Figure 4.12:** Arc analysis during OFF-state using breakdown electric field for 50V, 250V and 400V at 8 $\mu$ m

**Table 4.2:** Occurrence of arc during OFF-state

Voltage	Electric field (V/m)	Material	Arc due to voltage	Arc due to electric field
50V	$0.38 \times 10^7$	Al	NO	NO
		Cu	NO	NO
		Au	NO	NO
		Pt	NO	NO
250V	$1.9 \times 10^7$	Al	YES	NO
		Cu	YES	NO
		Au	NO	NO
		Pt	NO	NO
400V	$3.09 \times 10^7$	Al	YES	YES
		Cu	YES	YES
		Au	YES	NO
		Pt	YES	NO

YES means arc occurs and NO means arc does not occurs

The arc occurrence due to voltage and electric field are summarized in Table 4.2. From this it is clear that the driving voltage less than the breakdown voltage can also cause arc due electric field and vice versa. Hence it is preferred to choose the electrode which won't cause arc due to voltage and electric field.

Similar analysis has been carried out during ON-state for case a, b and c. The voltage of 50V, 250V and 400V are given across the driving electrode. These voltages are superimposed with modified Paschen curve as given in Figure 4.13 and the arc occurrence is discussed. Also the electric field is obtained for these voltages and the results are superimposed with the breakdown electric field as shown in Figure 4.14. Figure 4.13 and 4.14 shows that, below 4 $\mu\text{m}$ , the material does not have influence on the breakdown voltage and breakdown electric field. The arc occurrence due to both breakdown voltage and breakdown electric field is discussed in Table 4.3.

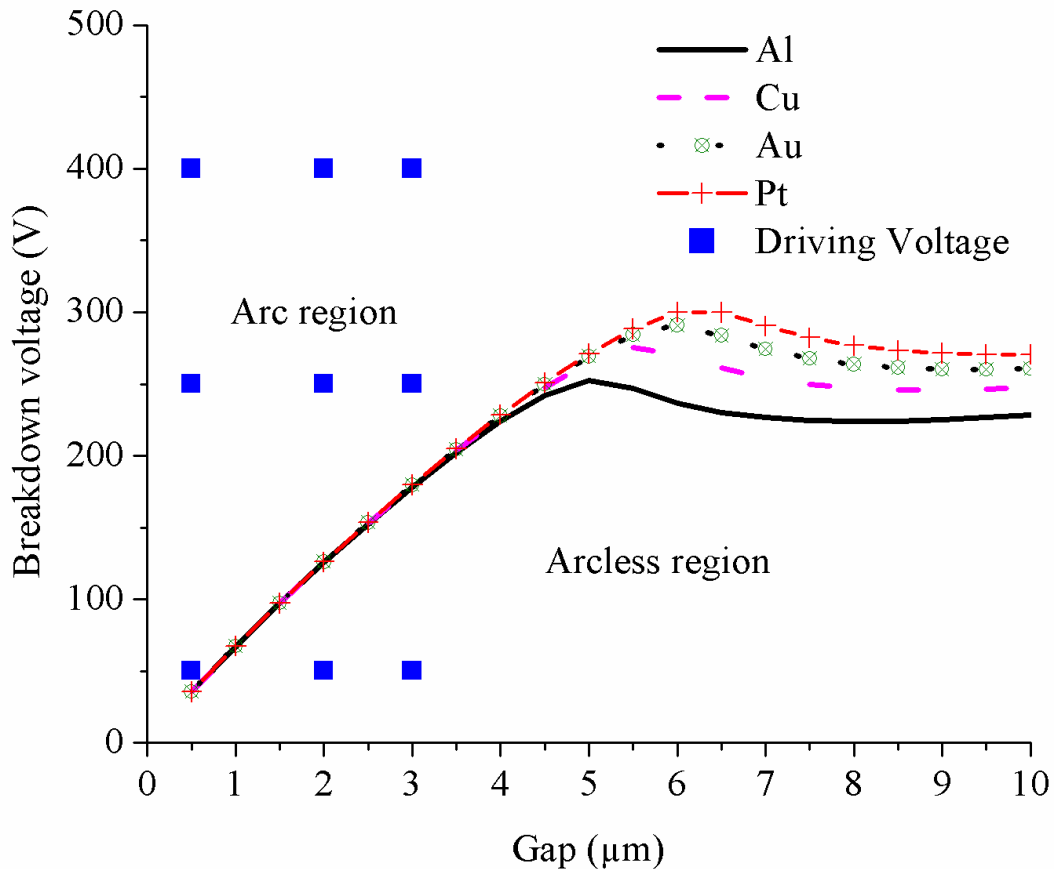


**Figure 4.13:** Arc analysis for 50V, 250V and 400V during ON-state



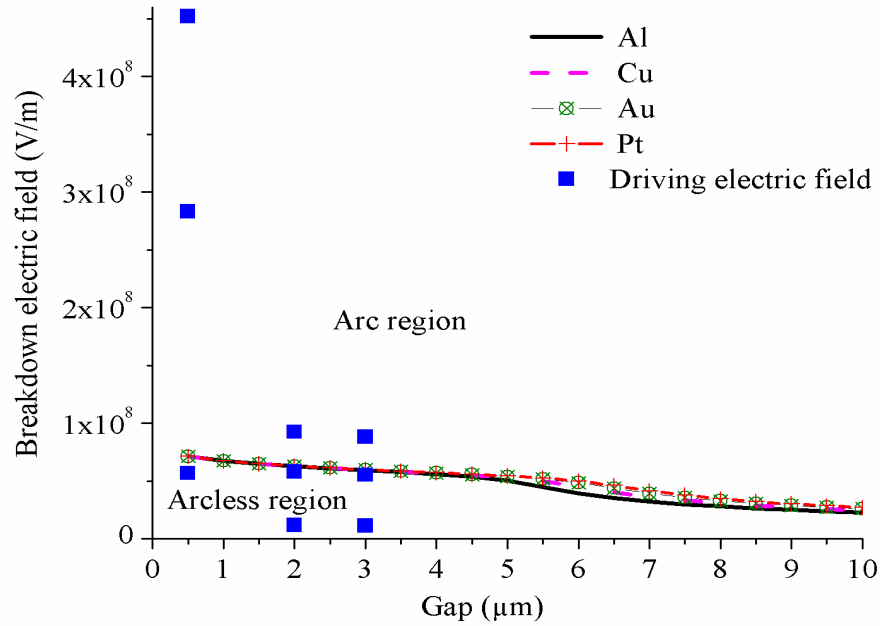


**Figure 4.15:** Arc analysis during ON-state for 50V, 250V and 400V using breakdown electric field

**Table 4.3:** Electric field and arc occurrence during ON-state

Case	Voltage	Electric field (V/m)	Arc occurrence due to voltage	Arc occurrence due to electric field
Case a	50V	$11.55 \times 10^6$	NO	NO
	250	$57.75 \times 10^6$	YES	NO
	400V	$92.4 \times 10^6$	YES	YES
Case b	50V	$56.6 \times 10^6$	YES	NO
	250	$283 \times 10^6$	YES	YES
	400V	$452 \times 10^6$	YES	YES
Case c	50V	$11 \times 10^6$	NO	NO
	250	$55 \times 10^6$	YES	NO
	400V	$88 \times 10^6$	YES	YES

This results shows that when the driving voltage is less than the breakdown voltage, the electric field may cause arc. Also when the driving voltage is more than the breakdown

voltage, the electric field may not cause arc. Hence while designing an arcless driving electrode both voltage and electric field has to be taken in to consideration. The size of the driving electrode and voltage combination has to be carefully selected while designing the micromechanical switch for arcless switching.

## 4.7 Conclusion

The conclusions of this chapter are as flows:

- Modified Paschen curve and breakdown electric field curve has been obtained for Al, Cu, Au and Pt at room temperature and atmospheric pressure. The boundary between the arc region and arcless region has been presented. At the gap of  $6\mu\text{m}$ , the breakdown voltages are obtained as 250V, 275V, 290V and 300V for the materials Al, Cu, Au and Pt respectively. It is found that the breakdown voltage is  $60\text{V}/\mu\text{m}$  for the gap less than  $6\mu\text{m}$ .
- The breakdown electric field is obtained for  $1\mu\text{m}$  to  $30\mu\text{m}$  gap and the electric field varies from  $7e^7$  V/m to  $1e^7$  V/m. It is found that both voltage and electric field needs to be analyzed to design arcless driving electrode. It is found that the breakdown voltage and breakdown electric field are high for Pt and low for Al.
- The structure of the driving electrode has been presented for ON-state and OFF-state. Three cases are presented with different electrode dimensions and four voltage levels. It is found that higher the size of the driving electrode, the chances of arc occurrence is less.
- The ON-state breakdown arc has been analyzed for various size and gap of the driving electrode. It is found that smaller gap may leads to arc. If the smaller gap point on the driving electrode does not produce arc, the larger gap point may not produces arc. The occurrence of arc has been discussed for 50V, 200V and 400V.
- Detailed investigation has been carried out during OFF-state and ON-state to analyze the occurrence of arc due to applied voltage and electric field produced. It is found that even if the contact voltage is less than breakdown voltage, the electric field can cause breakdown arc.

# CHAPTER 5

## MODELING AND ANALYSIS OF ARCLESS MICROELECTRICAL CONTACT

### 5.1 Introduction

Commercialization of micromechanical switches are challenging because of life time and reliability issues. Reliability of electromechanical switch depends on many parameters such as structure, electrical, mechanical, material, operating conditions, environment and fabrication process. Among these, electrical and mechanical parameters plays important role in the reliability. Micromechanical switches use microelectrical contact which allows and interrupt electric current. Reliable operation of the micromechanical switches can be achieved if the microelectrical contact is reliable.

The reliability of microelectrical contact is mainly affected due to two reasons. One is contact welding and the other is contact arc. During ON-state, electric current flows through the contact which depends on the resistance of the microelectrical contact. The current and resistance cause voltage-drop and power dissipation. This leads to increase in temperature of the microelectrical contact. If the temperature reaches the melting temperature of the contact material, leads to contact welding. The contact will be always in the ON-state and failed to move to the OFF-state. This is called contact welding or struck close state (Slade, 2014). In electrostatically actuated micromechanical switches arc occurrence is very significant in both driving electrode and microelectrical contact. The design of arcless driving electrode has been discussed in chapter 4. In microelectrical contacts arc can occur during the following states (Balachandra and Nagabhushana, 1993):

1. Switching state: The vaporization of cathode material causes pre-breakdown arc.
2. OFF-state: The voltage and electric field across anode and cathode ionize the medium present in the contact gap can initiate breakdown arc.

Contact resistance is an important factor for the reliability and life of the microelectrical contact (Aronstein and Hare, 2005). The temperature distribution is a very essential factor in the occurrence of arc (Li et al., 2011; Wang et al., 2014). The current carrying

capability of microelectrical contact and arc are limited by temperature (Kim et al., 2002). So it is very important to predict the temperature, while designing the micro electrical contact for power switching applications (Li Hongtao et al., 2013; Hwang et al., 2013).

In this chapter, analysis of electrothermal characteristics of 3D microelectrical contact for arcless DC switching has been carried out. Structure of 3D microelectrical contact is presented. Also ON-state parameters such as radius of contact spot, contact resistance, temperature and current carrying capability for smooth and rough surface are analyzed. The steady state and transient temperature of microelectrical contact are analyzed to achieve arcless switching. The power rating of the contact is also discussed. The OFF-state capacitance and electric field are discussed to design arcless contact. Voltage, current and power characteristics of microelectrical contacts are observed to verify the occurrence of pre-breakdown and breakdown arc.

## 5.2 Structure of Microelectrical Contact

The schematic representation of the 3D microelectrical contact geometry suitable for micromechanical switch is shown in Figure 5.1. The microelectrical contact has two fixed electrodes and one moving electrode. The fixed contact connected to positive and negative of the DC source is known as anode and cathode respectively. The moving contact is a floating (overlapping) contact. The floating contact is neither connected to positive nor to negative of DC source. When the floating contact moves down and come in physical contact with fixed contact, the switch become ON-state. This creates a continuous current conduction path between electrodes.

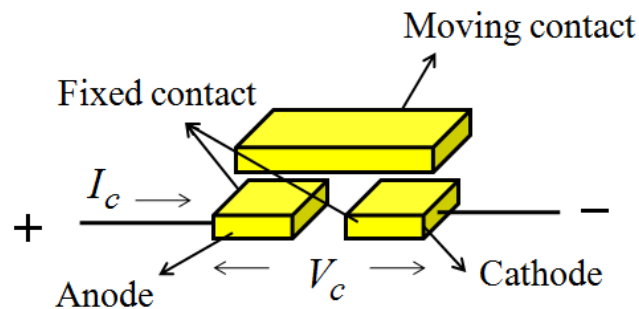


**Figure 5.1:** Structure of 3D microelectrical contact

For the design of arcless microelectrical contact, the electrothermal properties are analyzed for the following states of the switch.

1. ON-state
2. Switching state
3. OFF-state

In the ON-state, the floating contact is in touch with the fixed contact. The contact resistance appears at the microelectrical contact. The contact resistance and temperature has high influence on the reliability and life of the electrical contact. Temperature is a very important parameter in the design of ON-state microelectrical contact. The current carrying capability and reliability also depends on temperature distribution. If the temperature of the contact increases above the melting temperature of the contact material, electrodes get welded with each other and it get damaged. For designing reliable contact, it is very important to keep the temperature below the softening temperature of the contact material.

As the floating electrode of the microelectrical contact moving upwards, the current flowing through the microelectrical contact decreases. At the same time the voltage appearing across the microelectrical contact increases. Hence power appears across the contact. This phenomenon has been observed in Figure 3.3 of chapter 3. As power increases, temperature of the microelectrical contact also increases and reaches the melting temperature of the contact material. If the contact spot melts, a molten metal bridge forms between the electrodes. When the microelectrical contact reaches its evaporation temperature of the material, the molten metal bridge would evaporate, release electrons and produces arc (slade, 2004; Timron, 2005). The conventional model of breaking contact process is softening, melting, metal bridge formation, boiling, vaporization, arc ignition and isolation. In this work, the conventional breaking contact model is considered for various stages and is shown in Figure 5.2. If the temperature of the contact spot is limited below the evaporation temperature, there would not be any arc. If the temperature of the microelectrical contact is below melting temperature, molten metal bridge would not form.

The microelectrical contact needs some time to reach melting and boiling temperature. The corresponding time is called heating time (time lag). So arc can be avoided by faster switching of the contact.

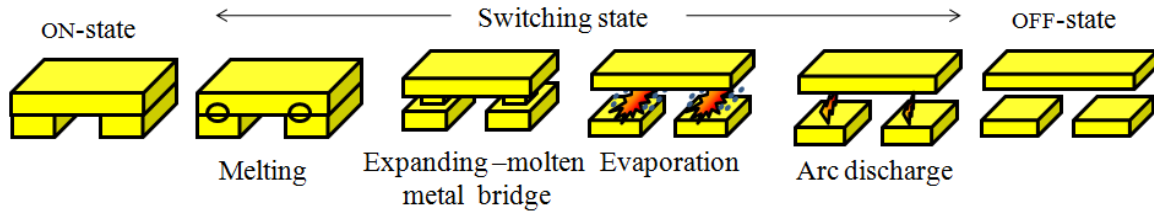


**Figure 5.2:** Various states of the microelectrical contact

During OFF-state, the floating contact won't touch the fixed contact. Hence capacitance appears across these contacts. The physical separation of electrodes results in high isolation and zero leakage current. But the voltage appears across the fixed electrical contact creates electric field across the air gap which can cause a breakdown arc. When the contact opens to interrupt the current, voltage and electric field between the contacts gradually increases. During such an event, when the voltage across the electrodes reaches the breakdown voltage or electric field between the contacts reaches the breakdown electric field of the corresponding gap, ionization of air occurs and an arc ignites.

### 5.3 ON-State

The current carrying capability and power withstanding capability are depends on the contact resistance, force, temperature and material of the microelectrical contact.

#### 5.3.1 Contact resistance

##### *Smooth surface*

The 3D structure of a microelectrical contact in the ON-state and its equivalent circuit model with current flow directions are shown in Figure 5.3(a) and (b). Anode, cathode and moving contact are made of the similar conducting material. The contact resistance is initially calculated based on the following assumptions. The structures of electrodes are ideal. The surface of electrode is perfect and smooth. The surfaces are mated perfectly.

The contact resistance  $R_{cs}$  of the microelectrical contact is given by

$$R_1 = \rho_c t_c / (L_{Fc} \times W_c) \quad (5.1)$$

$$R_2 = \rho_c t_c / [(L_{Mc} - 2L_{Fc}) \times W_c] \quad (5.2)$$

$$R_{cs} = (R_1 / 2) + R_2 + (R_1 / 2) \quad (5.3)$$

Where  $L_{Fc}$  is the length of the fixed contact,  $L_{Mc}$  is the length of moving contact,  $W_c$  is the width of the contact,  $t_c$  is the thickness of the contact and  $g_c$  is the gap between the fixed contact and  $\rho_c$  is the electrical resistivity of the contact material.

The dimensions of the microelectrical contact used in this study are: fixed contact  $L_{Fc} = 15\mu\text{m}$ ,  $W_c = 30\mu\text{m}$ ,  $t_c = 5\mu\text{m}$  each and floating electrode  $L_{Mc} = 35\mu\text{m}$ ,  $W_c = 30\mu\text{m}$ ,  $t_c = 5\mu\text{m}$ . Gap between fixed contact  $g_c$  is  $5\mu\text{m}$  and the electrodes are considered to be homogenous. The analysis has been carried out for the materials Al, Cu, Au and Pt.

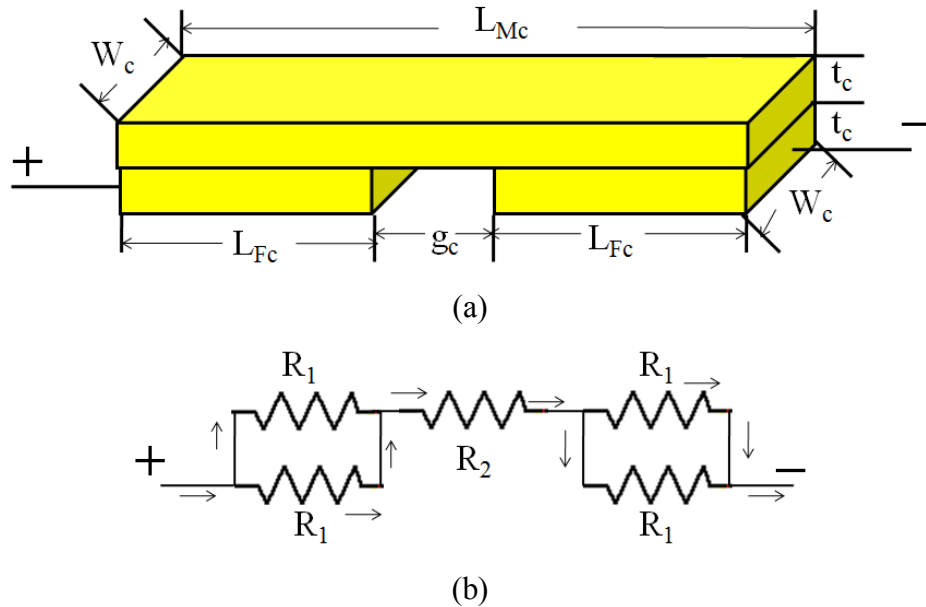


**Figure 5.3:** (a) ON-state microelectrical contact with smooth surface (b) Equivalent circuit model

The contact resistance of the microelectrical contact for the materials Al, Cu, Au and Pt are calculated using Equation 5.3. The calculation and simulation results are given in Table 5.1.

### ***Rough surface***

The surfaces of the microelectrical contact are generally very rough. It has peaks and troughs. During ON-state, contact occurs between the discrete spots of the microelectrical contact. For simplicity, it can be assumed that the contact spot is circular (Slade, 2014). The microelectrical contact with rough surface can be described with two contact spots as shown in Figure 5.4.

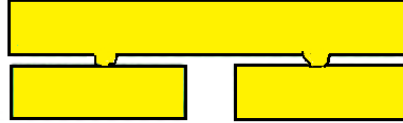


**Figure 5.4:** Microelectrical contact with rough surface

The ON-state contact resistance of the considered microelectrical contact is given by

$$R_{cr} = \frac{\rho_c}{2a_c} + \frac{\rho_c}{2a_c} = \frac{\rho_c}{a_c} \quad (5.4)$$

Where  $a_c$  is the radius of the contact spot. In microelectrical contacts the contact spot radius varies between  $0.01\mu\text{m}$  to  $10\mu\text{m}$  (Slade, 2014). Contact resistance has been obtained using Equation 5.4 and FEM simulation for the microelectrical contact with rough surface of  $0.2\mu\text{m}$  contact spot considered in the study are given in Table 5.1. The surface plot shown in Figure 5.5 shows the resistance of Al microelectrical contact with smooth and rough surface.

**Table 5.1:** ON-state resistance of the microelectrical contact

Material	ON-state contact resistance ( $\Omega$ )			
	Smooth Surface		Rough Surface	
	Calculated	Simulated	Calculated	Simulated
Al	3.58e-3	4.1e-3	1.4e-1	1.3e-1
Cu	2.24e-3	2.62e-3	0.8e-1	0.9e-1
Au	3.25e-3	3.47e-3	1.2e-1	1e-1
Pt	14.13e-3	16e-3	5.2e-1	5e-1



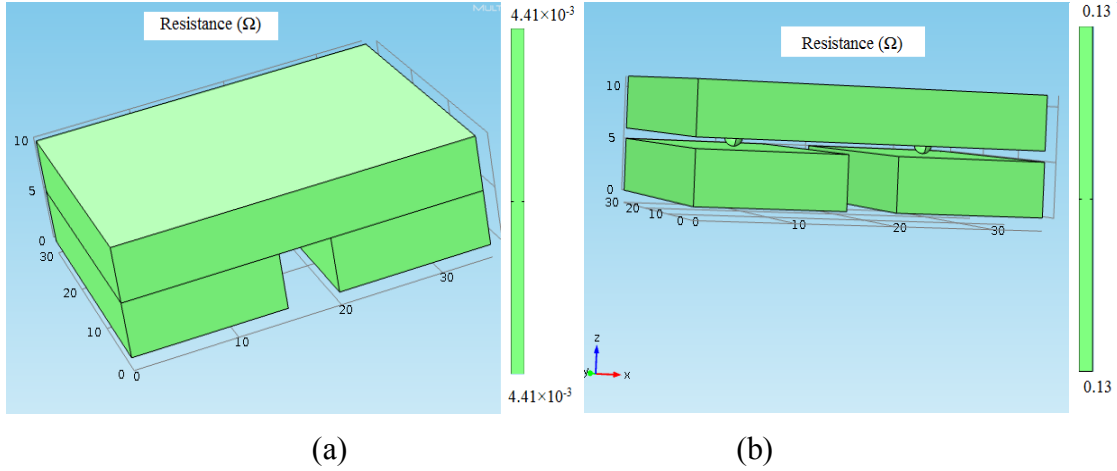


**Figure 5.5:** Surface plot for resistance of Al contact (a) smooth surface (b) rough surface

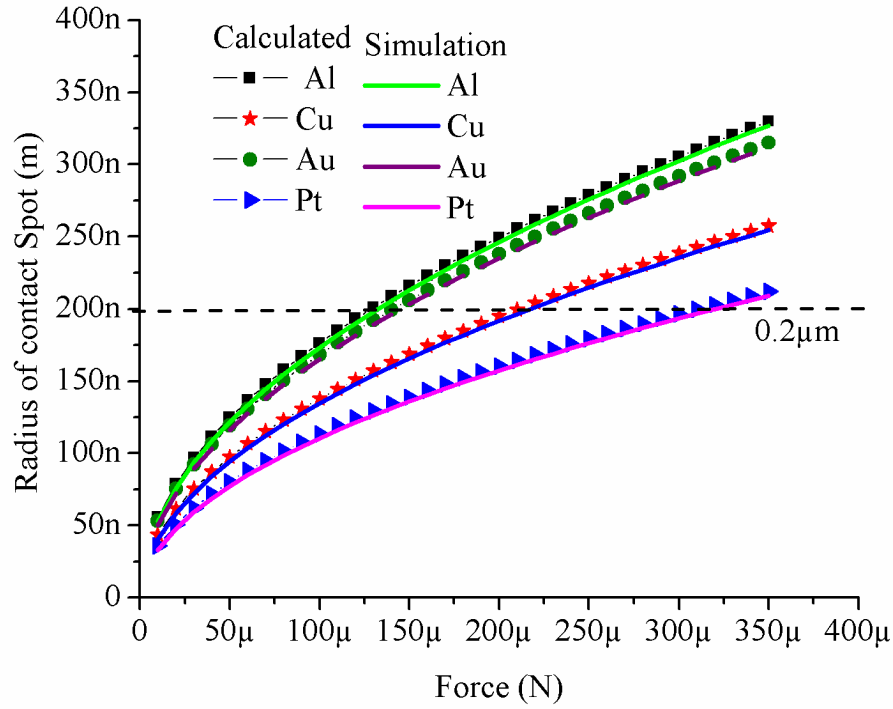
### 5.3.2 Effect of force on contact resistance

The radius of the contact spot is a function of the force acting on the microelectrical contact. The radius of the contact spot  $a_c$  is calculated using the following equations

$$a_c = \sqrt{8F_c R_{cr} / 3.14 H g_{cl}} \quad (5.5)$$

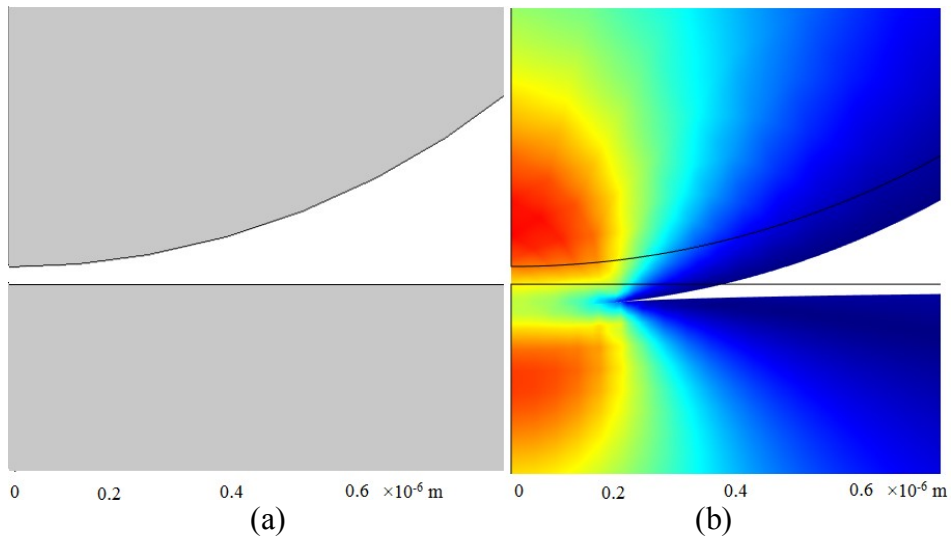
$$H = 2E_c^2 / ((2E_c \times (1 - p_c^2))) \quad (5.6)$$

Where  $F_c$  is the force acting on the moving contact,  $g_{cl}$  is the gap between fixed and moving contacts just before closing,  $R_{cr}$  is the radius of the contact,  $E_c$  is the young's modulus as a function of temperature and  $p_c$  is the poisson's ratio of the contact material (Pennec et al., 2007). The contact force of the micromechanical switches varies from  $80\mu\text{N}$  to  $300\mu\text{N}$  (Rebeiz et al., 2013). The analysis has been carried out between  $10\mu\text{N}$  and  $310\mu\text{N}$ . The FEM simulation uses the linear elasticity equations to obtain the radius of the contact spot as a function of force which is given in Appendix D. The simulation results are compared with the calculation and are shown in Figure 5.6. Microelectrical contacts reaches  $0.2\mu\text{m}$  radius of contact spot, approximately when the force is  $130\mu\text{N}$ ,  $210\mu\text{N}$ ,  $150\mu\text{N}$  and  $310\mu\text{N}$  for Al, Cu, Au and Pt respectively.



**Figure 5.6:** Radius of contact spot as a function of force

The surface plots obtained for Al from FEM simulation are shown in Figure 5.7. The contact before application of force is shown in Figure 5.7(a) and Figure 5.7(b) shows the contact after application of force. This shows the radius of contact spot  $0.2\mu\text{m}$  with applied force of  $130\mu\text{N}$  along with structure deformation and Figure 5.7(c) and (d) shows the 2D and 3D surface plots.



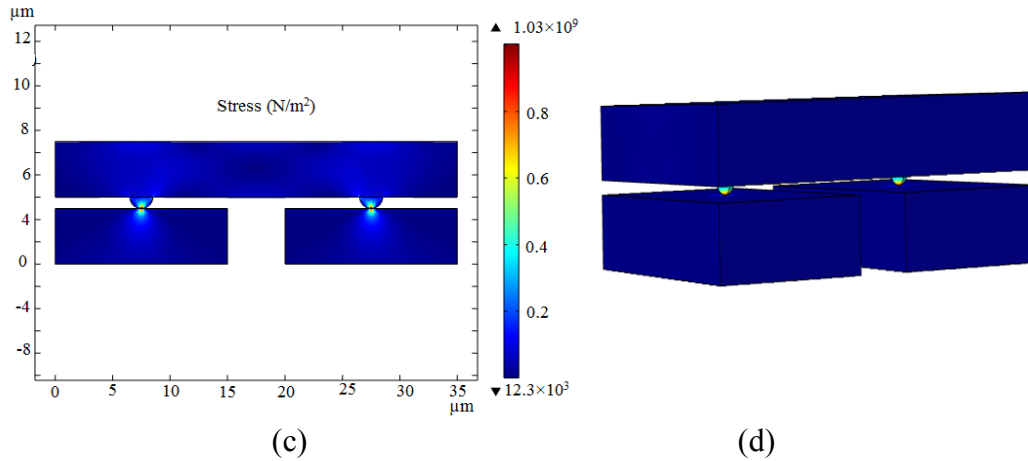


**Figure 5.7:** FEM surface plot for Al microelectrical contact (a) at  $F = 0 \mu\text{N}$  (b) structure deformation at  $F = 130 \mu\text{N}$  (c) 2D surface plot (d) 3D surface plot

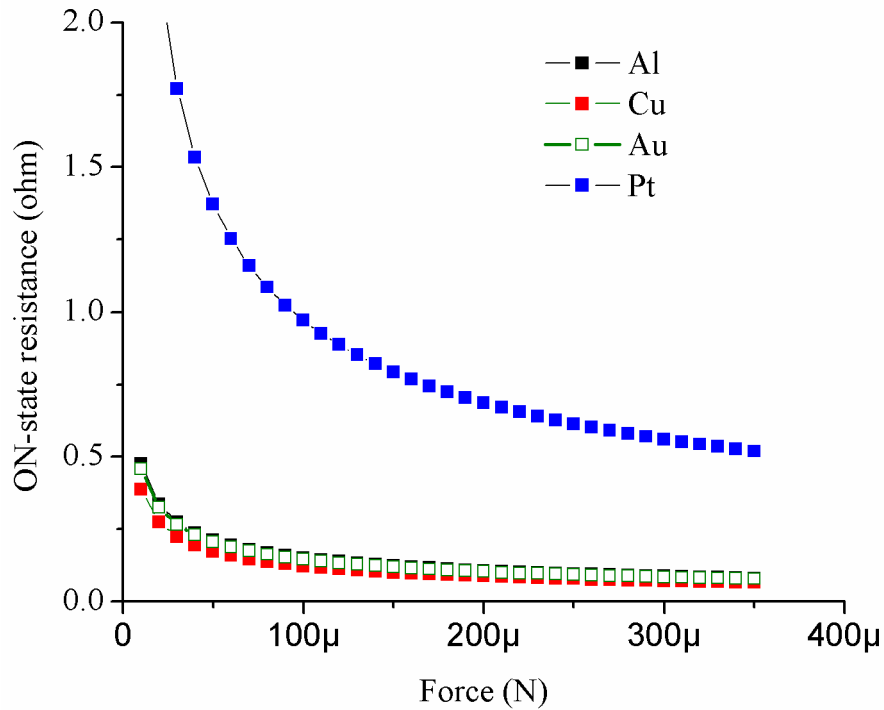


**Figure 5.8:** Force and contact resistance relationship

The ON-state resistance calculated using Equations 5.4 and 5.5 for various forces is shown in Figure 5.8. When the force increases from  $0\mu\text{N}$  to  $400\mu\text{N}$ , the area of contact spot increases hence the ON-state resistance decreases.

### 5.3.3 Effect of temperature on contact resistance

FEM analysis has been carried out for Al, Cu, Au and Pt to analyze the effect of temperature on contact resistance. In this analysis, the force and resistivity of the contact are kept constant. When temperature increases, young's modulus of the material changes and the contact area increases, hence the resistance decreases. For Al, at  $130\mu\text{N}$  force and resistivity of  $2.65\text{e}^{-8}\Omega\text{m}$ , FEM Simulation has been carried out for various temperatures. The temperature-resistance and temperature-radius of contact spot relationships are obtained. Similarly for Cu, Au and Pt FEM analysis has been carried out with the applied force of  $210\mu\text{N}$ ,  $150\mu\text{N}$  and  $310\mu\text{N}$  respectively. The resistivity of Cu, Au and Pt are kept as  $1.678\text{e}^{-8}\Omega\text{m}$ ,  $2.214\text{e}^{-8}\Omega\text{m}$  and  $10.5\text{e}^{-8}\Omega\text{m}$  respectively.

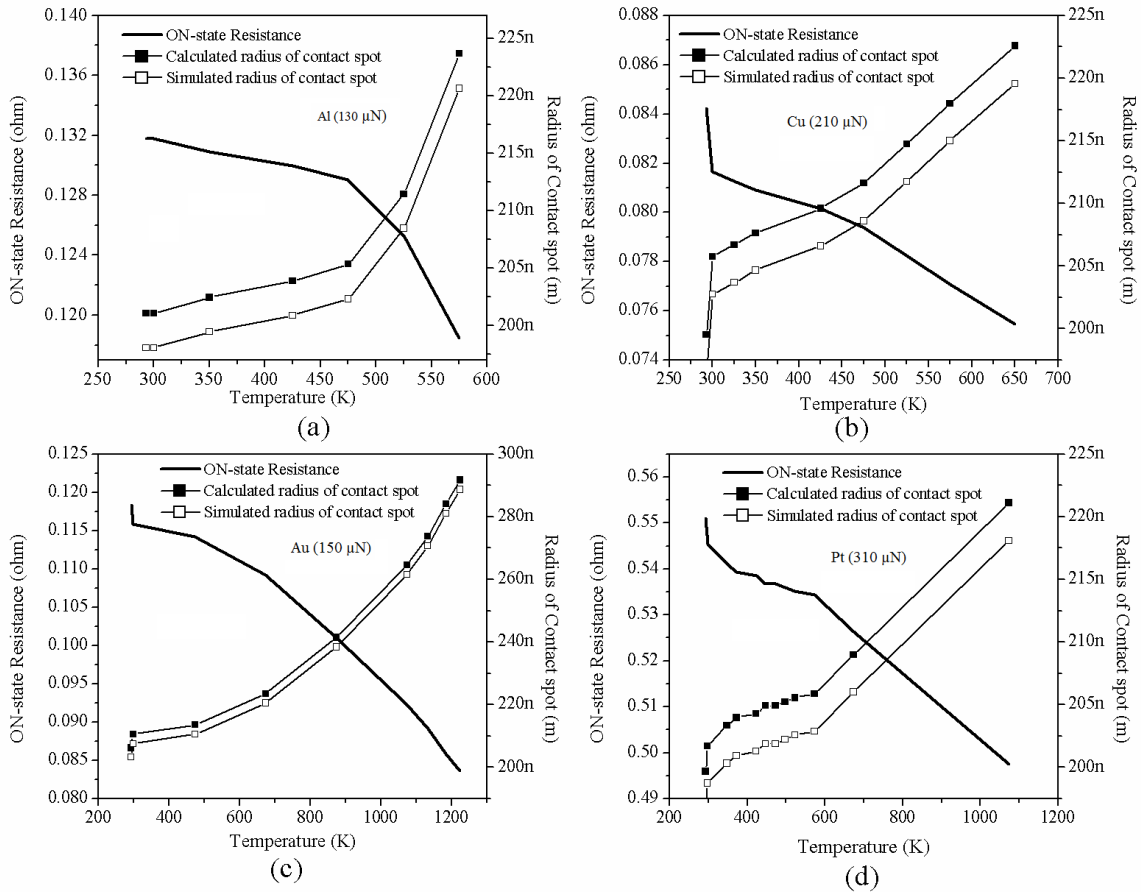


**Figure 5.9:** Temperature-resistance relationship and temperature-radius relationship of contact spot for (a) Al (b) Cu (c) Au and (d) Pt

Figure 5.9(a) shows that for Al microelectrical contact, when temperature increases, the radius of the contact spot varies from 0.2 $\mu\text{m}$  to 0.23 $\mu\text{m}$  and the resistance decreases from 0.132 $\Omega$  to 0.118 $\Omega$  approximately. Figure 5.9(b) shows that for Cu microelectrical contact, when temperature increases, the radius of the contact spot varies from 0.2 $\mu\text{m}$  to 0.25 $\mu\text{m}$  and the resistance decreases from 0.084 $\Omega$  to 0.075 $\Omega$ . Figure 5.9(c) shows that, when temperature increases the Au microelectrical contact the resistance decreases from 0.12 $\Omega$  to 0.0825 $\Omega$  and the radius of the contact spot varies from 0.2 $\mu\text{m}$  to 0.29 $\mu\text{m}$ . Figure 5.9(d) shows that for Au microelectrical contact, when temperature increases, the radius of the contact spot varies from 0.2 $\mu\text{m}$  to 0.22 $\mu\text{m}$  and the resistance decreases from 0.55 $\Omega$  to 0.495 $\Omega$ .

### 5.3.4 Current carrying capability

The current carrying capability is obtained based on temperature distribution. The temperature should not reach the melting temperature. But it is preferred that the temperature should not reach the softening temperature. Because at softening temperature structural deformation begins. This leads to resistance change and affect the design parameters. The current carrying capability also depends on the surface roughness.

#### *Smooth surface*

The following assumptions are made for the analysis of ON-state temperature distribution. The entire power is converted to heat and the whole heat input is transferred to the microelectrical contact. That is no radiation from the surface and no convection above the surface. The atmospheric temperature is assumed as 293K. The equation for the temperature rise is written as follows

$$\Delta T = I_c^2 L_{Mc}^2 / \sigma k A_c^2 \quad (5.7)$$

$$T = (I_c^2 L_{Mc}^2 / \sigma k A_c^2) + 293 \quad (5.8)$$

Where,  $T$  is the maximum anode temperature,  $I_c$  is the contact current,  $W_c$  is the width of moving contact,  $A_c = W_c \times t_c$  is the cross sectional area,  $\sigma_c$  is the electrical conductivity and  $k_c$  is the thermal conductivity of the contact material. Temperature is proportional to the square of the current through the microelectrical contact (Michael, 2011). Also the temperature is proportional to the square of the moving electrode width  $L_{Mc}$ . As  $L_{Mc}$  decreases, anode temperature decreases. This becomes an advantage for the

miniaturization of electrical contacts. However, the temperature is inversely proportional to the square of the cross sectional area. In FEM, the electrothermal behavior of microelectrical contact is modeled using the formulas given in Appendix E. The surface area of anode is connected to positive of DC source current  $I_c$ . The maximum temperature at the anode of the microelectrical contact with smooth surface is obtained for various values of currents. The calculated and simulated values of anode temperature for Al, Cu, Au and Pt microelectrical contact are given in Figure 5.10.

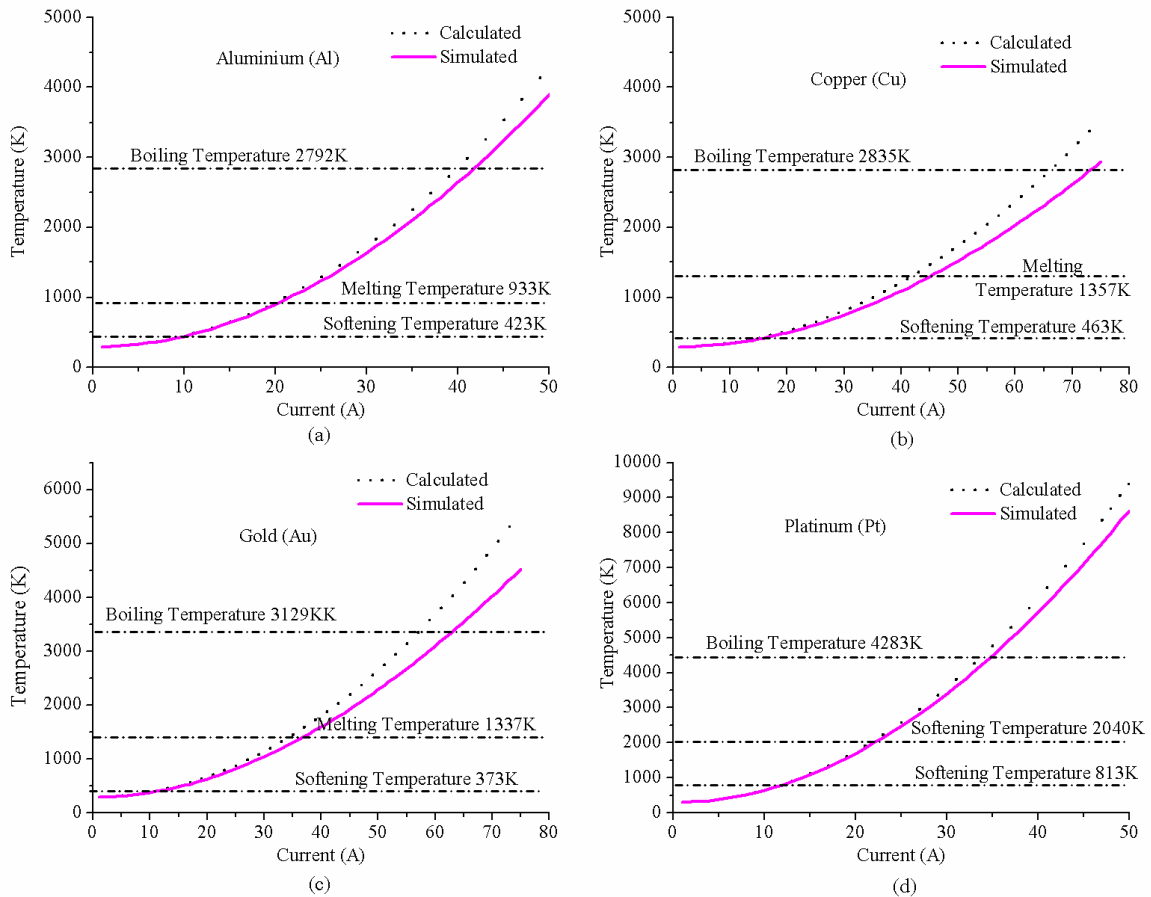


**Figure 5.10:** ON-state anode temperature of the microelectrical contact with smooth surface for (a) Al (b) Cu (c) Au and (d) Pt

The microelectrical contact should not reach its melting temperature for the given current. Al, Cu, Au and Pt microelectrical contacts reaches the softening temperature at 10A, 18A, 11A and 13A and melting temperature at 21A, 47A, 36A and 22A respectively. The current carrying capability of the microelectrical contact is predicted

based on the anode temperature. The current carrying capability of the microelectrical contact with smooth surface considered in the study for the materials Al, Cu, Au and Pt are predicted as 10A, 18A, 11A and 13A respectively.

In practical situation, the material properties changes as temperature increase. Hence current temperature relation has been carried out using the material properties as a function of temperature and is shown in Figure 5.11. This shows that the Al, Cu, Au and Pt microelectrical contacts reaches the softening temperature approximately at 8A, 14A, 9 A and 15A respectively. The Al, Cu, Au and Pt microelectrical contacts reaches the melting temperature approximately at 12A, 24A, 18 A and 21A respectively.

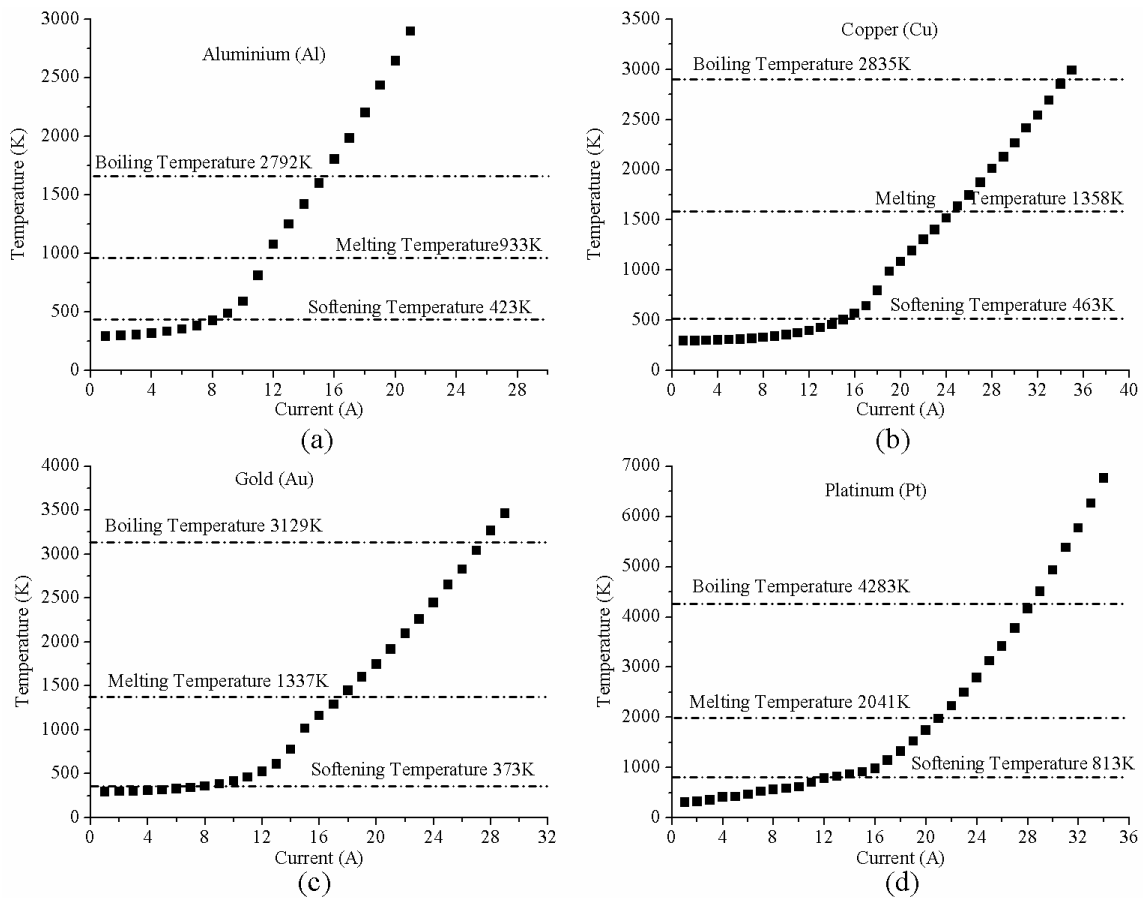


**Figure 5.11:** simulation results of ON-state temperature of the microelectrical contact with smooth surface with the material properties as a function of temperature for (a) Al (b) Cu (c) Au and (d) Pt

Figure 5.12 shows the temperature distribution of Al microelectrical contact. This shows that on the application of 10A, the anode is reaching the maximum temperature of 445K.

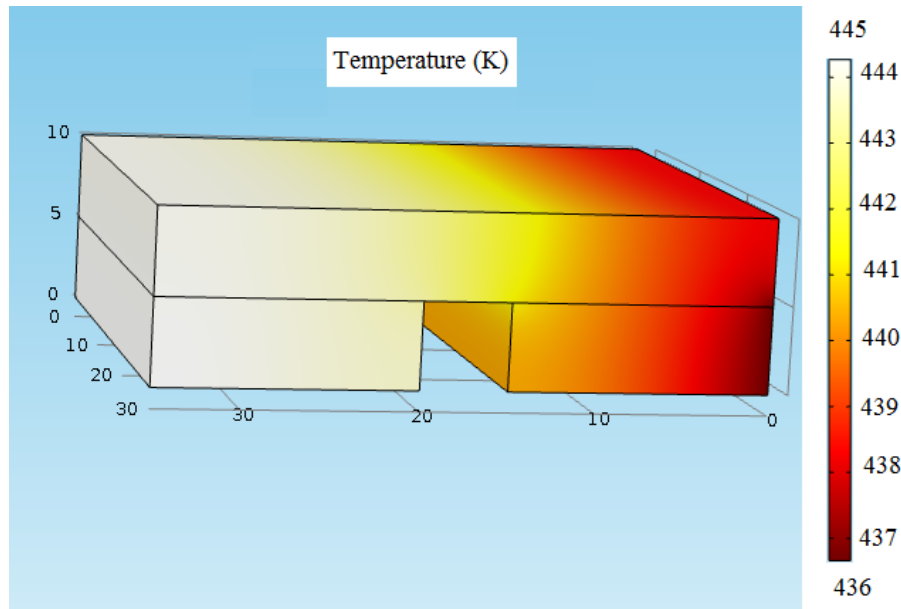


**Figure 5.12:** Surface plot of temperature distribution for Al

### ***Rough surface***

COMSOL simulation has been carried out to predict the ON-state temperature of the microelectrical contact for rough surface and the results are shown in Figure 5.13. The maximum anode temperature of the microelectrical contacts with rough surface for the materials Al, Cu, Au and Pt are given in Figure 5.13. It is a plot between current and temperature. The current carrying capability of the microelectrical contact is predicted based on the anode temperature. Figure 5.13 shows that the Al, Cu, Au and Pt microelectrical contacts reaches the softening temperature approximately at 0.2A, 0.24A, 0.21A and 0.45A respectively. Al, Cu, Au and Pt microelectrical contacts reaches the melting temperature of the material at 0.38A, 0.44A, 0.48A and 0.8A respectively.

If the temperature increases above the melting temperature, there will be problem of material transfer and welding of contacts which leads to the failure of microelectrical contact. Hence, the current flowing through the microelectrical contact considered in this study for the materials Al, Cu, Au and Pt has to be limited below 0.2A, 0.24A, 0.21A and 0.45A respectively. Figure 5.14 (a) and (b) shows the heat flow direction of the microelectrical contact with smooth and rough surface.



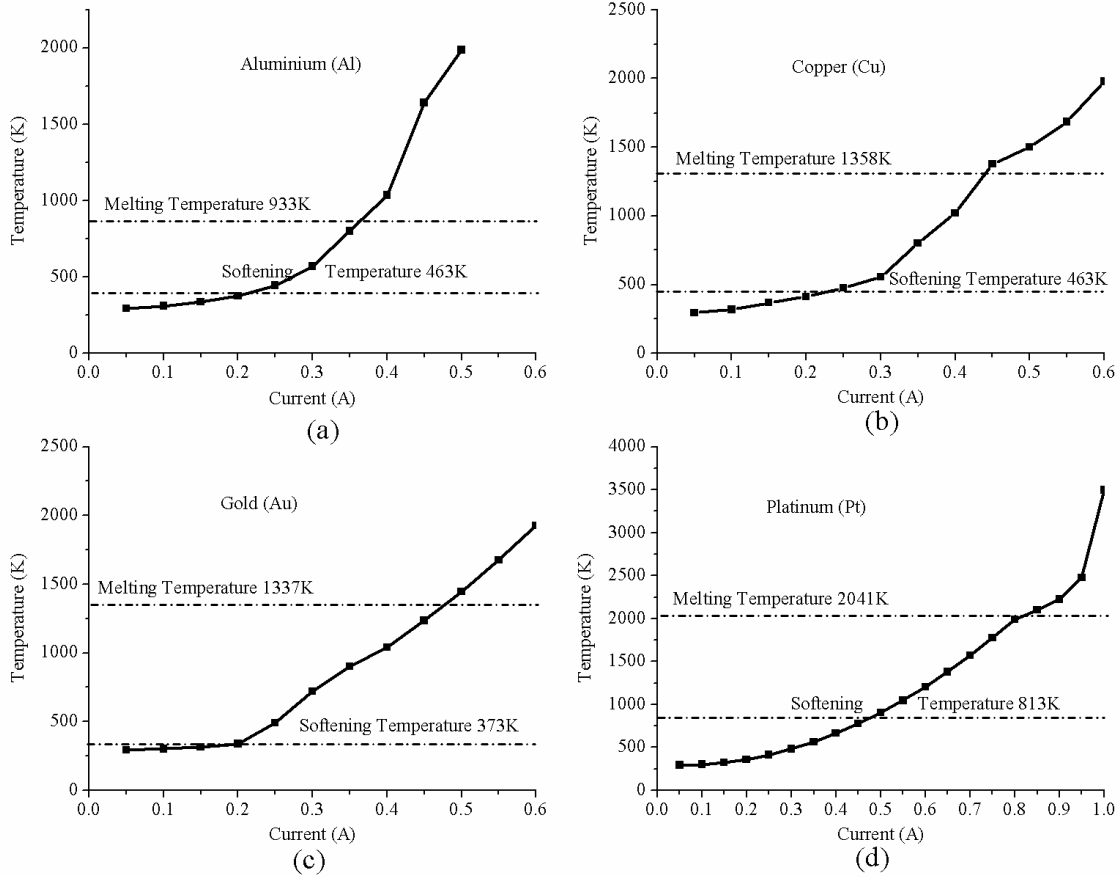


**Figure 5.13:** Simulation results of ON-state anode temperature of the microelectrical contact with rough surface for (a) Al (b) Cu (c) Au and (d) Pt

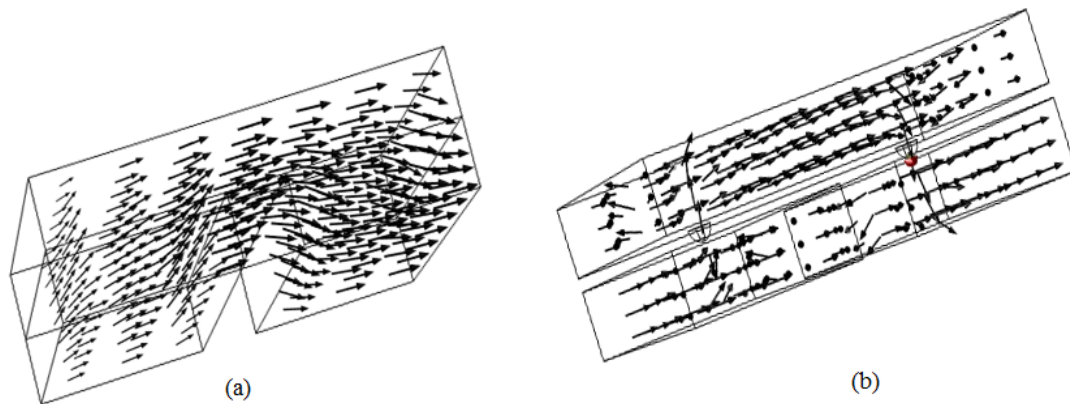


**Figure 5.14:** COMSOL surface plots of temperature flow directions of the microelectrical contact (a) with smooth surface (b) with rough surface

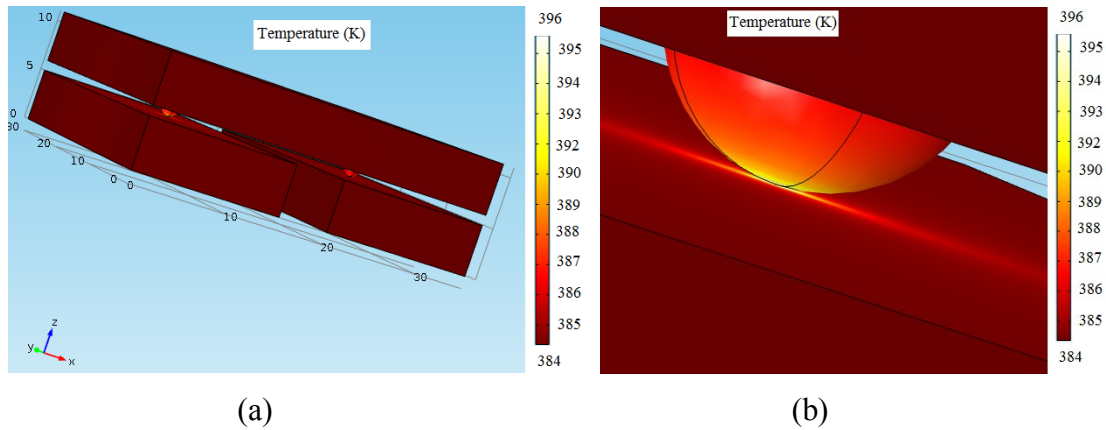


**Figure 5.15:** Surface plots of temperature distribution for rough surface (a) full view (b) projected view of contact area

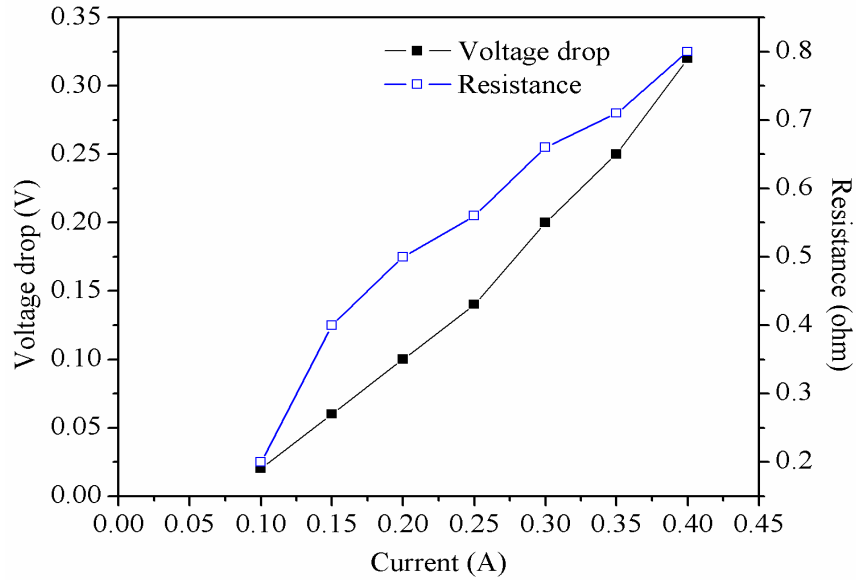
Figure 5.15 shows the surface plots of temperature distribution for rough surface. It shows that maximum temperature of 396K appears at contact area when the current flowing is 0.2A. It clearly shows that maximum temperature appears at the contact spot. If the the current reaches 0.3A, the temperature of the contact area increases above the softening temperature of Al. This leads to structural changes, which changes the resistance. Hence voltage drop increases. If the current increases above 0.4A, the temperature increases above the melting temperature and get welded at the contact area. Hence it very inportant to limit the current below 0.2 for Al microelectrical contact. During ON-state of the microelectrical contact, electromigration may also occurs. Electro-migration within the microelectrical contact is the drift of atoms within the solid metal due to electrical current flow. It is a current induced diffusion that is driven by the momentum of the electrons. When the conducting area of microelectrical contact is small, the current density may be high enough to initiate electro-migration failure. This may occur because of the interaction between the atoms of a microelectrical contact and leads to material transfer. Electro-migration may not occurs, if the current density of the microelectrical contact is less than  $<10^{10}$  A/m<sup>2</sup> (Slade 2014; Holm 2000). An increase in current density in the contact spots create the right conditions for electro-migration to occur. This electro-migration can cause material transfer which causes microelectrical contact failure and leads to reliability issues. Material transfer affects the surface topology of the microelectrical contact but the transfer may be quantitatively very small.

If the current flowing through the microelectrical contact increases above 0.38A, 0.43A, 0.42A and 0.8A for the material Al, Cu, Au and Pt respectively, the contact would melt. This causes the contacts to get welded. When contact starts separating, the melted contact material may then form a molten metal bridge. As current increases, the temperature of the microelectrical contact increases to boiling temperature and reaches evaporation temperature. This may collapse the molten metal bridge. Since the bridge does not necessarily break in the center, material can transfer between the contacts by the fine transfer mechanism. If the temperature of the microelectrical contact is above the melting temperature for metallic surfaces which lead to a transfer mechanism between two surfaces known as fine transfer or molten metal bridge phenomena. Material transfer between switching contact surfaces in microelectrical contacts causes device failure. So it is very important to keep the temperature below the melting temperature to avoid fine transfer, molten metal bridge and material transfer. In the considered microelectrical contact by limiting the current below 0.38A, 0.43A, 0.42A and 0.8A for the materials Al, Cu, Au and Pt respectively, the temperature can be limited below the melting temperature. Hence the fine transfer, material transfer and molten metal bridge formation can be avoided.

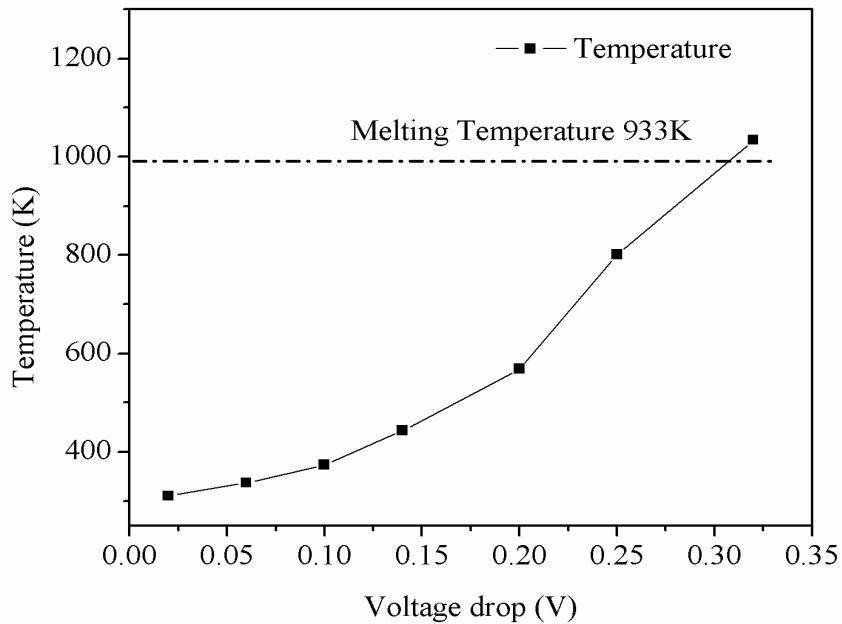
### **5.3.5 Contact voltage drop**

The contact resistance and current flowing in the microelectrical contact leads to voltage drop. The current-temperature relation and voltage drop-temperature relation has been obtained using FEM simulation. The voltage-drop and temperature simulation has been carried out for Al as an example. The simulation has been carried out with the material properties as a function of temperature and results are presented in Figure 5.16. Figure 5.16(a) shows the current-voltage drop relationship and current-resistance relationship of Al microelectrical contact. The increase in current, leads to increase in resistance and voltage drop of the microelectrical contact. When the current reaches 0.38A, the resistance increases approximately to  $0.8\Omega$  and voltage drop increases to 0.32V. Figure 5.16(b) shows the voltage drop and temperature relation of the Al microelectrical contact. At 0.31V, the temperature of the microelectrical contact reaches the melting temperature. Figure 5.17 shows the surface plot obtained from the COMSOL FEM simulation for voltage drop. Similar analysis has been carried out for Cu, Au and Pt and the voltage drop

at which the microelectrical contact reaches the melting temperature is observed. The Cu, Au and Pt microelectrical contact reaches the respective melting temperature at 0.41V, 0.416V and 0.683V respectively.

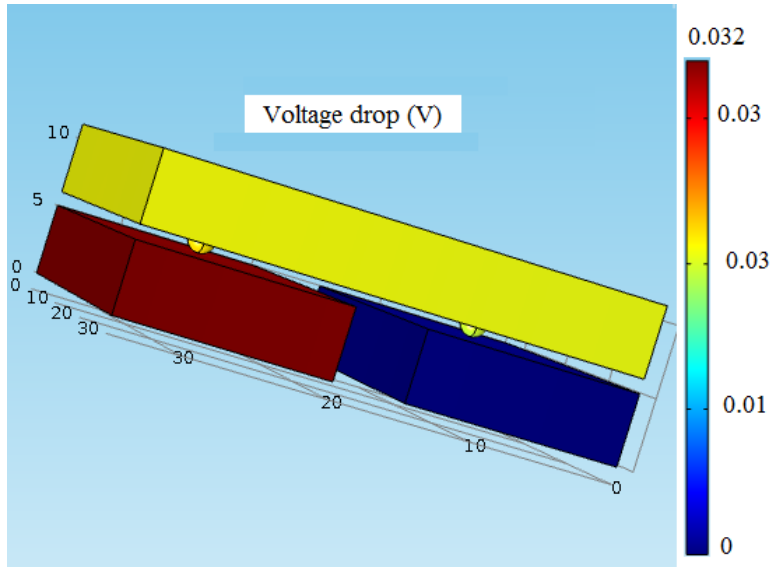


(a)



(b)

**Figure 5.16:** (a) Current-voltage drop and current-resistance relationship for Al (b) voltage drop-temperature relationship for Al



(a)

**Figure 5.17:** FEM surface plot for voltage drop

## 5.4 Switching State

During switching state of the microelectrical contact the current flow starts decreasing and voltage across the contact starts increases. During this time power appears across the microelectrical contact. This power increases the temperature of the microelectrical contact.

### 5.4.1 Steady state temperature

The anode temperature of an electrode is modeled using the 3D heat transfer equation which is given in Appendix F. At the surface of anode connected to positive terminal of the dc voltage source

$$\dot{Q}_h = P_c \quad (5.9)$$

Where  $\dot{Q}_h$  is the heat transfer rate,  $P_c$  is the contact power. The anode temperature corresponding to various power rating and material are obtained and it is shown in Figure 5.18. The Al, Cu, Au and Pt contact reaches boiling temperature at 1.6W, 2.6W, 2.3W and 4.3W respectively. Al, Cu, Au and Pt microelectrical contacts reaches melting temperature at 0.5W, 1.1W, 0.9W and 1.9W respectively. Power rating of the microelectrical contacts can be decided based on this temperature. Among the four materials platinum gives better power rating of 1.9W.

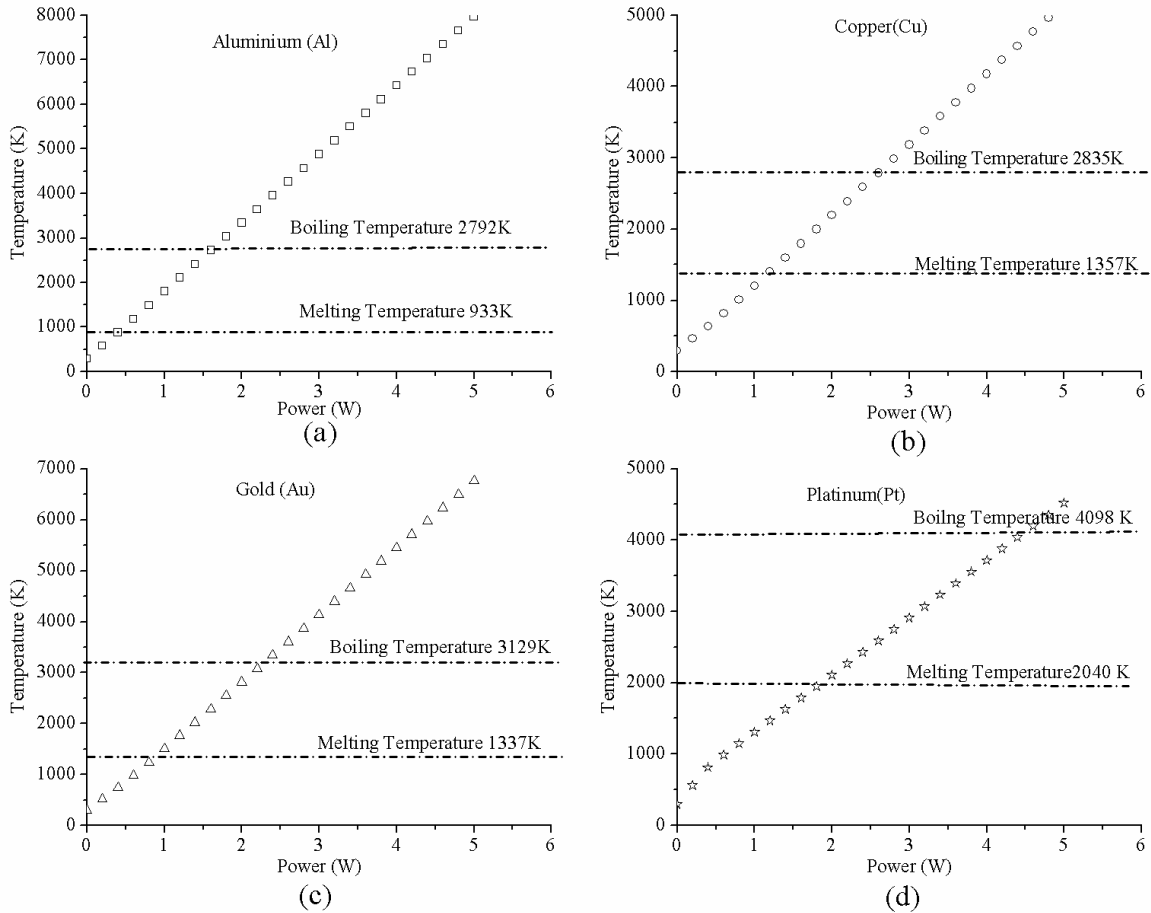


**Figure 5.18:** Power- temperature relationship for (a) Al (b) Cu (c) Au and (d) Pt

### 5.4.2 Transient Temperature

The time for which the power appears across the microelectrical contact and the switching speed are important in achieving arcless switching. Time required to reach the steady temperature is obtained using transient temperature analysis for various power ratings. The power levels of 1W, 2W, 3W, 4W and 5W are applied across the microelectrical contact and the temperature is obtained. The transient temperatures for various power levels are shown in Figure 5.19. The time lag to reach steady state value is 40  $\mu$ s for Al, Cu, Au and Pt microelectrical contact. The surface plot shown in Figure 5.20 shows the transient temperature distribution for Al microelectrical contact. It reaches 378K, 1598K, 2140K and 3202 K at 1 $\mu$ s, 5 $\mu$ s, 10 $\mu$ s and 35 $\mu$ s respectively.

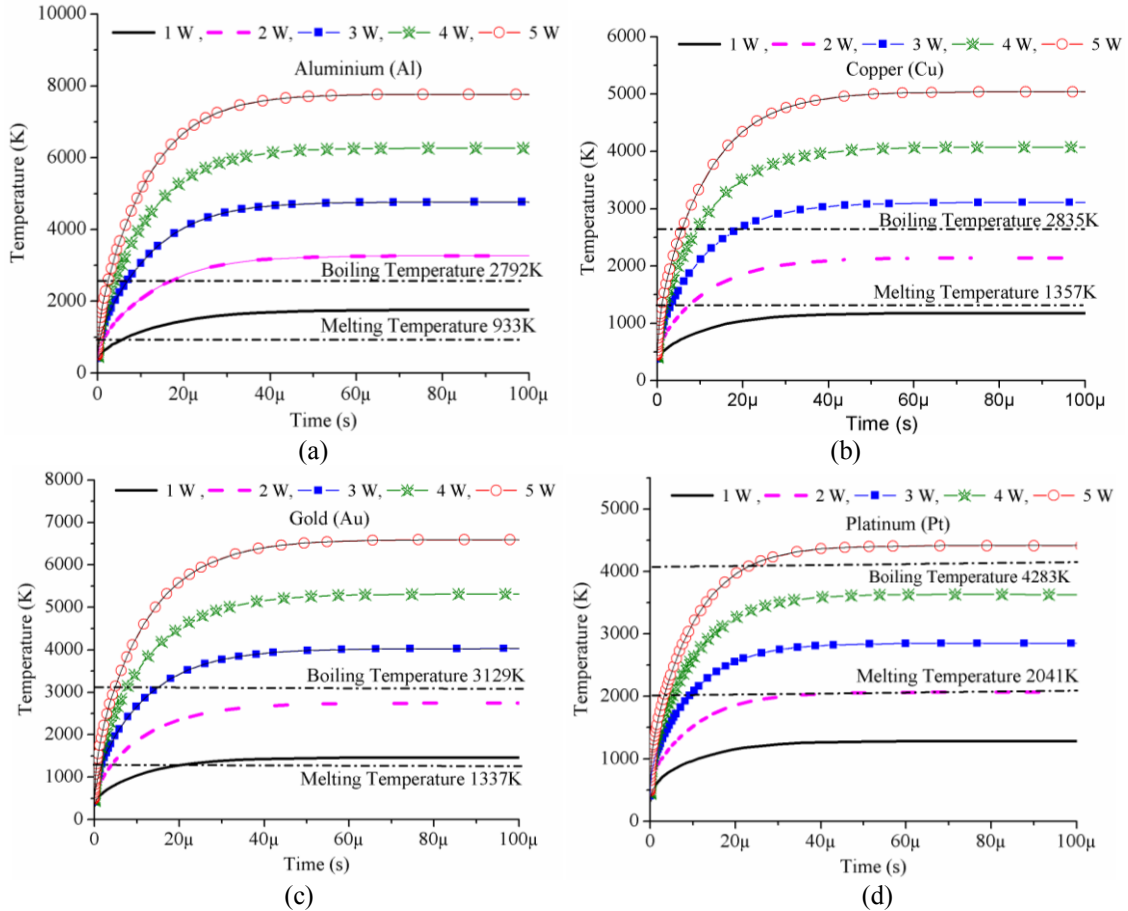


**Figure 5.19:** Transient temperature for various power levels (a) Al (b) Cu (c) Au (d) Pt

**Table 5.2:** Time lag to reach melting and boiling temperature

Power	Material	Time to reach the temperature ( $\mu$ s)		Material	Time to reach the temperature ( $\mu$ s)	
		Melting	Boiling		Melting	Boiling
1W	Al	5.28	NR	Au	23	NR
2W		1.06	20.8		4.67	NR
3W		0.488	8.05		1.83	13.9
4W		0.293	4.09		1.05	7.84
5W		0.166	3.15		0.547	4.96
1W	Cu	NR	NR	Pt	NR	NR
2W		8.55	NR		40.1	NR
3W		3.61	18.3		9.26	NR
4W		1.78	9.94		5.19	NR
5W		1.17	6.27		3.35	2.31

NR-Not Reaching

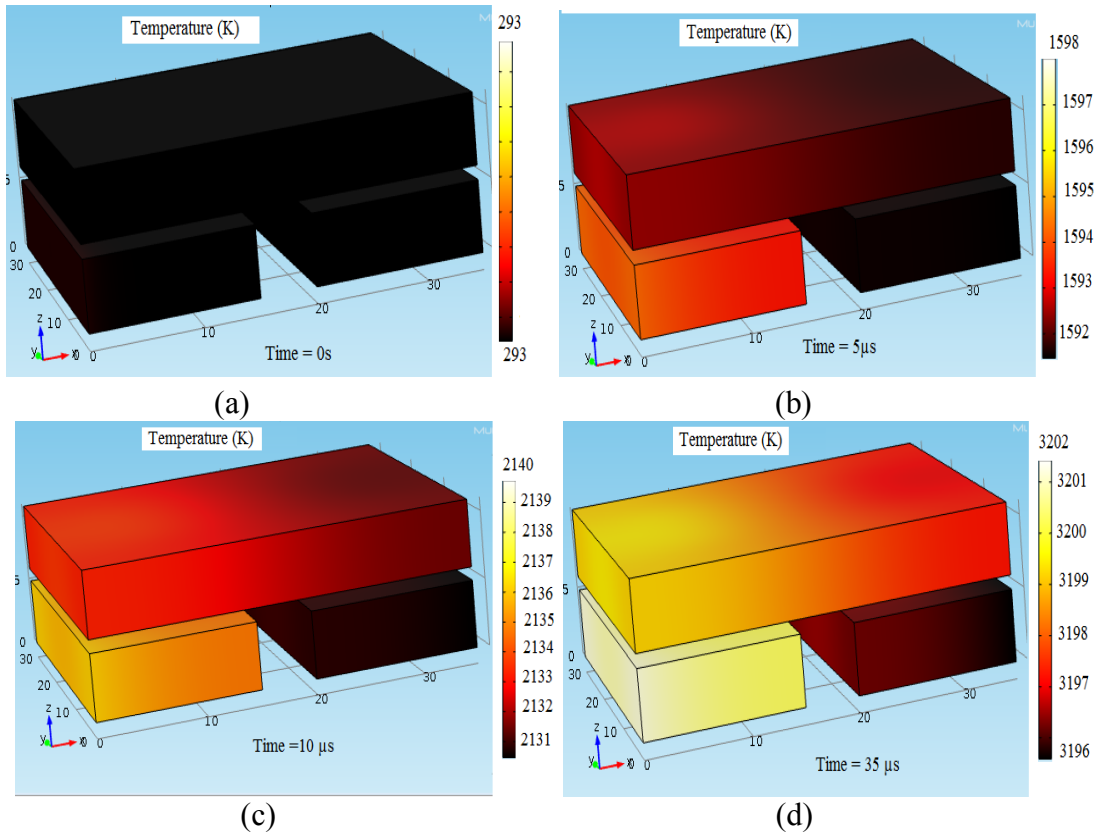


**Figure 5.20:** Temperature distribution for Al at (a) 0s (b)  $5\mu\text{s}$  (c)  $10\mu\text{s}$  (d)  $35\mu\text{s}$

The time required by the microelectrical contacts to reach melting and boiling temperature is given in Table 5.2. It is clear that, the Al, Cu and Au microelectrical contacts might withstand 5W without arcing if this power appears on the microelectrical contact for  $3.15\mu\text{s}$ ,  $6.27\mu\text{s}$ ,  $4.93\mu\text{s}$  and  $23\mu\text{s}$  respectively. Also Al, Cu, Au and Pt microelectrical contacts would not form molten metal bridge if 5W appears for  $0.166\mu\text{s}$ ,  $1.17\mu\text{s}$ ,  $0.547\mu\text{s}$  and  $3.35\mu\text{s}$  respectively. Copper and platinum withstand 1W and 2W respectively even if this power appears continuously for long time.

## 5.5 OFF-State

During OFF-state, voltage appears across the contact, but the current flowing through the contact is zero.

### 5.5.1 OFF-state capacitance

The 3D structure of a microelectrical contact at OFF-state and its equivalent capacitance are shown in Figure 5.21.



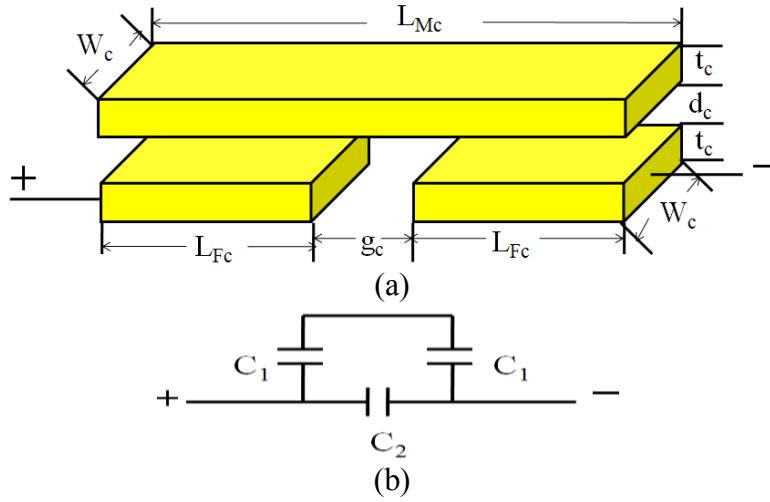


**Figure 5.21:** (a) OFF-state microelectrical contact (b) Equivalent capacitance

The OFF-state capacitance  $C_{OFF}$  of the microelectrical contact is given by

$$C_{OFF} = \frac{C_1}{2} + C_2 \quad (5.10)$$

The capacitance between the fixed and moving electrodes are given as

$$C_1 = \frac{k\epsilon_0 L_{Fc} W_c}{d_c} [C_{F1} + C_{Ft1}] \quad (5.11)$$

Where  $\epsilon_0 = 8.854 \times 10^{-12}$  F/m  $k$  is the relative permittivity of air medium  $t_c$  is the thickness and  $W_c$  is the width of the contact,  $L_{Fc}$  is the length of the fixed contacts,  $L_{Mc}$  is the length of the moving contact,  $g_c$  is the gap between fixed contact and  $d_c$  is the gap between floating and fixed contact during OFF-state.  $k\epsilon_0 L_{Fc} W_c / d_c$  is the normal capacitance,  $C_{F1}$  is the fringing field due to the finite dimensions of the electrodes and  $C_{Ft1}$  is the fringing field associated with the height of the electrical contacts.

$$C_{F1} = 1 + \frac{d_c}{\pi L_{Fc}} + \frac{d_c}{\pi L_{Fc}} \ln \left( \frac{2\pi L_{Fc}}{d_c} \right) \quad (5.12)$$

$$C_{Ft1} = \frac{d_c}{\pi L_{Fc}} \ln \left( 1 + \frac{2t_c}{d_c} + 2\sqrt{\frac{t_c}{d_c} + \frac{t_c^2}{d_c^2}} \right) \quad (5.13)$$

The capacitance between the fixed contacts anode and cathode is given as

$$C_2 = \frac{k\varepsilon_0 t_c W_c}{g_c} [C_{F2} + C_{Ft2}] \quad (5.14)$$

$$C_{F2} = 1 + \frac{g_c}{\pi t_c} + \frac{g_c}{\pi t_c} \ln \left( \frac{2\pi t_c}{g_c} \right) \quad (5.15)$$

$$C_{Ft2} = \frac{t_c}{\pi t_c} \ln \left( 1 + \frac{2L_{Fc}}{t_c} + 2\sqrt{\frac{L_{Fc}}{t_c} + \frac{L_{Fc}^2}{t_c^2}} \right) \quad (5.16)$$

$k\varepsilon_0 t_c W_c / g_c$  is the normal capacitance,  $C_{F2}$  is the fringing field due to the finite dimensions of the microelectrical contact and  $C_{Ft2}$  is the fringing field associated with the thickness of the microelectrical contacts (Leus and Elata, 2004).

The OFF-state capacitance is calculated for various contact gaps  $d_c$  between 1 and 10  $\mu\text{m}$ . The calculation results are compared with the simulation results obtained using COMSOL FEM simulation. The OFF-state capacitance of the microelectrical contact is given in Figure 5.22. When the gap increases from 1 $\mu\text{m}$  to 10 $\mu\text{m}$ , the capacitance varies between 3fF to 1.2fF.

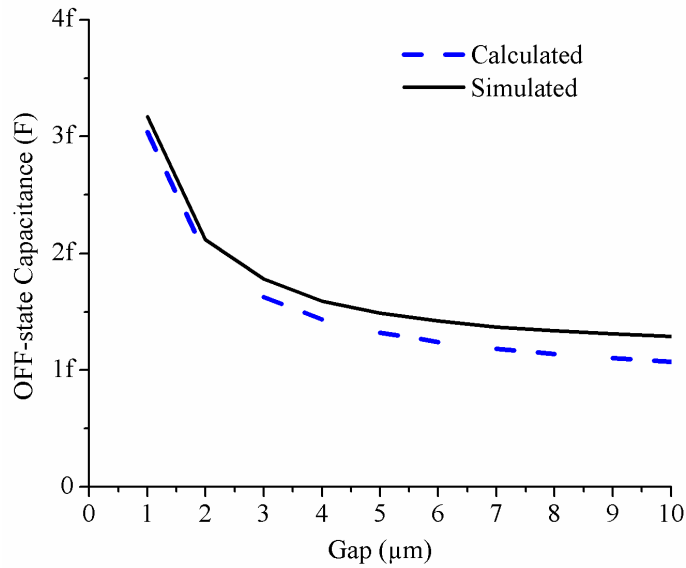


**Figure 5.22:** OFF-state capacitance

### 5.5.2 Electric field

The electric field across anode and cathode is given as

$$E_c = \frac{Q_c V_c}{\varepsilon_0 L_{Fc} W_c} \quad (5.17)$$

Where  $E_c$  is the contact electric field and  $Q_c$  is the charge of the microelectrical contact. The electric field distribution is obtained based on Maxwell's equations and are given in Appendix C. The contact voltage  $V_c$  is varied between 0V and 100V. The gap considered between fixed and floating electrode is 5  $\mu\text{m}$ . The results obtained for various voltage levels are shown in Figure 5.23.

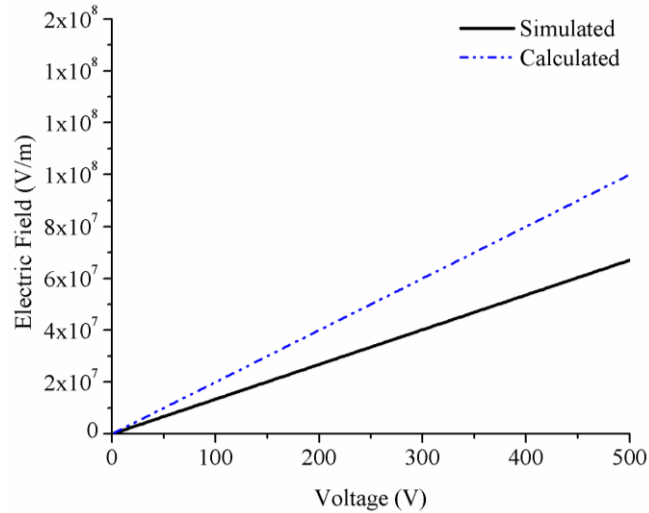


**Figure 5.23:** OFF-state electric field

The material does not have any influence on the capacitance and the electric field. The surface plot shown in Figure 5.24(a) shows that the capacitance of microelectrical contact is  $1.35e^{-15}\text{F}$ . Figure 5.24(b) and (c) shows the surface and slice plot showing the voltage distribution of 20V. The slice plot shown in Figure 5.24(d) shows the electric field distribution for the applied voltage of 20V. The maximum electric field obtained is  $2.93 \times 10^6 \text{V/m}$ . The electric field is distributed between anode and cathode. This electric field distribution shows that arc occurs between anode and cathode.

The arc which occurs during OFF-state of the microelectrical contact is breakdown arc. This has been studied in chapter 4. For achieve arcless switching, the voltage appearing across anode and cathode must be below the breakdown voltage given by modified Paschen curve. Also the electric field produced across anode and cathode should be below the breakdown electric field.

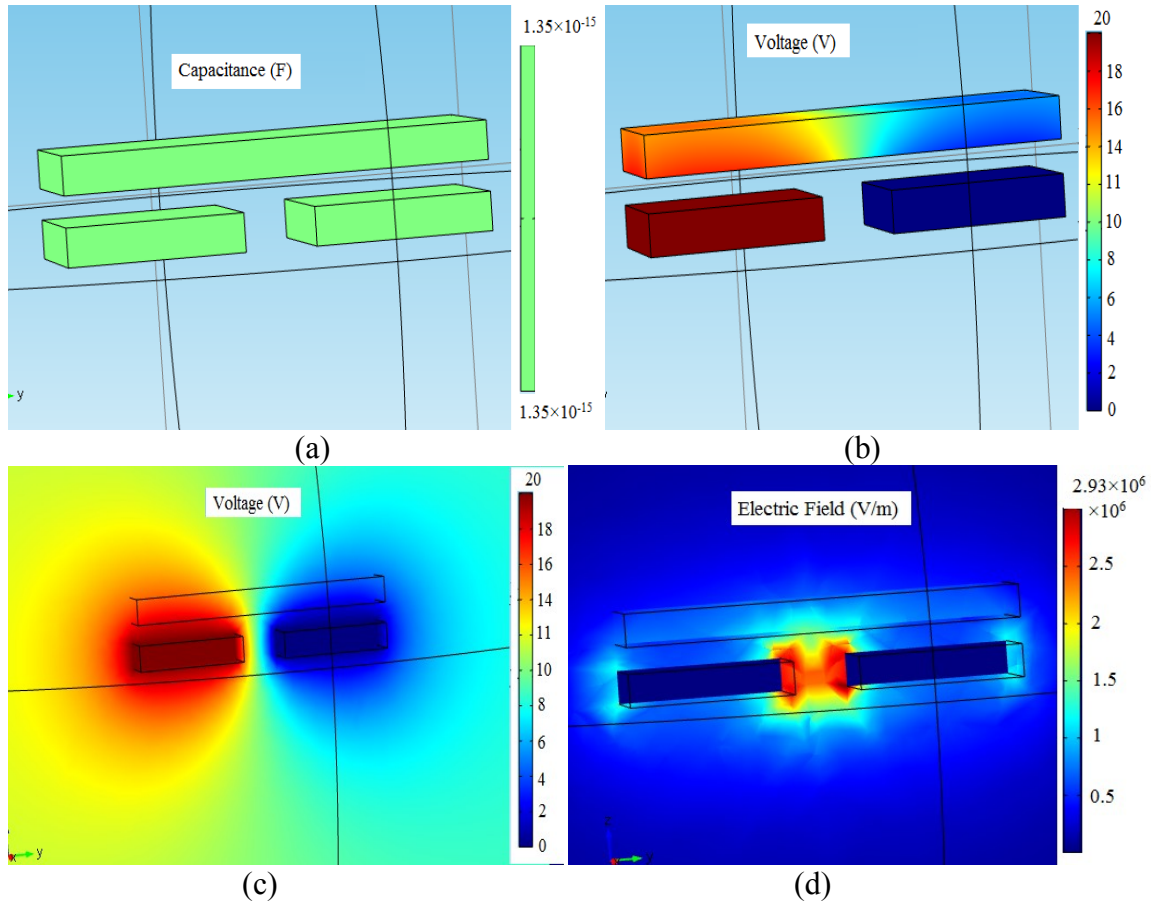


**Figure 5.24:** OFF-state FEM analysis results (a) surface plot of capacitance (b) surface plot of voltage (c) slice plot of voltage and slice plot of electric field

As discussed in Figure 4.4, chapter 4, the  $5\mu\text{m}$  can withstand  $5e^7\text{V/m}$  without arcing. The microelectrical contact considered reaches  $5e^7\text{V/m}$  at approximately 150V. Hence voltage below 150V can't generate arc between anode and cathode.

## 5.6 Discussion on Contact Welding and Arc Occurrence

The micromechanical switches uses microelectrical contact to allow and interrupt the electrical current. These microelectrical contacts have low ON-state resistance, low power losses, high isolation, no leakage current, high breakdown voltage and small size. The challenges in commercializing such switches are reliability and durability of the contact. The major cause responsible for reliability is contact welding during ON-state, arc during switching and OFF-state. The current-temperature relation, power-temperature relation and electric field have been analyzed for the design of arcless microelectrical contact.

Four cases with different current, power and voltage are considered and the possibility of contact welding, occurrence of pre-breakdown arc and breakdown arc are discussed in this section. These four cases are as follows:

$$\text{Case A: } I_c = 0.4\text{A}, P_c = 1.3\text{W}, V_c = 12\text{V}$$

$$\text{Case B: } I_c = 1.2\text{A}, P_c = 7.5\text{W}, V_c = 12\text{V}$$

$$\text{Case C: } I_c = 1\text{A}, P_c = 98\text{W}, V_c = 400\text{V}$$

$$\text{Case D: } I_c = 0.05\text{A}, P_c = 5\text{W}, V_c = 400\text{V}$$

Where  $I_c$  the maximum is current flowing through the contact during ON-state,  $P_c$  is the maximum power appearing across the contact during switching state and  $V_c$  is the maximum voltage across the microelectrical contact. The gap between anode and cathode  $g_c$  is 5  $\mu\text{m}$  for all the four cases. The occurrence of contact welding and arc has been investigated for the materials Al, Cu, Au and Pt. The possibility of contact welding and occurrence of arc due to various mechanisms such as anode temperature, contact voltage and contact electric field for the four cases are given in Table 5.3.

In case A, during ON-state maximum current flowing is 0.4A, which is sufficient to increase the temperature of the microelectrical contact to boiling temperature for the materials Al and Au. This leads to contact welding. But in case of Cu and Pt contacts won't reach the boiling temperature. Hence there is no possibility of contact welding. During switching time maximum power of 1.3W appears across the microelectrical contact. At 1.3W, Al and Au contacts reach its boiling temperature. This leads to vaporization of contact material and produces arc. Since Cu and Pt not reaching boiling temperature, it might not cause arc. If 1.3W appear for less than 2 $\mu\text{s}$ , arc might not occur. During OFF-state, 12V appears across anode and cathode. This voltage is below the breakdown voltage given by modified Paschen curve. The electric field produced by this voltage is less than the breakdown electric field for all four materials. Hence breakdown arc won't occur.

**Table 5.3:** Occurrence of arc due to various mechanism

Case	Material	Contact Welding	Pre-breakdown arc		Breakdown arc	
			Arc due to anode temperature	Arc due to anode temperature , if the maximum power appear for 2 $\mu$ s	Arc due to contact voltage	Arc due to contact electric field
A	Al	YES	YES	NO	NO	NO
	Cu	NO	NO	NO	NO	NO
	Au	YES	YES	NO	NO	NO
	Pt	NO	NO	NO	NO	NO
B	Al	YES	YES	YES	NO	NO
	Cu	YES	YES	YES	NO	NO
	Au	YES	YES	YES	NO	NO
	Pt	YES	YES	YES	NO	NO
C	Al	YES	YES	YES	YES	YES
	Cu	YES	YES	YES	YES	YES
	Au	YES	YES	YES	YES	YES
	Pt	YES	YES	YES	YES	YES
D	Al	NO	YES	YES	YES	YES
	Cu	NO	YES	YES	YES	YES
	Au	NO	YES	YES	YES	YES
	Pt	NO	YES	YES	YES	YES

YES means arc occurs and NO means arc does not occurs

Similarly case B can cause contact welding and pre-breakdown arc and may not cause breakdown arc for all the materials. Case C can cause contact welding, pre-breakdown arc and breakdown arc for all the materials. In case D, since the current is 0.05A, it won't cause contact welding. But the high voltage leads to high power, which causes pre-breakdown arc. The high voltage increases the electric field above breakdown electric field and causes breakdown arc.

While designing arcless micromechanical switch, it is very important that the switch should not produce both pre-breakdown and breakdown arc. In practical situations, the

geometry of the microelectrical contact changes once it reaches its softening temperature. This leads to change in resistance, voltage drop, and power dissipation. This increases the temperature. This affects the material properties which again increases the heat. So, it is very important to maintain the temperature of the microelectrical contact below the softening temperature.

In microelectrical contacts, roughness is at nanometer scale and the contact forces are in the order of micro-newton. During ON-state of the switch, few asperities of the microelectrical contact surfaces are effectively in touch. The possibility of touching more asperities of the contact surface can be improved by increasing the contact force. This leads to increase in contact area, which reduces the contact resistance and increases the current carrying capability. In practical microelectrical contacts, the applied forces should be strong enough to neglect the surface roughness effects. Also, since the current carrying capability and reliability of microelectrical contact is determined by the presence of these nano-asperities, surface roughness needs to be maintained below a certain level in order to avoid detrimental effects on contact resistance.

## **5.7 Conclusion**

This chapter presented the electrothermal design, modeling and analysis of arcless microelectrical contact.

- The structure of the microelectrical contact and the reliability affecting phenomena such as contact welding and arc are presented. The occurrence of pre-breakdown arc and breakdown arc are investigated for the materials Al, Cu, Au and Pt.
- The ON-state resistances for smooth and rough surface microelectrical contact are modeled using FEM and the results are compared with the analytical results. Electrothermal analysis has been carried out and current carrying capability of 8A, 14A, 9A and 15A are obtained for Al, Cu, Au and Pt microelectrical contact with smooth surface. Electrothermal analysis has been carried out to predict the current carrying capability of the rough surface microelectrical contact and 0.2A, 0.24A, 0.2A and 0.45A are obtained for Al, Cu, Au and Pt respectively. The temperature distribution has been obtained using FEM simulation. The variation in resistance and voltage-drop as a function of current has been investigated. It is

observed that more temperature appears at the contact spot. The maximum allowable voltage-drop of the microelectrical contact has been obtained as 0.31V, 0.41V, 0.416V and 0.683V for Al, Cu, Au and Pt respectively. The effect of force on the resistance has been discussed. Also the analysis has been carried out to obtain the effect of temperature on the contact spot and resistance. The result shows that the material and roughness has major factor in the design of microelectrical contact.

- The steady state and transient temperature as a function of power has been obtained using simulation for the switching state. The power withstanding capability has been investigated. The maximum power which the microelectrical contact can withstand without arc has been found as 0.5W, 1.1W, 0.9W and 1.9W for Al, Cu, Au and Pt respectively. The transient analysis shows that the microelectrical contact needs 40 $\mu$ s to reach steady state temperature.
- During OFF-state, capacitance of the microelectrical contact is obtained using FEM simulation and results are compared with the mathematical calculations. The electric field distribution is obtained and it is identified that arc may occur across anode and cathode during OFF-state. The capacitance of the considered microelectrical contact is obtained as  $1.35e^{-15}$ F.
- Four cases with different voltage, current and power levels are investigated to analyze the occurrence of arc due to pre-breakdown and breakdown arc phenomenon.



# CHAPTER 6

## ELECTROMECHANICAL MODELING AND ANALYSIS OF ARCLESS MICROMECHANICAL SWITCHES

### 6.1 Introduction

Electrostatically actuated micromechanical switches have electrical and mechanical components together on a chip to perform desired task. The design of these switches needs coupling between electrical and mechanical systems. The failure modes have to be analyzed for the design of reliable micromechanical switch (Li and Jiang, 2008). The failure modes mainly depend on the design and materials used for the switch. The fabrication approach and the packaging also play an important role in the reliability of micromechanical switches (Li and Jiang, 2008). The failure modes are broadly classified into mechanical failure modes and the electrical failure modes. The mechanical failure modes include stiction, wear, fatigue, deformation, curvature change, shock and vibration induced fracture. Short circuit due to contact welding, arc across driving electrode, arc on the microelectrical contact, electrostatic discharge (ESD) and corrosion are electrical failure modes (Shea, 2006). Arc across driving electrode has been discussed in chapter 4. The contact welding and arc in microelectrical contact are discussed in chapter 5. In general, reliable micromechanical switches are designed through material, circuitry and structural approaches (Song and Yoon, 2016). For designing reliable switch through material approach, researchers are working on metal alloy, refractory metals, dissimilar contact materials and cantilever beam materials (Coutu et al., 2006; Hiltmann et al., 2002). In circuitry approach, external circuit is connected across the microelectrical contact in order to achieve arcless switching. This method is also called as cold switching (Chan et al., 2003).

This chapter proposes to design arcless micromechanical switch through structural approach while hot switching. In this approach, first the structure of single electrostatically actuated micromechanical switch is designed. The electromechanical parameters such as spring constant, actuation voltage, force, switching speed and

quality(Q) factor (damping factor) are depends on the structure and material of the switch. The influence of these parameters on the performance, deformation of the cantilever beam and reliability of the device is also discussed. The structure of the electrostatically actuated micromechanical characteristics are analyzed using higher order finite element tool, Coventor MEMS+. The performance parameters are obtained using Coventor MEMS+ along with MATLAB Simulink. The performance parameters are obtained using simulation and the results are verified with calculated results.

In micromechanical switches arc may occur in four parts. They are

1. Across driving electrode
2. In microelectrical contact
3. Across anode and cathode of the microelectrical contact
4. Between actuation pad and anode of the microelectrical contact

This work proposes to design and analyze the micromechanical switch of 12V, 0.2A. The arcless nature of the switch needs to be analyzed with more emphasis on micromechanical parameters.

In order to enhance the voltage and current rating TCT array has been proposed in chapter 3. This study proposes to enhance the rating of 140V/3A by connecting switches in TCT array. The designed arcless micromechanical switches are connected in a 15×12 TCT array configuration to get higher rating of 140V, 3A. This structure divides the voltage appears across single switching element and reduces the current flows through each switch. This structure considerably reduces the contact resistance and losses. This approach uses hot switching to achieve arcless switching. Coventor MEMS+ tool interfaced with Cadence Virtuoso is used for system level simulation.

## **6.2 Structural Design of Electrostatically Actuated Micromechanical Switches**

In the design of micromechanical switch, dimension and material of the cantilever beam and driving electrode have more influence. The mathematical modeling is used to derive the performance parameters such as spring constant, actuation voltage, electrostatic force, switching speed and Q factor.

### 6.2.1 Structure of electrostatically actuated micromechanical switch

The cantilever based micromechanical switch is considered for power switching applications, as discussed in chapter 3. The beam is fixed at one end and the other is freely moving. The switch has base, anchor, cantilever beam, driving electrode and microelectrical contact. The basic structure and operation of the electrostatically actuated micromechanical switch has been discussed in section 3.5, chapter 3. The top view and side view of the considered micromechanical switch is shown in Figure 6.1.

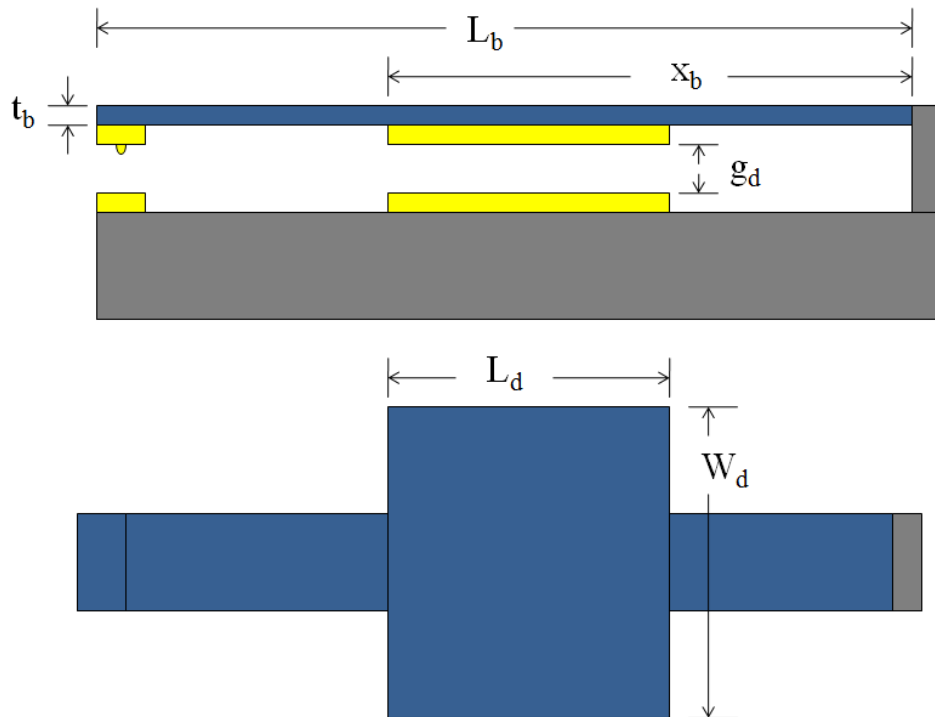


**Figure 6.1:** Micromechanical switch (a) side view (b) top view

The driving voltage applied across driving electrode creates electrostatic force. This pulls the free end of the cantilever beam downwards. Hence the floating contact gets in touch with anode and cathode. This completes the DC signal path, thus the switch become ON-state. The cantilever beam is then back to the original position once the driving voltage is removed or reduced. Hence disconnects the DC current and become OFF-state.

### 6.2.2 Mathematical modeling

In order to achieve arcless and reliable micromechanical switch, parameters such as actuation voltage, force, switching speed and Q factor has to be analyzed. The performance parameters are obtained using following equations:

### ***Spring constant***

The actuation voltage depends on the spring constant  $K$  of the beam and is given by (Vu et al., 2012)

$$K = 3E_b W_b \left( \frac{t_b}{L_b} \right)^3 \left( \frac{1 - \left( \frac{x_b}{L_b} \right)}{3 - 4 \left( \frac{x_b}{L_b} \right)^3 + \left( \frac{x_b}{L_b} \right)^4} \right) \quad (6.1)$$

Where  $L_b$  is the length of the cantilever beam,  $x_b$  is the distance of the beam from anchor to end of the driving electrode,  $t_b$  is the thickness of the beam,  $W_d$  is the width of the driving electrode and  $E_b$  is the effective young's modulus of the beam. The spring constant depends on material properties and physical dimensions of the beam.

### ***Actuation voltage***

Actuation voltage is the driving voltage at which the cantilever moves down and become ON-state (Dumas et al., 2011)

$$V_{act} = \sqrt{\frac{8K g_d^3}{27 \varepsilon_o L_d W_d}} \quad (6.2)$$

Where  $V_{act}$  is the actuation voltage,  $g_d$  is the gap across driving electrodes,  $L_d$  is the length of the driving electrodes.

### ***Collapse voltage***

If the voltage across the driving electrode increases, at a particular voltage, the driving electrodes touches each other and the micromechanical switch fails to operate is called collapse voltage (Coutu et al., 2004).

### ***Force***

When the voltage is applied between the driving electrodes, the electrostatic force attracts them towards each other. There are three types of forces involved in micromechanical switches. Contact force is the force at the microelectrical contact, electrostatic force is the force developed due to the actuation voltage and restoring force is the force opposite to the electrostatic force (Sedaghat-Pisheh and Rebeiz, 2010; Oberhammer and Stemme, 2006).

$$F_{electrostatic} = F_{contact} + F_{restoring} \quad (6.3)$$

The electrostatic force is given by

$$F_{electrostatic} = \frac{\varepsilon_o \varepsilon_r A_d V_{act}^2}{2g_d^2} \quad (6.4)$$

Where  $\varepsilon_r$ , the relative permeability of the air,  $\varepsilon_o$  is the  $8.854e^{-12}$ .

### ***Quality factor***

The quality of an oscillatory system is characterized by dimensionless parameter called the quality (Q) factor. The Q factor characterizes the rate of the energy transformation in a system. Quality factor is the number of system oscillations over its characteristic time.

$$Q = \frac{\sqrt{E_b \rho_b}}{\mu A_d^2} t_b^2 g_b^3 \quad (6.5)$$

$$A_d = L_d W_d \quad (6.6)$$

$$\mu = 1.2566 \times 10^{-6} \times \sqrt{T} \left( 1 + \frac{110.33}{T} \right)^{-1} \quad (6.7)$$

$A_d$  is the area of the driving electrode,  $T$  is the temperature in Kelvin and  $\rho_b$  is the density of the beam. The  $Q$  factor should be in the range of 0.5 to 2 to achieve a critically damped switching (Rebeiz, 2003).

### ***Switching speed***

The switching time  $t_s$  of micromechanical switches depends on the mechanical structure and is proportional to the voltage across the driving electrodes (Vu et al., 2012). The voltage across driving electrodes should be kept 1.2 times of the actuation voltage to obtain good performance of the micromechanical switch (Rebeiz, 2003).

### **6.2.3 FEM modeling**

In order to visualize the switching action and to verify the mathematical model, micromechanical switch is designed using higher order FEM tool MEMS+. In MEMS+, the switch has to be specified by providing the fabrication process steps. The fabrication process steps considered for the design of electrostatically actuated micromechanical switch, material and depth of the layers are given in Table 6.1.

The geometric parameters considered are  $L_b=520\mu\text{m}$ ,  $x_b=400\mu\text{m}$ ,  $t_b=5\mu\text{m}$ ,  $W_d=260\mu\text{m}$ ,  $L_d=240\mu\text{m}$  and  $g_d=6\mu\text{m}$ . The dimensions of the microelectrical contact of the micromechanical switch are: fixed contact (anode and cathode)  $L_{Fc}=15\mu\text{m}$ ,  $W_c=30\mu\text{m}$ ,  $t_c=5\mu\text{m}$  each and floating contact  $L_{Mc}=35\mu\text{m}$ ,  $W_c=30\mu\text{m}$ ,  $t_c=5\mu\text{m}$ . The gap between fixed contacts  $g_c$  is  $5\mu\text{m}$  and the radius of contact spot is  $0.2\mu\text{m}$ . These dimensions are same as discussed in chapter 5.

**Table 6.1:** Fabrication process step input used for MEMS+ simulations

Step	Action	Material	Layer	Thickness ( $\mu\text{m}$ )
1	Base	Silicon	Substrate	30
2	Deposit	Metal	Anode, cathode, lower driving electrode	5
3	Deposit	Photo resist	Sacrificial	6
4	Deposit	Metal	Dimple	0.2
5	Deposit	Metal	Upper driving electrode, floating electrode	6
6	Deposit	Poly silicon	Cantilever	5
7	Delete	Photo resist	Gap	6

The schematic of the switch designed using MEMS+ tool is shown in Figure 6.2. Point A is the tip of the cantilever, point B is the starting of the driving electrode, point C is the end of driving electrode and point D is fixed end of the cantilever.

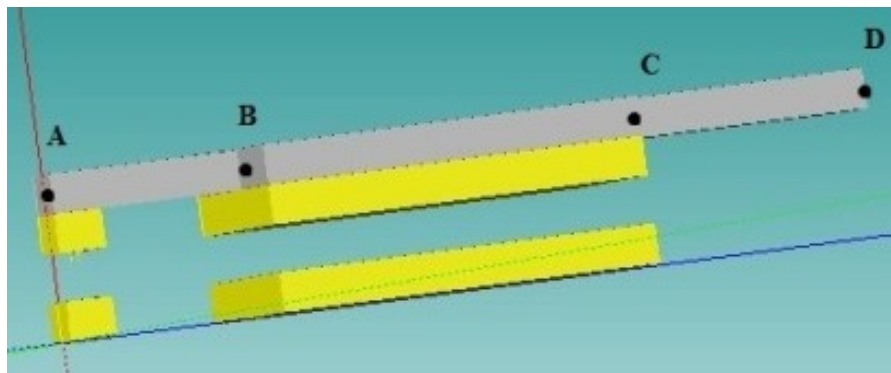


**Figure 6.2:** Schematic of the micromechanical switch designed using MEMS+

### 6.2.4 Performance analysis

Simulation has been carried out using MEMS+ with MATLAB Simulink to visualize the switching action and collapse of the micromechanical switch. The electrical and mechanical performance characteristics such as actuation voltage, collapse voltage, Q factor, electrostatic force, contact force, restoring force and switching time are also obtained. The cantilever beam is made up of poly-silicon. Driving electrodes and microelectrical contact are made up of similar metal. The design and analysis of micromechanical switch has been carried out for the metals Al, Cu, Au and Pt. Since the physical size of poly-silicon is more compared to metal, poly-silicon has more influence on the performance characteristics of the switch. The calculation and simulation results of performance parameters such as actuation voltage, Q factor and electrostatic force are given in Table 6.2.

**Table 6.2:** Performance parameters

Performance	Driving electrode and Contact metal							
	Al		Cu		Au		Pt	
	Cal	Sim	Cal	Sim	Cal	Sim	Cal	Sim
$V_{act}$ (V)	38	40	41.5	40	38.8	40	44	40
Q	0.48	0.52	0.75	0.8	0.9	0.82	1.1	0.97
F( $\mu$ N)	11.2	11.9	13.2	14.1	11.5	12	14.9	15

Cal-Calculation                      Sim- Simulation

Collapse voltage of 59.5V, 61.5V, 60V and 64.5 V are obtained using simulation for Al, Cu, Au and Pt respectively. From Table 6.2, it is clear that, the influence of contact metal is less on the performance parameters because of the smaller dimensions. Hence for further analysis, the micromechanical switch with gold contact has been considered. The mechanical movement of the beam for various driving voltage are visualized using MEMS+ tool and is shown in Figure 6.3.

The driving voltage across the driving electrodes  $V_d$  is varied from 0 to 80V. The point A of the beam move downwards by  $6\mu\text{m}$  and the floating electrode touches the anode and cathode at 40V. This voltage is called as actuation voltage  $V_{act}$ . As the voltage increases, the beam bends as seen in Figure 6.3. At 60 V the actuation pads touches each other and

the switch fail to operate as switch. This voltage is the collapse voltage  $V_{col}$ . Further increase in voltage leads to failure of the switch.

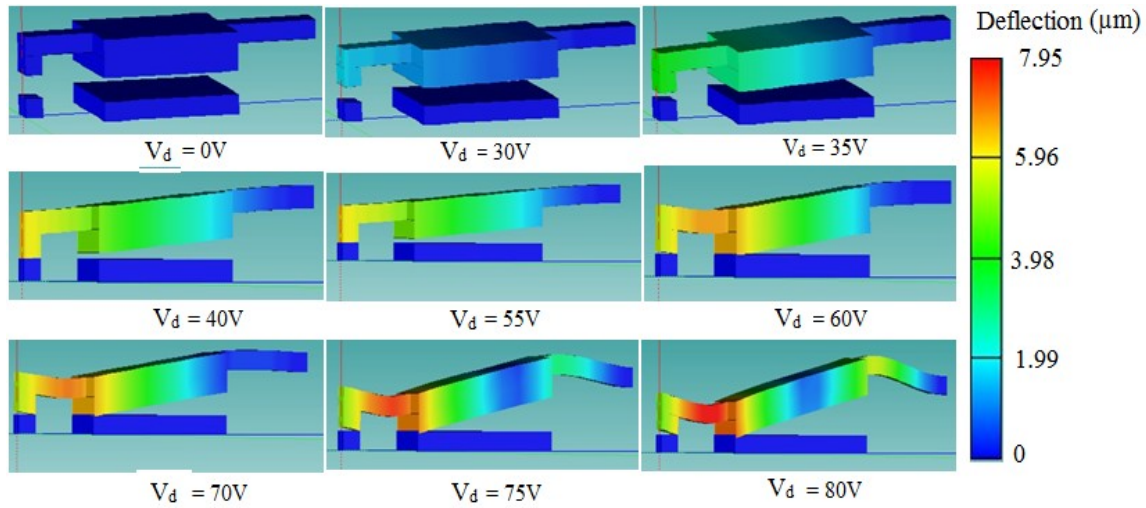


**Figure 6.3:** Mechanical movements of the micromechanical switch with respect to driving voltage

The deflection of the beam point A, point B and point C with respect to driving voltage is shown in Figure 6.4. The tip of the beam point A is moving downwards and touches the bottom electrode at 40V. The tip remains in the same position till 60V. If the voltage across the driving electrode is above 60V the tip of the cantilever moves in the upward direction. The driving electrode end point B is also moving downwards and reaching  $4.5\mu\text{m}$ . Hence the gap between top and bottom driving electrode is  $1.5\mu\text{m}$ . If the voltage is further increased, the point B moves downwards by  $6\mu\text{m}$  and touches each other. Further increase in voltage may leads to damage of the switch. At 40V, the driving electrode point C moves downwards and the gap is about  $1\mu\text{m}$ . The point D of the cantilever beam is fixed, hence the displacement is zero.

The actuation voltage of the designed switch is 40V and the driving voltage should be 1.2 times of actuation voltage. Hence the driving voltage of 48V is applied across the driving electrode. Transient analysis has been carried out using MEMS+ and MATLAB Simulink. The deflection at point A, B and C of the cantilever with respect to time is shown in Figure 6.5. At  $100\mu\text{s}$ , the voltage across the driving electrode is brought to 48V, and point A bent for  $6\mu\text{m}$  downwards at  $220\mu\text{s}$ . Hence the ON-time of the micromechanical switch is  $120\mu\text{s}$ . The voltage across the driving electrode is brought



down to 0V at 400 $\mu$ s and the beam point A moves upward and reaches OFF-state at 520 $\mu$ m. Hence OFF-time of the micromechanical switch is also 120 $\mu$ s. The transient movement visualization of the switch is shown in Figure 6.6.

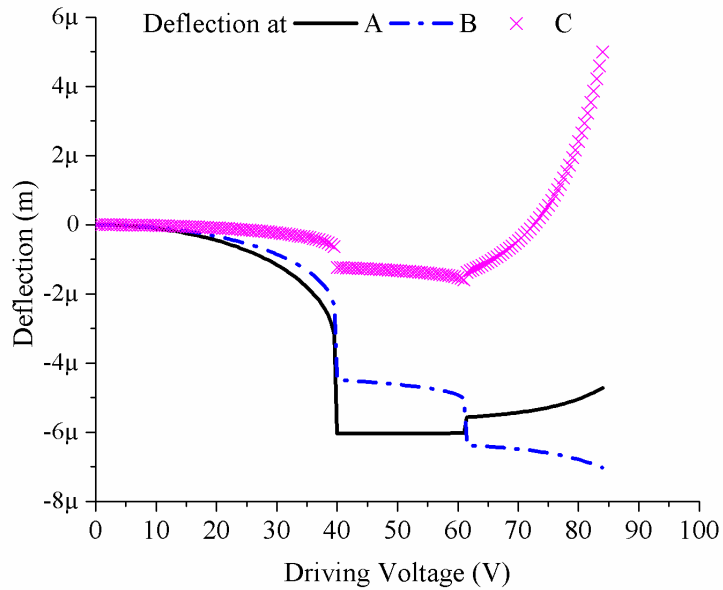


**Figure 6.4:** Deflection of point A, B and C with respect to driving voltage

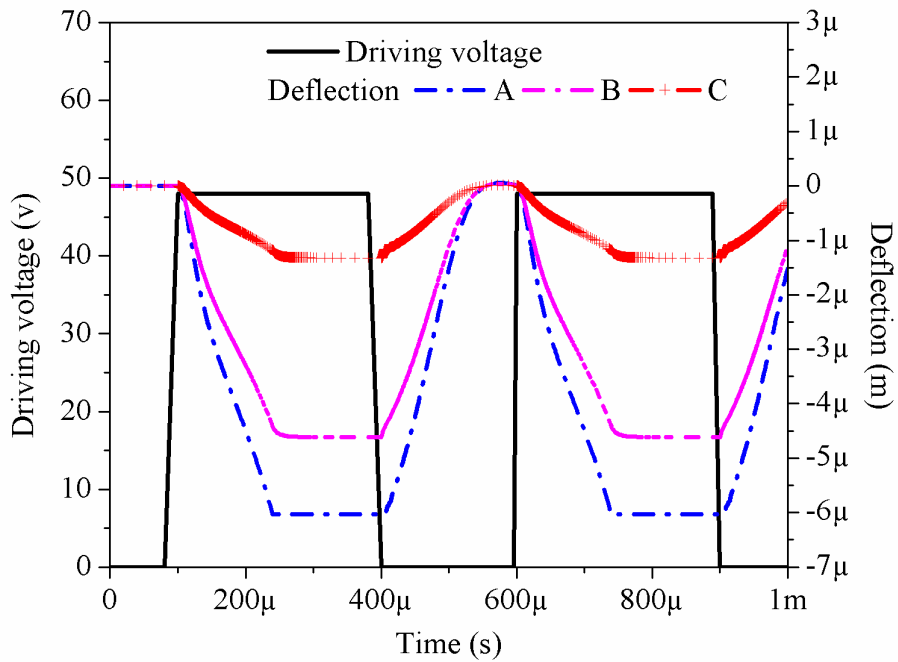


**Figure 6.5:** Voltage across the driving electrode, deflection of point A, B and C with respect to time

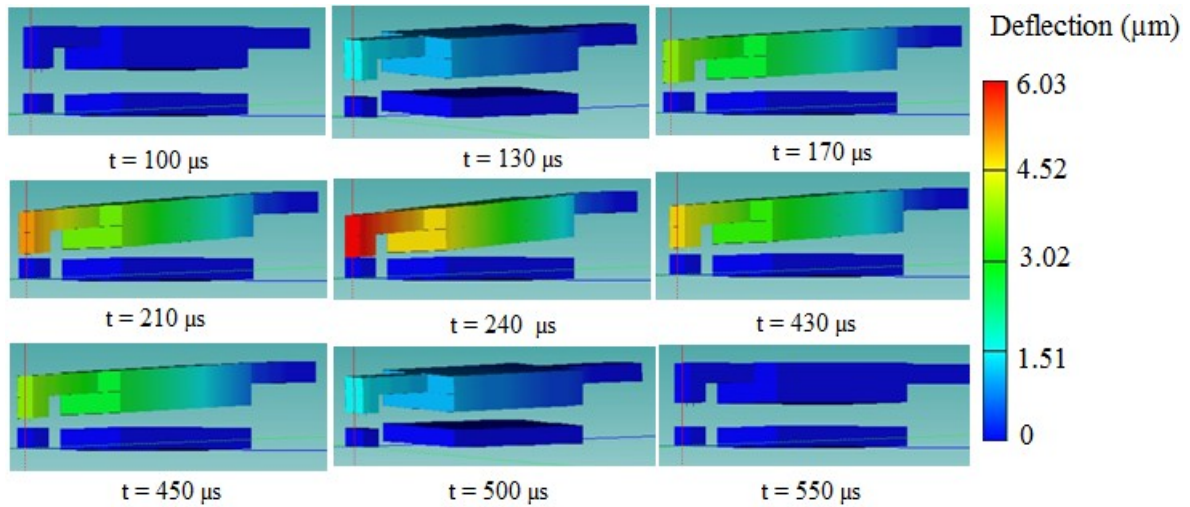


**Figure 6.6:** Transient switching states of the switch

The voltage across the driving electrodes is varied from 0V to 48 V and the electrostatic, contact force and restoring force are obtained. Figure 6.7 shows that when driving voltage of 48V is applied, electrostatic, contact and restoring forces are obtained as 32.54 $\mu$ N, 95.73 $\mu$ N and 63.19 $\mu$ N respectively. The switching speed is obtained as 120 $\mu$ s.

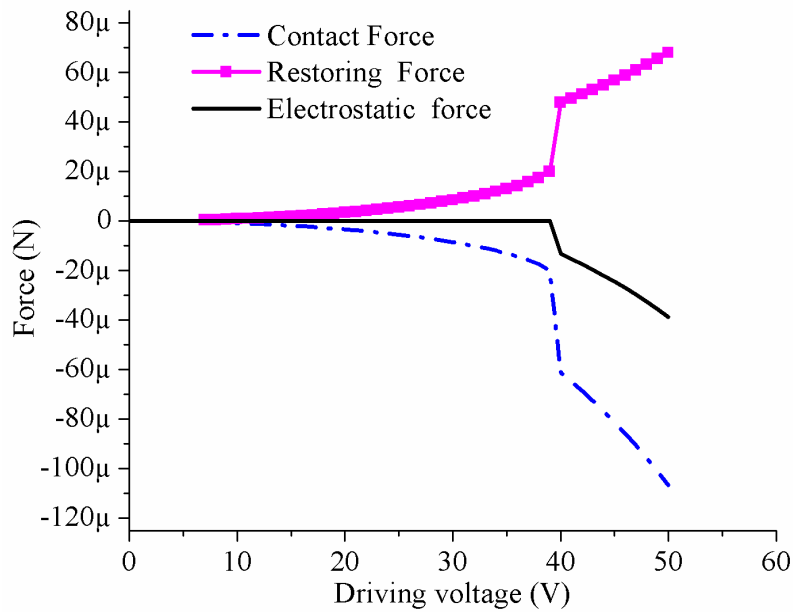


**Figure 6.7:** Force with respect to voltage across driving electrodes

The switching speed, electrostatic force, contact force and restoring force with respect to various voltages across driving electrodes are given in Table 6.3. It shows that increase in

voltage across driving electrode considerably increases the switching speed and force. Increasing voltage further leads to increase in force and damage the switch.

**Table 6.3:** Switching speed and force with respect to voltage across the driving electrodes

Driving voltage (V)	Switching speed ( $\mu\text{s}$ )	Electrostatic force ( $\mu\text{N}$ )	Restoring force ( $\mu\text{N}$ )	Contact force ( $\mu\text{N}$ )
40	185.8	13.2	47.92	61.2
45	129.8	24.41	56.81	81.2
50	117.8	38.76	68	106.8
55	103.18	58.49	82.87	141.4
60	78	91.53	106.3	197.8

When the voltage across the driving electrode increases, the cantilever beam moves downwards. Hence the gap between the driving electrodes decreases and the capacitance increases. The capacitance between the driving electrodes and the capacitance between floating electrode & anode are obtained for driving voltage from 0V to 50 V and are shown in Figure 6.8.

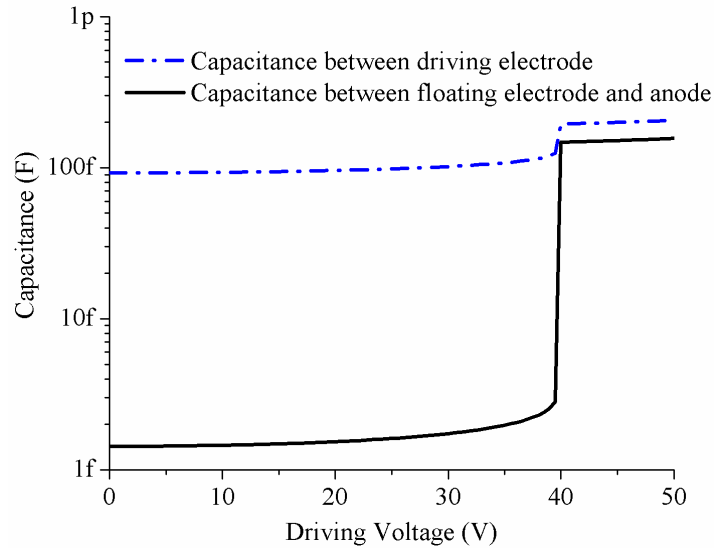


**Figure 6.8:** Capacitance with respect to voltage across the driving electrodes

The capacitance between driving electrodes varies between  $9.24e^{-14}\text{F}$  and  $2.02e^{-13}\text{F}$ . The capacitance between floating electrode and anode varies between from  $1.56e^{-15}\text{F}$  to  $1.54e^{-14}\text{F}$ .

<sup>13</sup>F. Since the dimensions and material of anode is same as cathode, the capacitance between floating electrode and cathode also varies between from  $2.5e^{-15}$ F to  $1.5e^{-13}$ F. The capacitance between the driving electrodes and the capacitance between floating electrode and anode with respect to time for the driving voltage given in Figure 6.5 are shown in Figure 6.9.

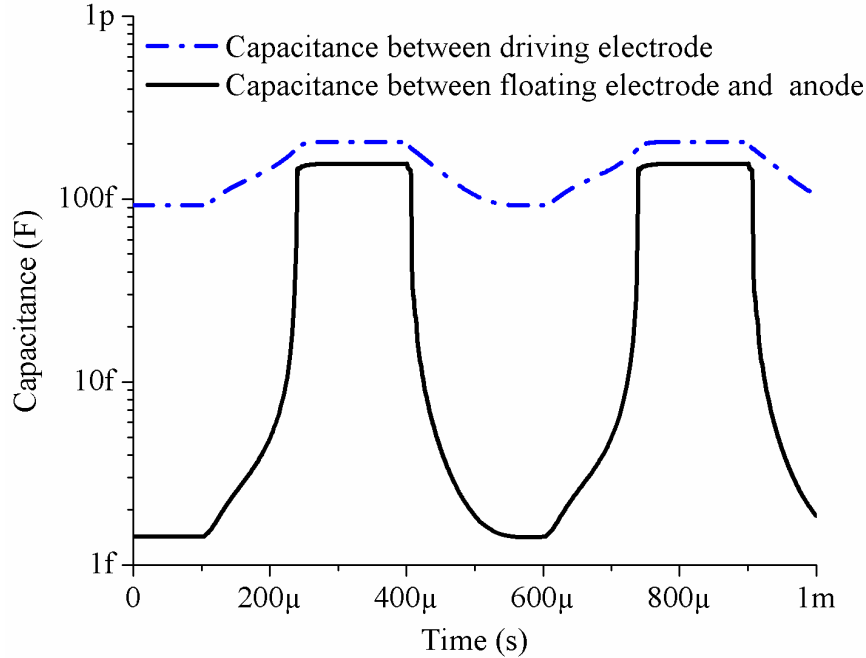


**Figure 6.9:** Capacitance with respect to time

This micromechanical switch can be operated till the softening temperature of the electrode and microelectrical contact material to enhance stability. The softening temperature of Al, Cu, Au and Pt are 423K, 463K, 373K and 813K respectively.

### 6.3 Effect of Q Factor

Q factor of the micromechanical switch should be between 0.5 and 2 to achieve better performance and reliability. And also it is a very important design parameter. If the Q factor of the switch is below or above the range may lead to deformation or oscillation of the beam. In order to analyze the effect of Q factor on the design of micromechanical switches two cases are considered and are as follows:

Case X:  $L_b=600\mu\text{m}$ ,  $x_b=495\mu\text{m}$ ,  $t_b=2\mu\text{m}$ ,  $W_d=300\mu\text{m}$ ,  $L_d=345\mu\text{m}$  and  $g_d=6\mu\text{m}$

Caser Y:  $L_b=400\mu\text{m}$ ,  $x_b=295\mu\text{m}$ ,  $t_b=6\mu\text{m}$ ,  $W_d=100\mu\text{m}$ ,  $L_d=195\mu\text{m}$  and  $g_d=6\mu\text{m}$

The driving electrode and the microelectrical contact material are made up of gold. The actuation voltage, electrostatic force, switching speed and Q factor are obtained using mathematical calculation and Coventor MEMS+ simulation and the results are given in Table 6.4. The collapse voltage is obtained as 11V and 131V for case X and case Y respectively.

**Table 6.4:** Performance parameters for case X and case Y

Parameter	Case X		Case Y	
	Calculation	Simulation	Calculation	Simulation
Actuation voltage (V)	6.44	7.6	107.09	109
Electrostatic force ( $\mu\text{N}$ )	0.528	0.43	20.2	18.5
Q factor	0.052	0.06	23	23

### 6.3.1 Deformation of the beam

Table 6.4 shows the case X micromechanical switch having low actuation voltage. This leads to less force and slow switching. Also the Q factor of the switch is very low. In order to discuss the performance and reliability, the transient simulation analysis has been carried out.

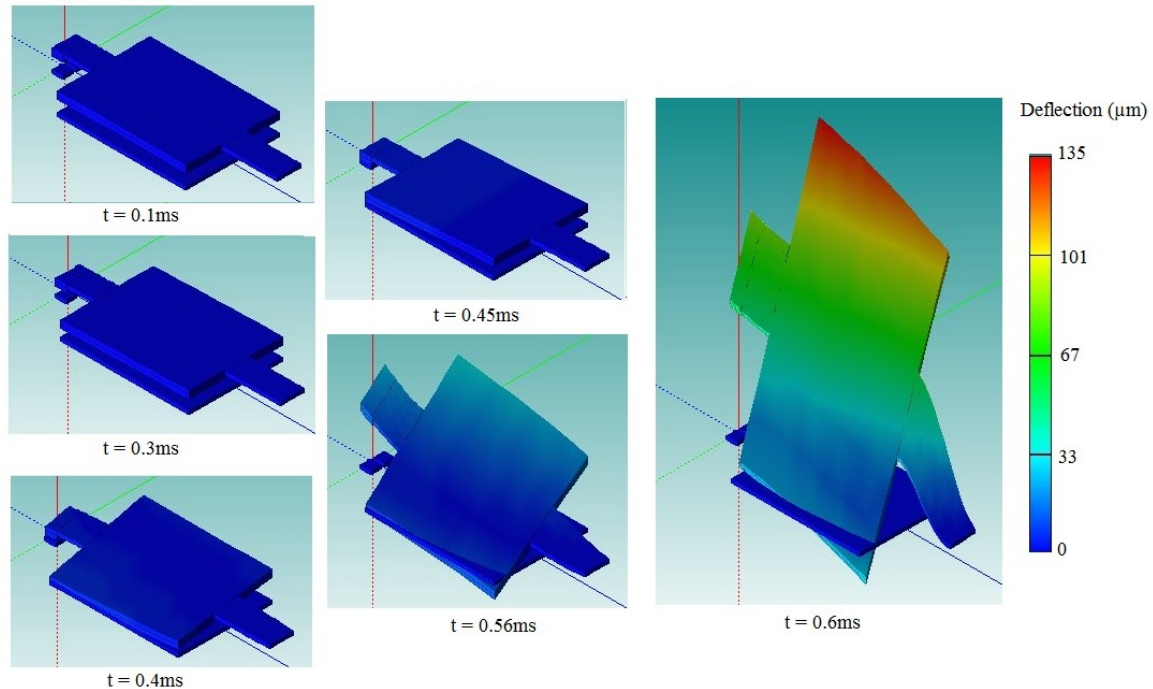


**Figure 6.10:** Deformation of beam for case X

The transient simulation has been carried for the period of 0s to 500ms. Since the driving voltage should be 1.2 times of the actuation voltage, 9V is applied across the driving electrode at 1ms. The switch become ON-state at 0.4ms. But at 0.45ms the beam started deforming and moves away from ON-state. This is because the force is not sufficient to hold the beam in the position of ON-state. The transient behavior and beam deformation are shown in Figure 6.10. This is the mechanical failure of micromechanical switch. Hence case X micromechanical switch may not be suitable to perform switching action.

### 6.3.2 Under-damped system

Table 6.4 shows the case Y micromechanical switch having high actuation voltage of 107V. This leads to high force and fast switching. Also the Q factor of the switch is very high. In order to discuss the performance and reliability, the transient simulation analysis has been carried out for the time period between 0 $\mu$ s to 1000 $\mu$ s. The driving voltage of 120V is applied across the driving electrode at 100 $\mu$ s as shown in Figure 6.11.

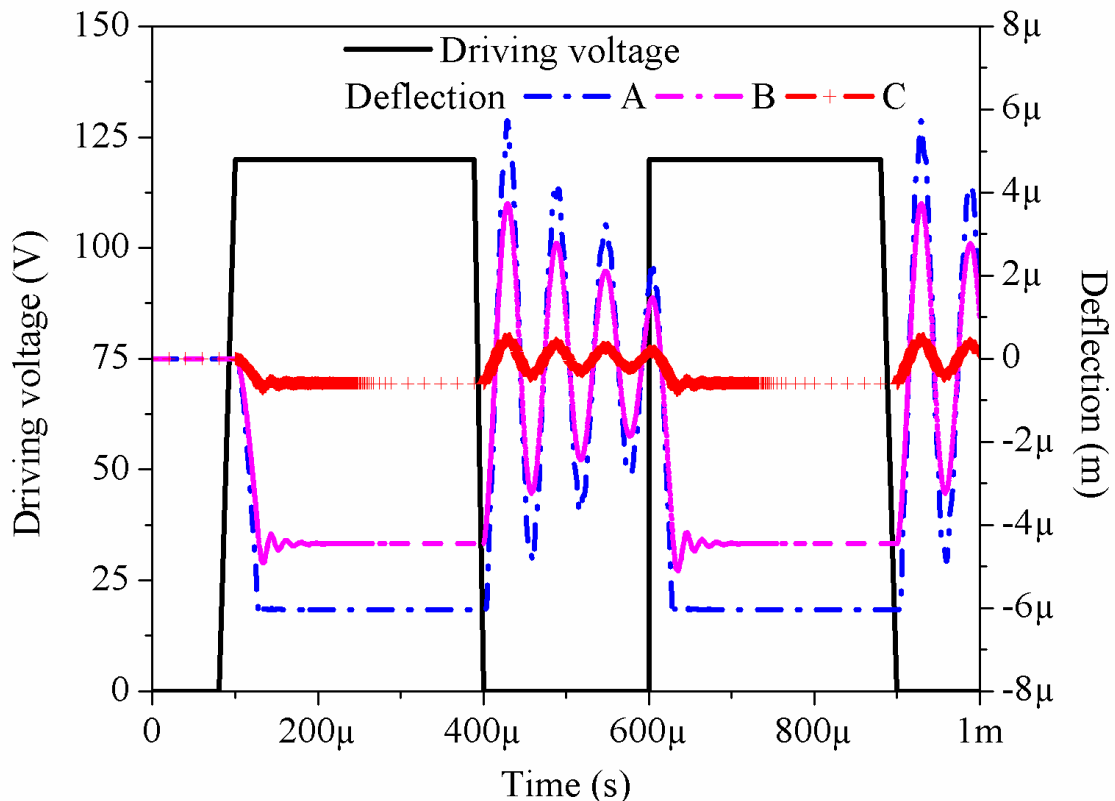


**Figure 6.11:** Driving voltage and beam deflection with respect to time for case Y

The switch reaches ON-state at  $110\mu\text{s}$ . Hence the switching speed is  $10\mu\text{s}$ . The driving voltage is removed at  $400\mu\text{s}$  and the beam tip moves upwards and produces oscillations. This design leads to under-damped system. This design may perform switching action with poor performance.

During ON-state of the switch the point B and C moves downward by  $4.4\mu\text{m}$  and  $0.5\mu\text{m}$  respectively. This makes a gap of  $1.6\mu\text{m}$  in one end and  $5.5\mu\text{m}$  in the other end of the driving electrode. For this design the gap of  $1.6\mu\text{m}$  and driving voltage of  $120\text{V}$  may leads to arc due to breakdown voltage and breakdown electric field.

### 6.4 Switching Characteristics of a Micromechanical Switch

In order to obtain the switching characteristics, the micromechanical switch designed in section 6.2 has been connected to an equivalent electrical circuit. Simulation has been carried out using MEMS+ interfaced with Cadence virtuoso and the schematic is shown in Figure 6.12.

A DC source of  $12\text{V}$  is connected to the anode of the micromechanical switch through a resistance of  $10\Omega$ . The load resistance of  $50\Omega$  is connected to cathode through an inductance of  $20\mu\text{H}$ . The DC voltage of  $48\text{V}$  is provided across the driving electrodes. Resistive and capacitive snubbers are used to reduce the voltage and current peaks during switching.

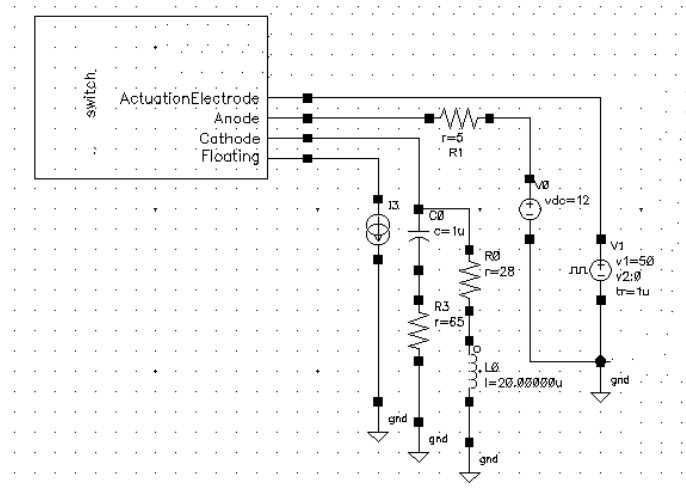
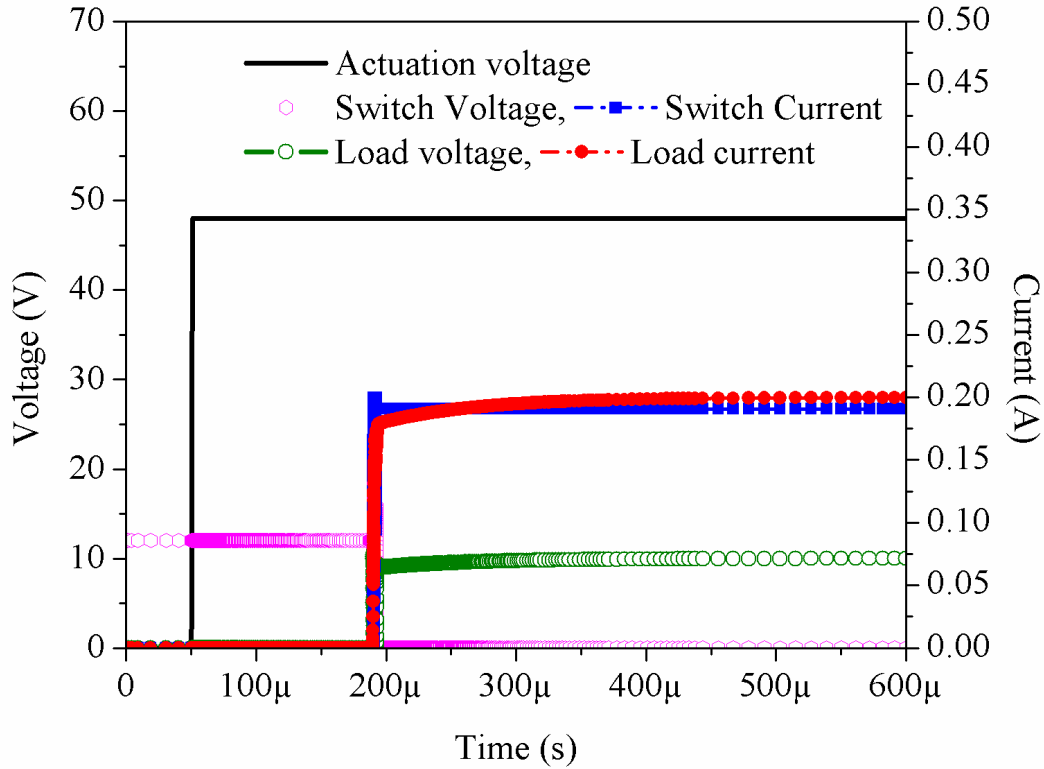


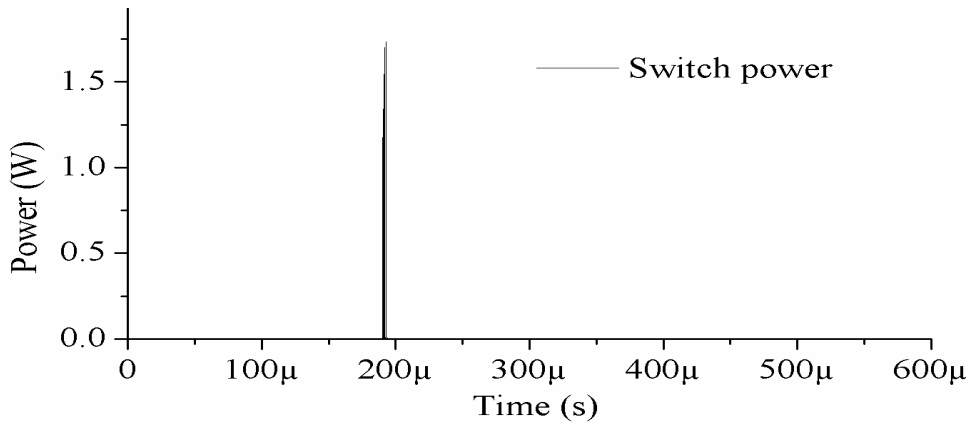
**Figure 6.12:** Schematic of equivalent DC electrical system with the micromechanical switch

### 6.4.1 Transition of switch from OFF-state to ON-state

The transient voltage, current, power characteristics are obtained, when the micromechanical switch changes from OFF-state to ON-state. The simulation has been carried out for the time period of  $0\mu\text{s}$  to  $600\mu\text{s}$ .



(a)



(b)

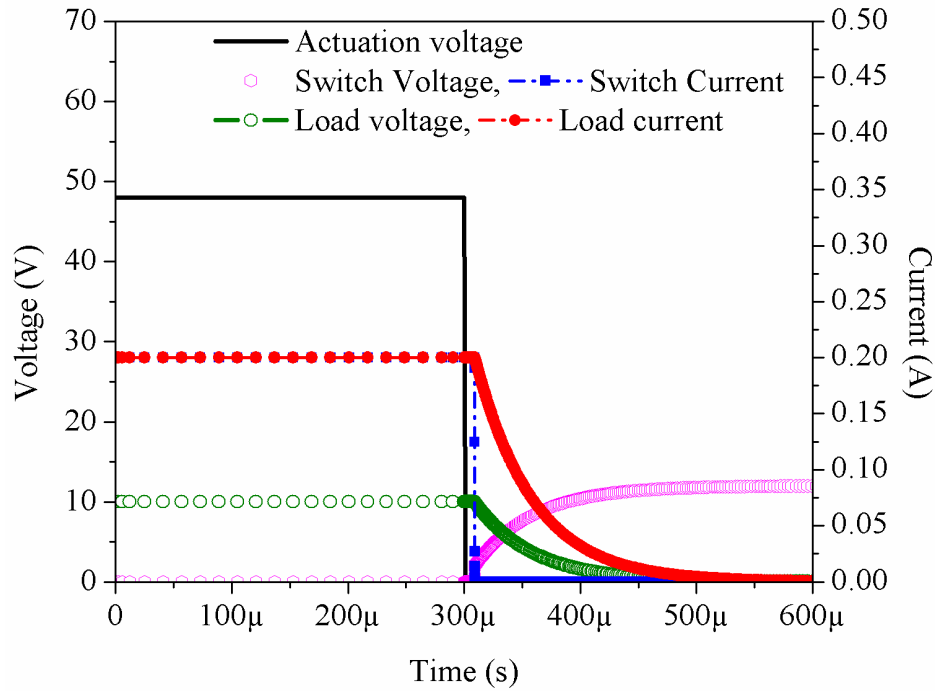
**Figure 6.13:** Transient switching from OFF-state to ON-state characteristics under load condition (a) Voltage and current (b) Power



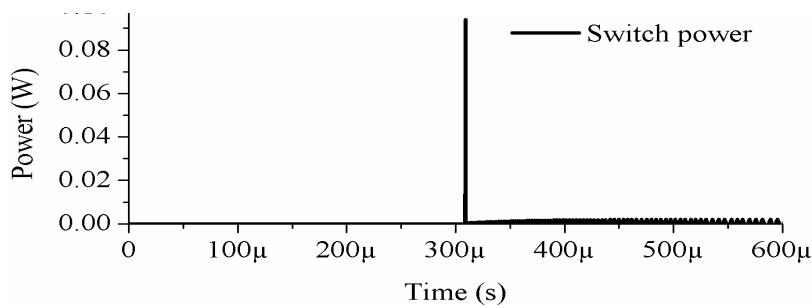
Driving voltage of 48V is applied across the driving electrode at 50 $\mu$ s and the current and voltage with respect to time is shown in Figure 6.13(a). The current through the switch increases and reaches 0.2A at 190 $\mu$ s. At the same time the voltage across the switch decreases from 12V to 0V. The delay time of 140 $\mu$ s is obtained. In this, the switching speed of the micromechanical switch is 120 $\mu$ s as discussed in section 6.2.4 and additional 20 $\mu$ s delay are due to circuit parameters. The switch becomes ON-state at 190 $\mu$ s and the load voltage and current increases to 12V and 0.2A respectively. This shows that the load is connected to the source through the micromechanical switch. The ON-state open loss and OFF-state open isolation losses are observed as 0W. During the switching time both switch voltage and switch current appears across the micromechanical switch and causes power loss of 1.75W and is shown in Figure 6.13(b). This power loss during switching time obtained is in agreement with the conceptual model simulation discussed in section 3.2.4, chapter 3.

#### **6.4.2 Transition of switch from ON-state to OFF-state**

The transient voltage, current, power characteristics are obtained, when the micromechanical switch changes from ON-state to OFF-state. The simulation has been carried out for the time period of 0 $\mu$ s to 600 $\mu$ s. The applied driving voltage is reduced from 48V to 0V at 300 $\mu$ s and is shown in Figure 6.14(a). The switch current decreases from 0.2A and reaches 0A at 450 $\mu$ s. At the same time the switch voltage increases from 0V to 12V. The delay time of 150 $\mu$ s is observed. In this the switching speed of the micromechanical switch is 120 $\mu$ s as discusses in section 6.2.4 and additional 10 $\mu$ s delay are due to load circuit parameters. The switch becomes OFF-state at 450 $\mu$ s and the load voltage and current deduces to 0V and 0A respectively. This shows that the load is completely isolated from the source due to the micromechanical switching. The ON-state open loss and OFF-state open isolation losses are observed as 0W and 0.002W. .During the switching time both the switch voltage and switch current appears across the micromechanical switch and causes power loss of 0.09W and is shown in Figure 6.14(b). This power loss during switching time obtained is in agreement with the conceptual model simulation discussed in section 3.2.4, chapter 3.



(a)



(b)

**Figure 6.14:** Transient switching from ON-state to OFF-state characteristics under load condition (a) Voltage and current (b) Power

### 6.5 Arcless Switching of Micromechanical Switch

Contact welding and arc are two important failure modes which cause reliability issues. Contact welding occurs in the microelectrical contact during ON-state. In micromechanical switch, arc may occur across driving electrodes, microelectrical contact, across anode-cathode gap and gap between anode-driving electrodes. Arc across driving electrode is discussed in chapter 4. Arc in the microelectrical contact is discussed in

chapter 5. The arcless nature of the designed micromechanical switch is discussed as follows.

### **6.5.1 Arc analysis for the gap between driving electrodes**

While performing switching action, the driving electrodes of the micromechanical switch won't touch each other. Hence, there is a gap between driving electrodes during ON-state and OFF-state. Breakdown arc occurs across the driving electrode, when the voltage across the microgap is above breakdown voltage. If the electric field across the microgap is above the breakdown electric field then arc may occur due to ionization of air. This has been extensively discussed in chapter 4.

For the switch designed in this chapter, gap of  $6\mu\text{m}$  appears across the driving electrodes during OFF-state. The driving voltage of 48V is applied across the driving electrode at  $100\mu\text{s}$  as shown in Figure 6.5. Hence the 48V is applied across uniform gap of  $6\mu\text{m}$ . According to modified Paschen curve discussed in chapter 4, the gold electrode with  $6\mu\text{m}$  can withstand 350V without producing arc. Hence 48V may not lead to arc. At  $230\mu\text{s}$ , the switch becomes ON-state. At this time point B and C moves downward by  $4.5\mu\text{m}$  and  $1.25\mu\text{m}$  respectively. This leads to non-uniform gap. The gaps between the driving electrodes are  $1.5\mu\text{m}$  ( $g_{d1}$ ) and  $4.75\mu\text{m}$  ( $g_{d2}$ ) at point B and C respectively. As discussed in chapter 4, for the worst case boundary arc analysis in  $1.25\mu\text{m}$  gap is at point B has to be analyzed. According to modified Paschen curve discussed in chapter 4, the gold electrode with  $1.25\mu\text{m}$  can withstand 85V without producing arc. Hence this design is free from breakdown arc. When 48V is applied across the driving electrodes, the electric field of  $5.87e^6$  V/m and  $1.95e^7$  V/m is produced during OFF-state and ON-state respectively. These electric fields are also below the breakdown electric field discussed in chapter 4. Hence the driving electrode won't cause breakdown arc during ON-state and OFF-state of the micromechanical switch.

### **6.5.2 Arc analysis for the microelectrical contact**

The maximum current appearing across the microelectrical contact during ON-state is 0.2A. As discussed in Figure 5.14 section 5.3.5, chapter 5, the microelectrical contact with gold (Au) reaches softening temperature at 0.2A and melting temperature at 0.47A. Since the microelectrical contact of the switch is not reaching the softening temperature, there is no chance of deformation in the structure and resistance of the microelectrical

contact. Under such condition contact welding will not occur. The failure mechanism of contact welding won't occur in this design and the design is reliable.

In the microelectrical contact arc occurs during switching time as discussed in chapter 5. At the time of switching from OFF-state to ON-state, the power appears across the microelectrical contact increases the temperature. If this reaches the melting temperature, then molten metal bridge may form. If the temperature reaches boiling temperature, the metal gets vaporized and leads to arc. This arc is called pre-breakdown arc. Figure 6.13(b) shows that maximum power across the switch is 1.75W. This power appears for 100ns. As discussed in chapter 5, section 5.4.2, and the power of 1.75W need  $2\mu\text{s}$  to reach its softening temperature and  $7\mu\text{s}$  to reach its melting temperature. Since 100ns is not sufficient to reach the softening temperature, structural deformation of the microelectrical contact may not occur. Also since the switch is not reaching its melting temperature, breakdown arc may not occur.

Figure 6.14(b) shows that, when switching from ON-state to OFF-state, maximum power across the switch is 0.09W. This power appears for 100ns. As discussed in chapter 5, section 5.4.2, and the power of 0.098W is not sufficient to reach even softening temperature and also this power appears only for 100ns. Since this power is not sufficient to reach the softening temperature, structural deformation of the microelectrical contact may not occur. Also since the switch is not reaching its melting temperature, pre-breakdown arc won't occur.

From this it is clear that the designed micromechanical switch won't generate any arc during the time of switching. But these designed micromechanical switches have low voltage, current and power rating. In general the time for which power appears across the microelectrical contact depends on the switching speed. If the switching speed is high, then the power appears across the contact for less time and if the switching speed is low, power appears for longer duration. Hence the switching speed of the microelectrical contact plays an important role in the design of arcless microelectrical contact.

### **6.5.3 Arc analysis for the gap between anode and cathode**

The gap between anode and cathode is fixed. As discussed in chapter 5, breakdown Arc may occur between anode and cathode during OFF-state of the micromechanical contact. For the considered design the gap between anode and cathode is  $5\mu\text{m}$  and the rating of

12V is considered. According to modified passion curve discussed in chapter 4, the gold plate with 5 $\mu$ m gap can withstand 300V without arcing. At 12V the designed anode and cathode produces electricfield of  $1.7e^6$  V/m. Since the electric field produced by 12V is well below the breakdown electric field, breakdown arc won't occures across anode and cathode.

#### **6.5.4 Arc analysis for the gap between driving electrodes and anode**

In microelectrical contact, driving voltage of 48V is applied across the driving electrodes. During OFF-state of the switch, the voltage of 12V is appearing across anode and cathode. This leads to a voltage difference of 36V across anode and driving electrode. The gap between driving electrode and anode is 105 $\mu$ m. Hence, in this design, 38V won't produce any arc due to voltage and electric field.

### **6.6 Switching Characteristics of Scalable TCT Array of**

#### **Micromechanical Switches**

In order to enhance higher power rating, the designed arcless, low rating micromechanical switches are connected in TCT array configuration as discussed in the conceptual model proposed in chapter 3. The series connection of switches increases the voltage rating and the current rating is increased by parallel connection of switches. To increase the overall reliability of the array, these switches are cross tied with each other. Hence, failure of single won't affect the performance of entire array. By connecting more switches in series and parallel, this array can be scalable to the required rating. In this design, the driving voltage is applied to all the switches at the same time to perform switching operation simultaneously.

A TCT array configuration is formed using designed, arcless micromechanical switches of rating 12V, 0.2A and is shown in Figure 6.15. The 15x12 switch array has been designed for the rating of 140V, 3A. In order to obtain the switching characteristics of the array, this TCT array configuration is connected with the equivalent electrical system as shown in Figure 6.16.

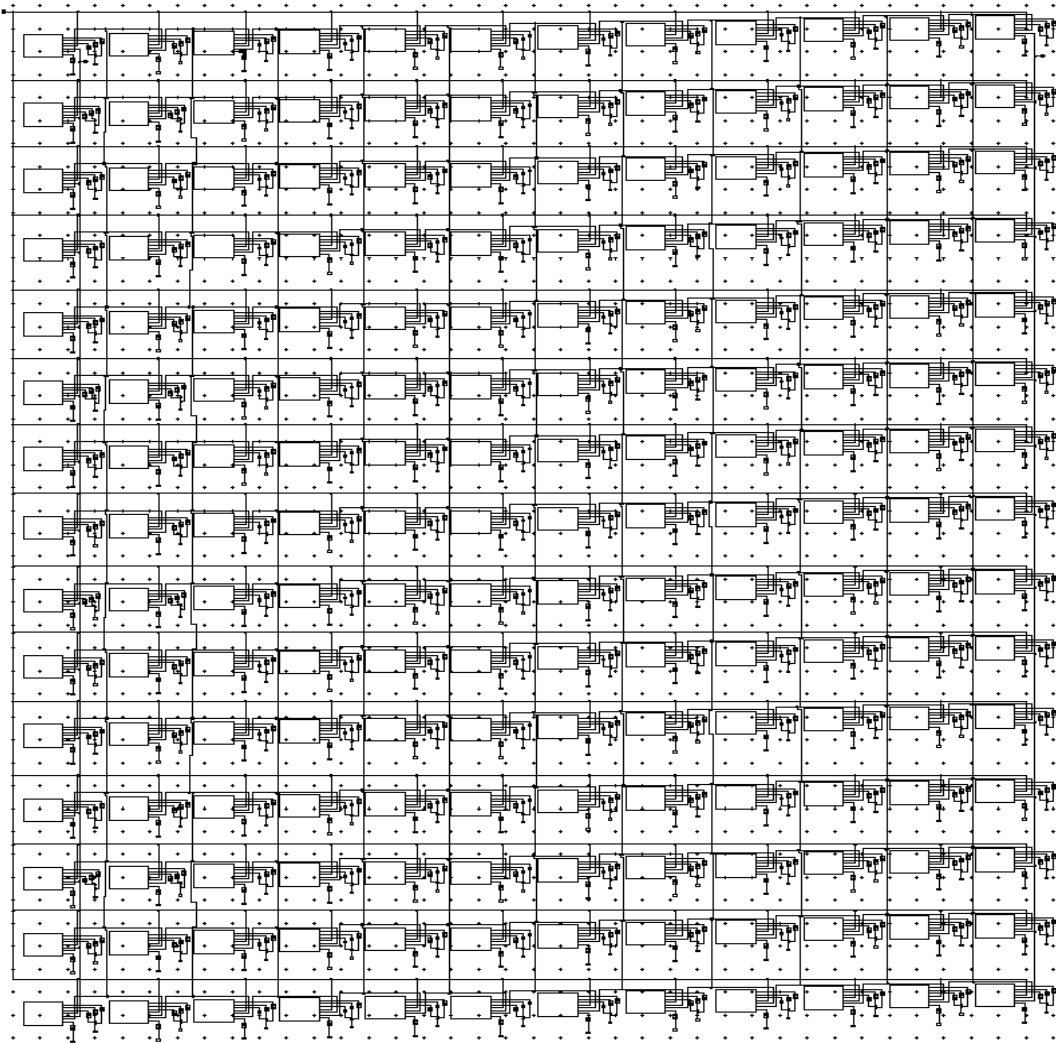


Figure 6.15: Schematic of TCT array of  $15 \times 12$  micromechanical switches

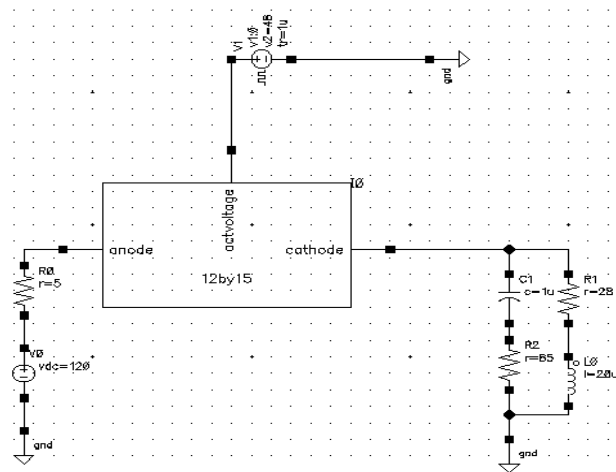
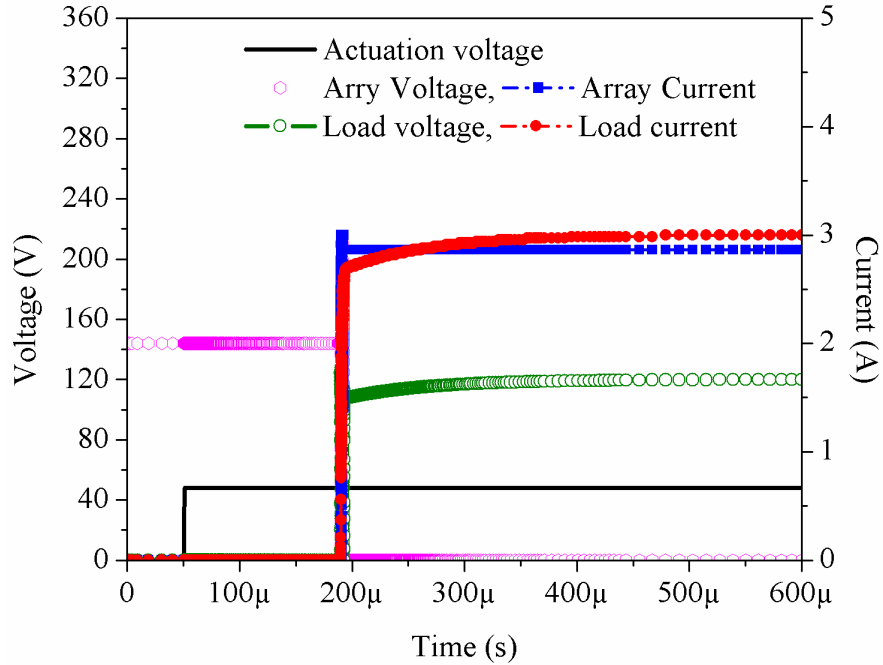


Figure 6.16: Electrical circuit with micromechanical switch array

### 6.6.1 Transition of TCT array from OFF-state to ON-state

Transient voltage, current, power characteristics are obtained, when the TCT array changes from OFF-state to ON-state. The simulation also has been carried out for the time period of  $0\mu\text{s}$  to  $600\mu\text{s}$ . Driving voltage of  $48\text{V}$  is applied across the driving electrodes of all the micromechanical switches in the TCT array at  $50\mu\text{s}$  and is shown in Figure 6.17.



**Figure 6.17:** Transient switching of array from OFF-state to ON-state under load condition

The array current increases and reaches  $3\text{A}$  at  $190\mu\text{s}$ . At the same time the array voltage decreases from  $140\text{V}$  to  $0\text{V}$ . The delay time of  $140\mu\text{s}$  is obtained. The switching speed of the micromechanical switch is obtained as  $120\mu\text{s}$  as discussed in section 6.2.4 and additional  $20\mu\text{s}$  delay are due to circuit parameters. The array becomes ON-state at  $190\mu\text{s}$  and the load voltage and current increases to  $140\text{V}$  and  $3\text{A}$  respectively. This shows that the load is connected to the source through the TCT array of micromechanical switches. The maximum voltage, current and power handled by a single micromechanical switch of the array is  $12\text{V}$ ,  $0.2\text{A}$  and  $1.75\text{W}$  respectively. Since the single switch is arcless, the TCT array configuration also enhances arcless switching.

### 6.6.2 Transition of TCT array from ON-state to OFF-state

Transient voltage, current, power characteristics are obtained, when the TCT array changes from ON-state to OFF-state. The simulation has been carried out for the time

period of  $0\mu\text{s}$  to  $600\mu\text{s}$ . The applied driving voltage of  $48\text{V}$  is reduced to  $0\text{V}$  at  $300\mu\text{s}$  for all the switches present in the TCT array and is shown in Figure 6.18.

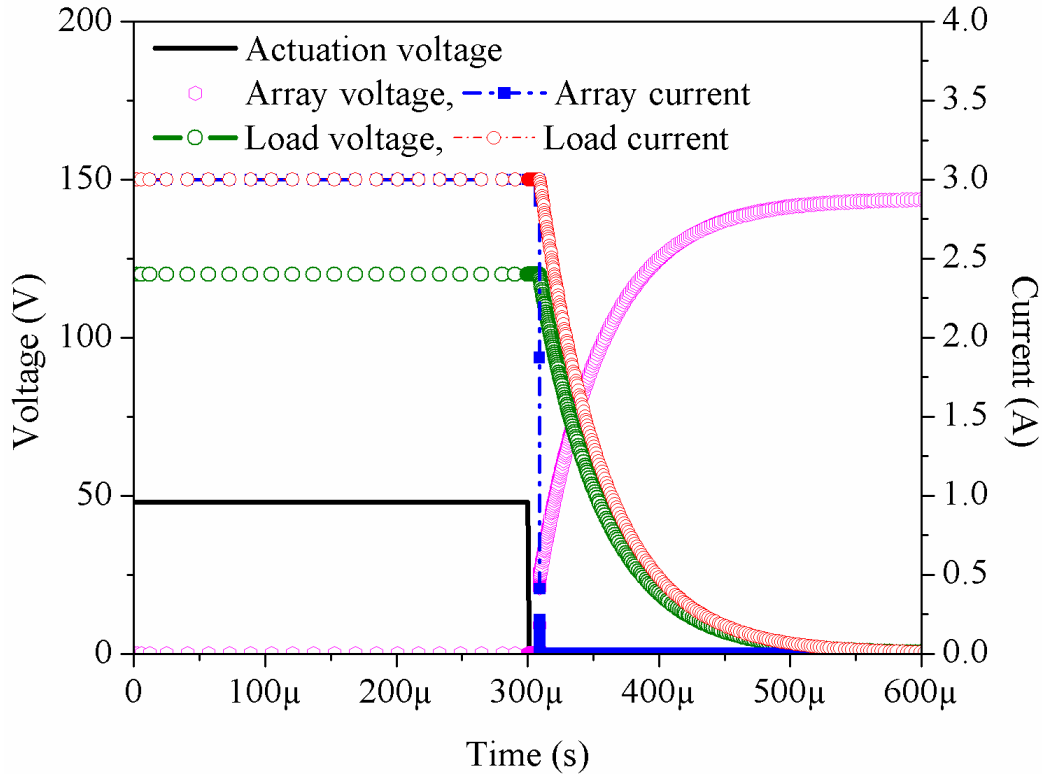


**Figure 6.18:** Transient switching of array from ON-state to OFF-state under load condition

The array current decreases from  $3\text{A}$  and reaches  $0\text{A}$  at  $450\mu\text{s}$ . At the same time the array voltage increases from  $0\text{V}$  to  $12\text{V}$ . The delay time of  $150\mu\text{s}$  is observed. In this the switching speed of the micromechanical switch is  $120\mu\text{s}$  as discussed in section 6.2.4 and  $10\mu\text{s}$  delay are due to circuit parameters. The switch becomes OFF-state at  $450\mu\text{s}$  and the load voltage and current reaches  $0\text{V}$  and  $0\text{A}$  respectively. This shows that the load is completely isolated from the source through TCT array of micromechanical switches. The maximum voltage, current and power handled by each switch is  $12\text{V}$ ,  $3\text{A}$  and  $0.09\text{W}$ .

### 6.6.3 Resistance of TCT array of micromechanical switches

The resistance of micromechanical switch is the resistance of the microelectrical contact. The dimensions of the microelectrical contact mentioned in this chapter are similar to the one in chapter 5. Hence resistance of each micromechanical switch is  $120\text{m}\Omega$  when  $120\mu\text{N}$  force is applied across the contact. The calculated resistance of the TCT array is



96mΩ. In the TCT array configuration, it is preferred to keep more number of parallel switches than number of series switches. This reduces the overall resistance of the array and leads to less power losses. Connecting more number of series switches than parallel switches increases the overall resistance and power loss. This increases the temperature of the array and may leads to reliability issues.

#### 6.6.4 Scalability

Based on the required voltage and current rating, more number of micromechanical switches can be connected in TCT array configuration. 150×12 switches can be connected to enhance the rating of 140V, 30A and 5×4 switches can be connected to enhance the rating of 48V, 1A.

The Comparison of presented switch with mechanical, semiconductor and RF switch have been given in Table 6.5.

**Table 6.5:** Comparison of micromechanical switch with mechanical, semiconductor and RF switches

	<b>Mechanical switch</b>	<b>Semiconductor Switches</b>	<b>RF MEMS</b>	<b>Micromechanical switch for power application</b>
<b>ON-state resistance</b>	Medium	High	Medium	Very low
<b>OFF-state isolation</b>	High	Low	High	High
<b>Contact</b>	Metal	PN junction	Ohmic or dielectric	Metal
<b>Frequency range</b>	Dc to 67GHz	Dc to 90GHz	Dc to 40GHz	DC
<b>Switching speed</b>	Slow	Very fast	Fast	Fast
<b>Insertion loss</b>	Low	High	Low	Low
<b>Power handling</b>	High	Low	Medium	Medium
<b>Power consumption</b>	Low	High	Low	Low
<b>Size</b>	Large	Small	Small	Small
<b>Linearity</b>	Excellent	Fair	Excellent	Excellent
<b>Scalability</b>	Fair	Good	Excellent	Excellent

## 6.7 Conclusion

This chapter presented the modeling, design and analysis of arcless micromechanical switch array and following are the main conclusions:

- The electromechanical parameters which have more influence on the design of micromechanical switch have been presented. In order to obtain the electromechanical performance parameters and visualize the switching action, the switch has been modeled following the fabrication flow using Coventorware MEMS+ simulation tool. The proposed fabrication flow uses poly-silicon as cantilever beam and the driving electrode and microelectrical contact are made up of metals such Al, Cu, Au and Pt.
- For the considered micromechanical switch with poly-silicon beam and Au as contact material, actuation voltage of 38.8V, collapse voltage of 60V, electrostatic force of 11.5 $\mu$ N, switching speed of 120 $\mu$ s and Q factor of 0.9 has been obtained from numerical calculation and simulation. It has been found that the poly-silicon beam has more influence on the electromechanical performance. Also it has been found that the electromechanical performance parameters are less affected by the driving electrode and microelectrical contact material.
- The switching speed and force with respect to driving voltage across the driving electrode shows that when voltage increases from 40V to 60V the switching speed increases from 118 $\mu$ s to 78 $\mu$ s and the electrostatic force increases from 13.2 $\mu$ N to 91.53 $\mu$ N. At the same time the contact force varies from 61.2 $\mu$ N to 197.8 $\mu$ N.
- The load handling capability of the switch and switching characteristics has been obtained using an electrical equivalent load circuit having RLC parameters. The current flowing through the switch, voltage across the switch, power appears across the switch, load voltage and load current are obtained. Maximum current of 0.2A and voltage of 12V are obtained across the switch during ON-state and OFF-state respectively. The power of 1.8W and 0.09W appears across the switch during switching time of OFF to ON and ON to OFF respectively.
- Arc analysis has been carried out for all four possible arc occurring parts of the microelectrical contact. The arcless nature of the micromechanical switch has

- been discussed. This analysis shows that the considered micromechanical switch withstands 12V, 0.2A without occurrence of arc. The load current and load voltage characteristics shows that the micromechanical switch is performing proper switching action so that it can be used to make and interrupt the current flow between source and load. The 12V causes the electric field of  $1.7e^6$  V/m. When 48V is applied across the driving electrodes, the electric field of  $5.87e^6$  V/m and  $1.95e^7$  V/m has been obtained during OFF-state and ON-state respectively.
- The importance of Q factor and the range at which the switch to be designed has been discussed. Two switches with Q factor of 0.052 and 23 have been designed and the performance parameters are obtained. The micromechanical switch with the Q factor of 0.052 leads to beam deformation. The switch with the Q factor of 23 leads to under damped oscillations. The importance of keeping Q factor within the range has been discussed. This analysis would help us to design reliable switch without oscillation and deformation.
  - 140V, 3A array has been designed using 12V, 0.2A micromechanical switches connected in 15×12 TCT array configuration. The switching characteristics of TCT array have been obtained. The resistance of the array has been obtained as 96mΩ. Scalability and arcless nature of the TCT array have been discussed. Since the single switch does not generate arc, the TCT array also can not generate arc.

# CHAPTER 7

## CONCLUSIONS AND SCOPE FOR FUTURE WORK

### 7.1 Conclusions

The significant conclusions made in the present work are as follows:

- The conceptual modeling and simulation concluded that the TCT cross tied array configuration provides better performance in terms of OFF-state leakage current, ON-state voltage drop and power losses. This array is suitable for both DC and AC power switching. This array is scalable to enhance higher voltage and current rating. The switching behavior and power appearing across the switch during switching period has been discussed. The study of various micromechanical switches concludes that the cantilever based, electrostatically actuated micromechanical switch is more suitable for power switching applications. The driving electrode and microelectrical contact are responsible for performing switching action and interrupting electric current. It is also concluded that arc occurs across four parts of the micromechanical switches. These are driving electrode, microelectrical contact, anode-cathode and anode-driving electrode.
- The modified Paschen curve provided the breakdown voltage and breakdown electric field for the materials Al, Cu, Au and Pt from gap of  $0.5\mu\text{m}$  to  $30\mu\text{m}$ . It has been found that larger the size of the driving electrode lesser the electric field for a given voltage. Hence both voltage and electric field should be analyzed. It has been concluded that both voltage and electric field appearing across the driving electrode has to be below the modified Paschen curve boundary in order to achieve arcless driving electrodes. In addition to this, it has been concluded that during the OFF-state of the micromechanical switch, occurrence of arc should be analyzed with respect to the smaller gap of the microelectrical contact.
- The surface roughness of the microelectrical contact has major influence on the ON-state resistance and current carrying capability. The electrothermal analysis showed that the temperature produced by the current should be below the softening temperature so that contact welding can be avoided. And also pre-

breakdown arc occurs during switching state and can be avoided if the temperature is below the melting temperature. The breakdown arc that occurs between anode and cathode can be avoided by limiting the voltage and electric field below the breakdown voltage and breakdown electric field.

- The performance parameters such as actuation voltage, collapse voltage, switching speed and Q factor of the arcless micromechanical switches are investigated extensively. The load switching characteristics are obtained and the influence of switching speed on the design of arcless switching has been investigated. The TCT array of micromechanical switch has been proposed to enhance the higher rating with reduced ON-state resistance. Also it has been concluded that the Q factor should be maintained within the range to achieve reliable arcless switching.

## **7.2 Contributions of the Thesis**

The main contributions of this thesis are described below:

### ***TCT array configuration of micromechanical switches for power switching:***

The conceptual model of TCT array configuration of micromechanical switches has been built based on literature for power switching applications and simulation has been carried out to understand the physical structure and performance of the array. This conceptual model results gives the confidence to proceed further for the design of arcless micromechanical switches.

### ***Design of arcless driving electrode using mathematical modeling and FEM simulation:***

Understanding the distribution of electric field is the basic requirement in designing arcless driving electrodes. The mathematical modeling gives the maximum electric field obtained and the FEM simulation study presents the maximum electric field and how it has been distributed across the driving electrodes. This prediction of electric field distribution can be useful in designing arcless non-touching contacts present in microstructures.

***Design of microelectrical contact through electrothermal analysis, mathematical modeling and FEM simulation:***

Electrothermal analysis is important in designing the arcless microelectrical contact. In order to prevent contact welding and to achieve arcless switching, electrothermal analysis has been carried out. The importance of both electrical and thermal parameters in the design of arcless microelectrical contact has been extensively explored using mathematical modeling and FEM simulations.

***Design and analysis of arcless micromechanical switch:***

The micromechanical switch has been designed and the electromechanical parameters have been analyzed in detail. The electrical and mechanical parameters have sufficient influence on the design of arcless switching. The switching characteristics along with external load circuit have been analyzed. The performances of the TCT array of micromechanical switch have been analyzed to evaluate the performance of the micromechanical switch array for high voltage and current rating.

### **7.3 Scope for Future Work**

This thesis work has few limitations that warrant further research.

- This work can be extended to enhance the reliability of micromechanical switch considering fabricatability, manufacturability, material, packaging and operating environmental conditions. After the extensive reliability study, the switch can be fabricated and characterization may be carried out.
- The leakage current analysis can be carried out and the improvement in battery life can be analyzed.
- This work also can be extended to investigate better materials which can withstand high voltage and current without arc and thus leading to low power consumption.
- This work can be further extended to design CMOS fabrication compatible arcless micromechanical switches and investigate their usage for SoC, clock gating and power gating circuits.

## REFERENCES

ABB STOTZ-KONTAKT (2011) *Miniature circuit breaker S 200 S*. Available at: <https://library.e.abb.com/public/1c8e6454c74f56cfc125795a0036e740/2CDC002137D0201.pdf> (Accessed: 9 July 2016).

Abou-Seada, M.S. (1984) 'Calculation of high-frequency breakdown voltages of point-to-plane air gaps', *IEEE Transactions on Industry Applications*, IA-20(6), pp. 1627–1630.

Advameg (2016) *Electromagnetically actuated switches patent application class*. Available at: <http://www.patentsencyclopedia.com/class/000492377> (Accessed: 28 June 2016).

Amir Khan, U., Lee, J.-G., Amir, F. and Lee, B.-W. (2015) 'A novel model of HVDC hybrid-type Superconducting circuit breaker and its performance analysis for limiting and breaking DC fault currents', *IEEE Transactions on Applied Superconductivity*, 25(6), pp. 1–9.

Ammerman, R.F., Gammon, T., Sen, P.K. and Nelson, J.P. (2010) 'DC-Arc models and incident-energy calculations', *IEEE Transactions on Industry Applications*, 46(5), pp. 1810–1819.

Andronachi, C.-C. and Istrate, D.-M. (2015) 'Design and simulation of a network for testing a shunt switch', *Proceedings of 6<sup>th</sup> International Conference on Modern Power System*, pp. 5-9.

ANSYS (2016) *Simulation driven product development*. Available at: <http://www.ansys.com/> (Accessed: 28 June 2016).

Arnaud, J. and Branco, P.J.C. (2016) 'Electrothermal characteristics of YBCO bulk magnets deep in LN<sub>2</sub>: A preliminary analysis for its use as Excitation system of low-speed synchronous generators', *IEEE Transactions on Applied Superconductivity*, 26(3), pp. 1–8.

Aronstein, J. and Hare, T.K. (2005) ‘AC and DC electromigration failure of aluminum contact junctions’, *IEEE Transactions on Components and Packaging Technologies*, 28(4), pp. 701–709.

Atalla, M.M. (1953) ‘Arcing of electrical contacts in telephone switching circuits’, *Bell System Technical Journal*, 32(5), pp. 1231–1244.

Atmadji, A.M.S. and Sloot, J.G.J. (1998) ‘Hybrid switching: A review of current literature’, *Proceedings of Energy Management and Power Delivery*, 2, pp. 683–688.

Bachman, M., Zhang, Y., Wang, M. and Li, G.. (2012) ‘High-power magnetically actuated microswitches fabricated in Laminates’, *IEEE Electron Device Letters*, 33(9), pp. 1309–1311.

Baek, J.W., Yoo, D.-W. and Kim, H.-G. (2001) ‘High-voltage switch using series-connected IGBTs with simple auxiliary circuit’, *IEEE Transactions on Industry Applications*, 37(6), pp. 1832–1839.

Baglio, S., Castorina, S. and Savalli, N. (2008) *Scaling issues and design of Microelectromechanical systems*. United States: Hoboken, New Jersey, U.S.A.: Wiley-Interscience.

Balachandra, T.C. and Nagabhushana, G.R. (1993) ‘Anode hotspot temperature estimation in vacuum gaps under 50 Hz alternating excitations’, *IEEE Transactions on Electrical Insulation*, 28(3), pp. 392–401.

Bastidas, R.J.D., Ramos, P.C.A. and Saavedra, M.A.J. (2013) ‘Reconfiguration analysis of photovoltaic arrays based on parameters estimation’, *Simulation Modelling Practice and Theory*, 35, pp. 50–68.

Basu, A., Hennessy, R., Adams, G. and McGruer, N. (2013a) ‘Leading and trailing edge hot switching damage in a metal contact RF MEMS switch’, *Proceedings of 17<sup>th</sup> International Conference on Solid-state sensors, Actuators and Microsystems*, pp. 514-517.



Basu, A., Hennessy, R., Adams, G. and McGruer, N. (2013b) 'Reliability in hot switched ruthenium on ruthenium MEMS contacts', *Proceedings of IEEE 59th Holm Conference on Electrical Contacts*, pp.1-8.

Basu, A., Hennessy, R.P., Adams, G.G. and McGruer, N.E. (2014) 'Hot switching damage mechanisms in MEMS contacts—evidence and understanding', *Journal of Micromechanics and Microengineering*, 24(10), p. 105004.

Batra, R.C., Porfiri, M. and Spinello, D. (2007) 'Review of modeling electrostatically actuated microelectromechanical systems', *Smart Materials and Structures*, 16(6), pp. R23–R31.

Batunlu, C. and Albarbar, A. (2016) 'Real-time system for monitoring the electro-thermal behaviour of power electronic devices used in boost converters', *Microelectronics Reliability*, 62, pp. 82–90.

Bell, W.J. (1991) 'Calhoun: The NPS institutional archive proposed model of thermionically assisted breakdown and implementation on electrostatic thrusters', *Monterey, California, Naval Postgraduate School*.

Bielinski, R.F., Jaeschke, J.R., Krstic, S., Piber, E.T., Theisen, P.J. and Corporation, E. (1985) *Patent US4642481 - solid state hybrid switch*.

Boudreaux, R.R. and Nelms, R.M. (1996) 'A comparison of MOSFETs, IGBTs, and MCTs for solid state circuit breakers', *Eleventh Annual Conference Proceedings of Applied Power Electronics Conference and Exposition*, pp. 227-233.

Boyle, W.S. and Kisliuk, P. (1955) 'Departure from Paschen's law of breakdown in gases', *Physical Review*, 97(2), pp. 255–259.

Burkes, T.R., Hagler, M.O., Kristiansen, M., Craig, J.P., Portnoy, W.M. and Kunhardt, E.E., (1978). *A critical analysis and assessment of high power switches*. Sothern Center for Electrical Engineering Education Inc St Cloud Fl.

Carslaw, H.S. and Jaeger, J.C.C. (1986) *Conduction of heat in solids*. 2<sup>nd</sup> edn. United Kingdom: Oxford University Press.

Chakraborty, S., Simoes, G.M. and Kramer, W.E. (2013) *Power electronics for renewable and distributed energy systems: A Sourcebook of Topologies, control and integration*. United States.

Chan, R., Lesnick, R., Becher, D. and Feng, M. (2003) ‘Low-actuation voltage RF MEMS shunt switch with cold switching lifetime of seven billion cycles’, *Journal of Microelectromechanical Systems*, 12(5), pp. 713–719.

Chen, C.-H., Yeh, J.A. and Wang, P.-J. (2006) ‘Electrical breakdown phenomena for devices with micron separations’, *Journal of Micromechanics and Microengineering*, 16(7), pp. 1366–1373.

COMSOL Inc (2014) *Multiphysics simulation software - platform for physics-based modeling*. Available at: <https://www.comsol.co.in/comsol-multiphysics>. (Accessed: 12 June 2016).

Cook, C.K.A., Thambi, N. and Sastry, A.M. (2008) ‘Powering MEMS portable devices—a review of non-regenerative and regenerative power supply systems with special emphasis on piezoelectric energy harvesting systems’, *Smart Materials and Structures*, 17(4), p. 043001.

Coutu, R.A., Kladitis, P.E., Leedy, K.D. and Crane, R.L. (2004) ‘Selecting metal alloy electric contact materials for MEMS switches’, *Journal of Micromechanics and Microengineering*, 14(8), pp. 1157–1164.

Coutu, R.A., Kladitis, P.E., Starman, L.A. and Reid, J.R. (2004) ‘A comparison of micro-switch analytic, finite element, and experimental results’, *Sensors and Actuators A: Physical*, 115(2-3), pp. 252–258.

Coutu, R.A., Reid, J.R., Cortez, R., Strawser, R.E. and Kladitis, P.E. (2006) ‘Microswitches with sputtered Au, AuPd, Au-on-AuPt, and AuPtCu alloy electric

contacts', *IEEE Transactions on Components and Packaging Technologies*, 29(2), pp. 341–349.

Coventor Inc. (2016) *COVENTORWARE*. Available at: <http://www.coventor.com/mems-solutions/products/coventorware/>.(Accessed: 28 June 2016).

Czarnecki, N.A. and Corporation, R.C. (2013) *Patent US9054447 - electrical connector using air heated by an electrical arc during disengagement of contacts to extinguish the electrical arc*.

Dewey, A., Srinivasan, V. and Icoz, E. (2001) 'Visual modeling and design of microelectromechanical system transducers', *Microelectronics Journal*, 32(4), pp. 373–381.

Dryburgh, L., Hewitt, J. and Hewett, J. (2004) *Signaling system no. 7 (SS7/C7) no. 7: Protocol, architecture, and services*. United States: Cisco Press.

Dumas, N., Trigona, C., Pons, P., Latorre, L. and Nouet, P. (2011) 'Design of smart drivers for electrostatic MEMS switches', *Sensors and Actuators A: Physical*, 167(2), pp. 422–432.

Dummer, G.W.A.W. and Davies, E. (1997) *Electronic inventions and discoveries: Electronics from its earliest beginnings to the present day*. United Kingdom: Institute of Physics Publishing.

Eiser, S., Bernardoni, M., Nelhiebel, M. and Kaltenbacher, M. (2017) 'Finite-element analysis of coupled Electro-Thermal problems with strong scale separation', *IEEE Transactions on Power Electronics*, 32(1), pp. 561–570.

Ekwińska, M.A., Bieniek, T. and Janczyk, G. (2015) 'Specialized MEMS microphone for industrial application', in Jabłoński, R. and Brezina, T. (eds.) *Advanced Mechatronics Solutions*. Switzerland: Springer International Publishing, pp. 453–460.

*EN6555A D* (2013) Available at: [http://www.onsemi.com/pub\\_link/Collateral/EN6555A-D.PDF](http://www.onsemi.com/pub_link/Collateral/EN6555A-D.PDF) (Accessed: 9 July 2016).

Etal, H. (1967) *Solid State Switc*, 3339104.

General Electric (2016) *GE MEMS for LTE advanced mobile devices*. Available at: <http://www.geglobalresearch.com/news/press-releases/ge-mems-switch-technology-demonstrates-performance-meet-demands-next-generation-true-4g-mobile-devices>. (Accessed: 9 June 2016).

Go, D.B. and Pohlman, D.A. (2010) 'A mathematical model of the modified Paschen's curve for breakdown in microscale gaps', *Journal of Applied Physics*, 107(10), p. 103303.

Go, D.B. and Venkatraman, A. (2014) 'Microscale gas breakdown: Ion-enhanced field emission and the modified Paschen's curve', *Journal of Physics D: Applied Physics*, 47(50), p. 503001.

Goggin, R., Fitzgerald, P., Stenson, B., Carty, E. and McDaid, P. (2015) 'Commercialization of a reliable RF MEMS switch with integrated driver circuitry in a miniature QFN package for RF instrumentation applications', *Proceedings of IEEE MTT-S International Microwave Symposium*, pp.1-4.

Hajjaj, A.Z., Alcheikh, N., Ramini, A., Al Hafiz, M.A. and Younis, M.I. (2016) 'Highly tunable electrothermally and electrostatically actuated resonators', *Journal of Microelectromechanical Systems*, 25(3), pp. 440–449.

Hennessy, R.P., Basu, A., Adams, G.G. and McGruer, N.E. (2013) 'Hot-switched lifetime and damage characteristics of MEMS switch contacts', *Journal of Micromechanics and Microengineering*, 23(5), p. 055003.

Hiltmann, K., Schumacher, A., Guttman, K., Lemp, E., Sandmaier, H. and Lang, W. (2002) 'New micromachined membrane switches in silicon technology', *IEEE Transactions on Components and Packaging Technologies*, 25(3), pp. 397–401.

Holm, R. (2000) *Electric Contacts: Theory and Application*. Berlin, Springer-verlog.

Hsu, T.-R. (2002) *Miniaturization – A paradigm shift in advanced manufacturing and education*, Available at: <http://www.engr.sjsu.edu/trhsu/Miniaturization%20.pdf> (Accessed: 9 June 2016).

Huang, D.F., Jou, H.L., Wu, J.C., Wu, K.D. and Huang, J.-J. (2015) ‘Multi-level DC power distribution interface for data centers’, *Proceedings of IEEE International Conference on Smart City/SocialCom/SustainCom together with DataCom*, pp. 878–881.

Hwang, S.Y., Lee, J.H., Visuwanathan, K.K. and Ban, I.H. (2013) ‘Experiments and thermal-electrical analysis of buss bar and relay assemblies in junction blocks’, *International Journal of Automotive Technology*, 14(1), pp. 79–90.

Hyman, D. and Mehregany, M. (1999) ‘Contact physics of gold microcontacts for MEMS switches’, *IEEE Transactions on Components and Packaging Technologies*, 22(3), pp. 357–364.

*IRF730A pdf, IRF730A description, IRF730A datasheets, IRF730A view: ALLDATASHEET::* Available at: <http://pdf1.alldatasheet.com/datasheet-pdf/view/97869/IRF/IRF730A.html> (Accessed: 9 July 2016).

Jau, T.W. (2013) *RF MEMS switches: High-frequency performance and hot-switching reliability*, *High Frequency Electronics*, pp. 34-38.

Johnson, C. (2009) *Numerical solutions of partial differential equations by the finite element method*. United States: Dover Publications.

Kaiser, K.L. (2005) *Electromagnetic Compatibility Handbook*. CRC Press.

Kam, H., Chen, Y. and Liu, T.-J.K. (2013) ‘Reliable micro-electro-mechanical (MEM) switch design for ultra-low-power logic’, *Proceedings of IEEE Reliability Physics Symposium*, pp. 1–6.

Kanno, I. (2013) ‘Piezoelectric thin films for MEMS applications’, in *MEMS: Fundamental Technology and Applications*, Taylor & Francis, pp. 41–68.

Kapoor, R., Shukla, A. and Demetriades, G. (2012) 'State of art of power electronics in circuit breaker technology', *Proceedings of IEEE Energy Conversion Congress and Exposition*, pp. 615-622.

Kara, A., Kalenderli, Ö. and Mardikyan, K. (2006) 'Effect of dielectric barriers to the electric field of rod-plane air gap', *Proceedings of the COMSOL Users Conference*.

Karady, G.G. and Heydt, G.T. (2006) 'Novel concept for medium voltage circuit breakers using Microswitches', *IEEE Transactions on Power Delivery*, 21(1), pp. 536–537.

Karady, G.G., Heydt, G.T., Gel, E.S. and Hubele, N.F. (2005) 'The Utilization of Micromechanical Devices in a Power Circuit Breaker', in *Electric Power Components and Systems*, Taylor & Francis, pp. 1159–1174.

Keimel, C., Claydon, G., Li, B., Park, J.N. and Valdes, M.E. (2012) 'Microelectromechanical-Systems-Based switches for power applications', *IEEE Transactions on Industry Applications*, 48(4), pp. 1163–1169.

Khoshnoud, F. and de Silva, C.W. (2012) 'Recent advances in MEMS sensor technology-mechanical applications', *IEEE Instrumentation & Measurement Magazine*, 15(2), pp. 14–24.

Khushalani, D.G., Pande, R.S. and Patrikar, R.M. (2016) 'Fabrication and characterization of MEMS cantilever array for switching applications', *Microelectronic Engineering*, 157, pp. 78–82.

Khushalani, D.G., Pande, R.S. and Patrikar, R.M. (2016) 'Fabrication and characterization of MEMS cantilever array for switching applications', *Microelectronic Engineering*, 157, pp. 78–82.

Kim, J.-M., Lee, S., Baek, C.-W., Kwon, Y. and Kim, Y.-K. (2008) 'Cold- and hot-switching lifetime characterizations of ohmic-contact RF MEMS switches', *IEICE Electronics Express*, 5(11), pp. 418–423.

Kim, S.W., Kim, H.H., Hahn, S.C., Lee, B.Y., Park, K.Y., Shin, Y.J., Song, W.P., Kim, J.B. and Shin, I.H. (2002) ‘Coupled finite-element-analytic technique for prediction of temperature rise in power apparatus’, *IEEE Transactions on Magnetics*, 38(2), pp. 921–924.

Kuffel, J., Kuffel, P., Zaengl, W.S. and Kuffel, E. (2000) *High-voltage engineering: Fundamentals*, United Kingdom.

Lee, J.-G., Khan, U.A., Lee, H.-Y. and Lee, B.-W. (2016) ‘Impact of SFCL on the Four types of HVDC circuit breakers by simulation’, *IEEE Transactions on Applied Superconductivity*, 26(4), pp. 1–6.

Lee, R., Chiou, Y. and Chung, H. (2001) ‘Arc erosion behaviour of silver electric contacts in a single arc discharge across a static gap’, *IEE Proceedings - Science, Measurement and Technology*, 148(1), pp. 8–14.

Leus, V. and Elata, D. (2004) Available at: <http://citeseerx.ist.psu.edu/viewdoc/download;jsessionid=4211542EF1FBC1768AB5DDF70A308600?doi=10.1.1.454.9033&rep=rep1&type=pdf> (Accessed: 19 July 2016).

Leviton, C.M. (2016) *Switches*. Available at: [http://www.leviton.com/OA\\_HTML/SectionDisplay.jsp?section=37678](http://www.leviton.com/OA_HTML/SectionDisplay.jsp?section=37678) (Accessed: 28 June 2016).

Lewis, A.P., McBride, J.W. and Jiang, L. (2015) ‘Evolution of voltage transients during the switching of a MEMS relay with au/MWCNT contacts’, *IEEE Transactions on Components, Packaging and Manufacturing Technology*, 5(12), pp. 1747–1754.

Li Hongtao, L.H., Naiqiu, S., Li Ling, L.L. and Wu Xiaowen, W.X. (2013) ‘Numerical calculation of transient thermal characteristics in gas-insulated transmission lines’, *TELKOMNIKA (Telecommunication Computing Electronics and Control)*, 11(3), p. 425.

Li, J., Sumner, M., Thomas, D.W.P., Christopher, E. and Jia, K. (2015) ‘Non-contact Arc Study for DC power systems’, *Proceedings of 41<sup>st</sup> Annual IEEE Conference on Industrial Electronics*, pp. 005113-005117.

Li, L., Li, C., Feng, Y., Jing, N., Zheng-Yang, Z. and Fu-Chang, L. (2011) ‘Analysis of electrical contact temperature rise in spark gap switches with graphite electrodes’, *IEEE Transactions on Dielectrics and Electrical Insulation*, 18(4), pp. 1307–1313.

Li, N., Mao, J., Zhao, W.-S., Tang, M., Chen, W. and Yin, W.-Y. (2016) ‘Electrothermal Cosimulation of 3-D carbon-based heterogeneous Interconnects’, *IEEE Transactions on Components, Packaging and Manufacturing Technology*, 6(4), pp. 518–526.

Li, Y. and Jiang, Z. (eds.) (2008) ‘An Overview of Reliability and Failure Mode Analysis of Microelectromechanical Systems’, in *Handbook of Performability Engineering*, pp. 953–966.

Long, X., Liao, R. and Zhou, J. (2012) ‘Numerical simulation on electrical-thermal properties of Gallium-Nitride-Based light-emitting Diodes embedded in board’, *Advances in OptoElectronics*, pp. 1–6.

Lu, J., Menard, S., MEMS, R. and Société (2006) *Patent US8115576 - MEMS actuators and switches*.

Lu, Y., Ren, Q., Liu, T., Leung, S.L., Gau, V., Liao, J.C., Chan, C.L. and Wong, P.K. (2016) ‘Long-range electrothermal fluid motion in microfluidic systems’, *International Journal of Heat and Mass Transfer*, 98, pp. 341–349.

Ma, B., You, Z., Ruan, Y., Chang, S. and Zhang, G. (2016) ‘Electrostatically actuated MEMS relay arrays for high-power applications’, *Microsystem Technologies*, 22(4), pp. 911–920.

Mathúna, C.O., Wang, N., Kulkarni, S. and Roy, S. (2012) ‘Review of integrated magnetics for power supply on chip (PwrSoC)’, *IEEE Transactions on Power Electronics*, 27(11), pp. 4799–4816.

MathWorks, (1994) *Simulink - simulation and model-based design - MathWorks United Kingdom*. Available at: <http://in.mathworks.com/products/simulink/>. (Accessed: 12 June 2016).



McKillop, J., Inc, T.T. and Austin (2007) MEMS switch challenges, *Microwave Journal*, pp.1-3.

Meyer, C., Kowal, M. and De Doncker, R.W. (2006) ‘Circuit breaker concepts for future high-power DC-applications’, *Proceedings of 40<sup>th</sup> IAS Annual Meeting and conference on Industry Applications*. 2, pp. 860 – 866.

Meyer, J. and Rufer, A. (2006) ‘A DC hybrid circuit breaker with ultra-fast contact opening and integrated Gate-Commutated Thyristors (IGCTs)’, *IEEE Transactions on Power Delivery*, 21(2), pp. 646–651.

Michael\_Gedeon (2011) *Connector temperature rise*. Available at: <https://materion.com/~media/Files/PDFs/Alloy/Newsletters/Technical%20Tidbits/Issue%20No%2023-%20Connector%20Temperature%20Rise.pdf> (Accessed: 26 July 2016).

*MINIATURE CIRCUIT BREAKERS LSN UP TO 63 A (10 kA) 4 miniature circuit breakers 1-pole* (2006) Available at: [http://www.oez.com/uploads/oez/files/ks/3081-Z01-06\\_EN\\_PL.pdf](http://www.oez.com/uploads/oez/files/ks/3081-Z01-06_EN_PL.pdf) (Accessed: 9 July 2016).

Mohan, N., Undeland, T.M., Robbins, W.P. and Undel, T.M. (2003) *Power electronics: Converters, applications and design, media enhanced*. 3rd edn. United States: John Wiley and Sons.

Morel, R., Rival, M., Garcia, H., Miguet, P. and Gerin, M. (1991) *Patent US5210385 - low voltage circuit breaker with multiple contacts for high currents*.

Mu, J., Wang, L. and Hu, J. (2009) ‘Analysis and Design of Topological Structure for DC Solid-State Circuit Breaker’, *Proceedings of World Non-Grid-Connected Wind Power and Energy Conference*, pp.1-5.

Muley, C.A., Naveed, S.A. and Shingare, S.M. (2013) ‘Design Aspects of RF Switch’, *International Journal of Electrical and Electronics Engineering Research*, 3(1), pp. 135–140.

Mulloni, V., Iannacci, J., Bartali, R. and Michel, V. (2011) 'Gold-based thin multilayers for ohmic contacts in RF-MEMS switches', *Microsystem Technologies*, 18(7), pp.965-971.

Newman, H.S., Ebel, J.L., Judy, D. and Maciel, J. (2008) 'Lifetime measurements on a high-reliability RF-MEMS contact switch', *IEEE Microwave and Wireless Components Letters*, 18(2), pp. 100–102.

Niayesh, K., Niemeyer, L. and Fabian, J.H. (2006) 'Matrix combination of elementary switches: General considerations and application to MEMS relays', *Electrical Engineering*, 90(1), pp. 19–31.

Noel, J.G. (2016) 'Review of the properties of gold material for MEMS membrane applications', *IET Circuits, Devices & Systems*, 10(2), pp. 156–161.

Oberhammer, J. and Stemme, G. (2006) 'Active opening force and passive contact force electrostatic switches for soft metal contact materials', *Journal of Microelectromechanical Systems*, 15(5), pp. 1235–1242.

Okawa, M., Shioiri, T., Okubo, H. and Yanabu, S. (1988) 'Area effect on electric breakdown of copper and stainless steel electrodes in vacuum', *IEEE Transactions on Electrical Insulation*, 23(1), pp. 77–81.

Paice, D.A., Mattern, K.E. and Corp, W.E. (1984) *Patent US4618906 - hybrid solid state/mechanical switch with failure protection.*

Parent, A., Krust, A. and Lorenz, G. (2015) 'Efficient Nonlinear Simulink Models of MEMS Gyroscopes Generated With a Novel Model Order Reduction Method', *Proceedings of 18<sup>th</sup> International Conference on Solid-State Sensors, Actuators and Microsystems*, pp. 2184-2187.

Park, K., Kang, S., Kim, H.S., Baek, C. and Chung, T.K. (2012) 'Energy scavenging system utilising MEMS switch for power management', *Electronics Letters*, 48(15), p. 948.

Penec, F., Achkar, H., Peyrou, D., Plana, R. and Pons, P. (2007) *VERIFICATION OF CONTACT MODELING WITH COMSOL MULTIPHYSICS SOFTWARE*. Available at: <https://hal-univ-tlse3.archives-ouvertes.fr/hal-00180257/document> (Accessed: 16 September 2016).

Persano, A., Quaranta, F., Capoccia, G., Proietti, E., Lucibello, A., Marcelli, R., Bagolini, A., Iannacci, J., Taurino, A. and Siciliano, P. (2016) 'Influence of design and fabrication on RF performance of capacitive RF MEMS switches', *Microsystem Technologies*, 22(7), pp. 1741-1746.

Radant MEMS (2003) *Radant MEMS*. Available at: <http://www.radantmems.com/radantmems/index.html> (Accessed: 29 June 2016).

Rashid, M.H. (1993) *Power electronics: Circuits, devices, and applications*. 2nd edn. London: Prentice-Hall International.

Raychowdhury, A., Kim, J.I., Peroulis, D. and Roy, K. (2013) 'Integrated MEMS switches for leakage control of battery operated systems', *Proceedings of IEEE Custom Intergrated Circuits Conference*, pp. 457–460.

Raychowdhury, A., Kim, J.I., Peroulis, D. and Roy, K. (2013) 'Integrated MEMS switches for leakage control of battery operated systems', *Proceedings of IEEE Custom Integrated Circuits Conference*, pp. 457–460.

Rebeiz, G.M. (2003) *RF MEMS: Theory, design, and technology*. United States: Wiley-Interscience.

Rebeiz, G.M., Patel, C.D., Han, S.K., Ko, C.-H. and Ho, K.M.J. (2013) 'The search for a reliable MEMS switch', *IEEE Microwave Magazine*, 14(1), pp. 57–67.

Ruan, J., Nohier, N., Baffleur, M., Bary, L., Coccetti, F., Lisec, T. and Plana, R. (2016) 'Electrostatic discharge failure analysis of capacitive RF MEMS switches', *Microelectronics Reliability*, 47(s 9–11), pp. 1818–1822.

Rumbach, P. and Go, D.B. (2012) 'Fundamental properties of field emission-driven direct current microdischarges', *Journal of Applied Physics*, 112(10), p. 103302.

Saeedifard, M., Graovac, M., Dias, R.F. and Iravani, R. (2010) 'DC power systems: Challenges and opportunities', *IEEE PES General Meeting*, pp. 1–7.

Sawa, K., Tsuruoka, M. and Morii, M. (2014) 'Fundamental characteristics of arc extinction by magnetic blow-out at DC voltages (<500V)', *Proceedings of 60<sup>th</sup> IEEE Holm Conference on Electrical Contacts Conference*, pp. 1–6.

Schröpfer, G., Lorenz, G.L. and Krust, A. (2016) 'MEMS System-Level Modeling and Simulation in Smart Systems', *Smart Systems Integration and Simulation*. Switzerland, pp 145–168.

Schwarz, P. (1998) 'Microsystem CAD: From FEM to System Simulation', *Simulation of Semiconductor Processes and Devices*, pp. 141–148.

Sedaghat-Pisheh, H. and Rebeiz, G.M. (2010) 'Variable spring constant, high contact force RF MEMS switch', *Proceedings of IEEE MTT-S International Microwave Symposium Digest*, , pp. 304–307.

Sekikawa, J. and Kubono, T. (2004) 'Voltage-current characteristics of breaking arc at constant opening speed in the air', *IEEE Transactions on Components and Packaging Technologies*, 27(1), pp. 167–171.

Shalaby, M.M., Wang, Z., Chow, L.L., Jensen, B.D., Volakis, J.L., Kurabayashi, K. and Saitou, K. (2009) 'Robust design of RF-MEMS Cantilever switches using contact physics modeling', *IEEE Transactions on Industrial Electronics*, 56(4), pp. 1012–1021.

Shammas, N.Y.A. (1994) 'Combined conventional and solid-state device breakers', *Proceedings of IEE Colloquium on Power Semiconductor Devices*, pp. 5/1-5/5.

Shea, H.R. (2006) 'Reliability of MEMS for space applications', *Proceedings of SPIE*, 6111, pp. 61110A1-61110A10.

Shi, Y.-B., Yin, W.-Y., Mao, J.-F., Liu, P. and Liu, Q.H. (2009) 'Transient Electrothermal analysis of multilevel Interconnects in the presence of ESD pulses using the Nonlinear time-domain finite-element method', *IEEE Transactions on Electromagnetic Compatibility*, 51(3), pp. 774–783.

Shobak, H., Ghoneim, M., Boghdady, N.E., Halawa, S., Iskander, S. and Anis, M. (2011) 'Power gating of VLSI circuits using MEMS switches in low power applications', *ICM Proceeding*, pp. 1–5.

Shukla, A. and Demetriades, G.D. (2015) 'A survey on hybrid circuit-breaker Topologies', *IEEE Transactions on Power Delivery*, 30(2), pp. 627–641.

Sinha, R., Paredis, C., Liang, V.-C. and Khosla, P. (2001) Modeling and simulation methods for design of engineering systems, *Journal of Computing and Information Science in Engineering*, 1(1), pp. 84-91.

Slade, P.G. (2010) 'Opening electrical contacts: The transition from the molten metal bridge to the electric arc', *IEICE Transactions on Electronics*, E93-C(9), pp. 1380–1386.

Slade, P.G. (ed.) (2013) *Electrical Contacts: Principles and Applications*. CRC Press.

Slaughter, W.S. (2001) *The linearized theory of elasticity*. Boston, MA: Springer-Verlag New York.

Sokolowski, J.A. and Banks, C.M. (2010) *Modeling and simulation fundamentals: Theoretical underpinnings and practical domains*. United States: Somerset, New Jersey, U.S.A.: John Wiley & Sons.

Song, Y.-H. and Yoon, H.-B (2016) 'Micro and Nanoelectromechanical Contact Switches for Logic, Memory, and Power Applications', in Yoon, J.-B. (ed.) *Nano Devices and Circuit Techniques for Low-Energy Applications and Energy Harvesting*. Springer Netherlands, pp.65-115.

Song, Y.-H., Han, C.-H., Kim, M.-W., Lee, J.O. and Yoon, J.-B. (2012) 'An Electrostatically actuated stacked-electrode MEMS relay with a Levering and Torsional

spring for power applications’, *Journal of Microelectromechanical Systems*, 21(5), pp. 1209–1217.

Song, Y.-H., Kim, M.-W., Ahn, S.-J. and Yoon, J.-B. (2013) ‘Improvement of hot switching lifetime in MEMS DC switches using a drain voltage-sustaining capacitor’, *Proceedings of 17<sup>th</sup> International Conference on Solid-State Sensors, Actuators and Microsystems*, pp. 546-549.

Souchon, F., Reig, B. and Dieppedale, C. (2013) ‘Key improvements of the MEMS switch lifetime thanks to a dielectric-free design and contact reliability investigations in hot/cold switching operations’, *Proceedings of IEEE International Reliability Physics Symposium (IRPS)*, pp. 6B.2.1-6B.2.8.

Soul, S. and Dey, S. (2013) ‘Radio Frequency Micro Electro Mechanical Systems An Overview’, *Institute of smart structures and systems*, 2(2), pp. 27–75.

Spengen, W.M. van, Modliński, R., Puers, R. and Jourdain, A. (2010) ‘Failure Mechanisms in MEMS/NEMS Devices’, in *Springer Handbook of Nanotechnology*. Berlin Heidelberg: Springer, pp. 1761–1782.

Steeneken, P.G. and Wunnicke, O. (2007) ‘Performance limits of MEMS switches for power electronics’, *Proceedings of 24<sup>th</sup> International Symposium on Power Semiconductor Devices and ICs*, pp. 417–420.

Sterner, M., Roxhed, N., Stemm, G. and Oberhammer, J. (2010) ‘Static Zero-Power-Consumption Coplanar Waveguide embedded DC-to-RF metal-contact MEMS switches in Two-Port and Three-Port configuration’, *IEEE Transactions on Electron Devices*, 57(7), pp. 1659–1669.

Storozhev, D.A. and Surzhikov, S.T. (2015) ‘Numerical simulation of the two-dimensional structure of glow discharge in molecular nitrogen in light of vibrational kinetics’, *High Temperature*, 53(3), pp. 307–318.

Strong, F.W., Skinner, J.L. and Tien, N.C. (2008) 'Electrical discharge across micrometer-scale gaps for planar MEMS structures in air at atmospheric pressure', *Journal of Micromechanics and Microengineering*, 18(7), p. 075025.

Swingler, J. and McBride, J.W. (2008) 'Micro-Arcing and arc erosion Minimization using a DC hybrid switching device', *IEEE Transactions on Components and Packaging Technologies*, 31(2), pp. 425–430.

Tabari, M. and Yazdani, A. (2015) 'An energy management strategy for a DC distribution system for power system integration of plug-in electric vehicles', *IEEE Transactions on Smart Grid*, 7(2), pp. 659-668.

Takahashi, K., Sakaguchi, O., Yamamoto, T. and Inaoka, H. (2004) 'Investigation of contact materials in 42 VDC automotive relay', *Proceedings of 50<sup>th</sup> IEEE Holm Conference on Electrical Contacts*, pp. 22–27.

Theisen, P., Krstic, S. and Chen, C. (1986) '270-V Dc hybrid switch', *IEEE Transactions on Components, Hybrids, and Manufacturing Technology*, 9(1), pp. 97–100.

Timron, S.C. (2005) *Timron: TekNote newsletter: May 2001*. Available at: [http://www.timron-inc.com/teknote\\_May2001.html](http://www.timron-inc.com/teknote_May2001.html) (Accessed: 26 July 2016).

Tirumala, R. (2010), 'A mathematical model for the departure from Paschen's law at micrometer gaps using ion enhanced field emission', *AME60637: Ionization and ion transport final project paper*, pp. 1.1-1.6.

Toler, B.F., Coutu, R.A. and McBride, J.W. (2013) 'A review of micro-contact physics for microelectromechanical systems (MEMS) metal contact switches', *Journal of Micromechanics and Microengineering*, 23(10), p. 103001.

Torri, G.B., Hoof, C.V. and Bienstman, J. (2015) 'Co-Design of a MEMS-CMOS Autonomous Switched Oscillator', *Proceeding of Symposium on Design Test Integration and Packaging of MEMS and MOEMS*, pp. 1-4.

Tseng, K.-J., Wang, Y. and Vilathgamuwa, D.M. (1997) 'An experimentally verified hybrid Cassie-Mayr electric arc model for power electronics simulations', *IEEE Transactions on Power Electronics*, 12(3), pp. 429–436.

Van, C.W.A.R. (1978) *Protective Relays their theory and practice: Volume Two: V. 2*. United Kingdom: Chapman and Hall.

Vu, T.M., Prigent, G., Ruan, J. and Plana, R. (2012) 'Design and fabrication of RF-MEMS switch for V-band reconfigurable applications', *Progress In Electromagnetics Research B*, 39, pp. 301–318.

Wang, Z., Ma, H., Kong, G., Liu, Z., Geng, Y. and Wang, J. (2014) 'Decay modes of anode surface temperature after current Zero in vacuum arcs-part I: Experimental study', *IEEE Transactions on Plasma Science*, 42(5), pp. 1464–1473.

Wong, J.-E., Lang, J.H. and Schmidt, M.A. (2000) 'An electrostatically-actuated MEMS switches for power applications', Proceedings of the Thirteenth International Conference on Micro Electro Mechanical Systems, pp. 633–638.

Wood, R., Mahadevan, R., Dhuler, V., Dudley, B., Cowen, A., Hill, E., and Markus, K., (1998), MEMS microrelay, *Mechatronics*, 8, pp. 535-547.

Woodworth, A. (1981) 'High-voltage GTO Thyristors streamline power-switching circuits', *Electronics magazine*, pp. 129–131.

Xia, X., Guo, S., Zhao, W., Xu, P., Yu, H., Xu, T. and Li, X. (2014) 'Carboxyl functionalized gold nanoparticles in situ grown on reduced graphene oxide for micro-gravimetric ammonia sensing', *Sensors and Actuators B: Chemical*, 202, pp. 846–853.

Yang, Z., Lichtenwalner, D., Morris, A., Krim, J. and Kingon, A.I. (2010) 'Contact degradation in hot/cold operation of direct contact micro-switches', *Journal of Micromechanics and Microengineering*, 20(10), p. 105028.

Yeatman, E.M. (2007) 'Applications of MEMS in power sources and circuits', *Journal of Micromechanics and Microengineering*, 17(7), pp. S184–S188.



Yoichi, M. (2006) ‘Applications of piezoelectric Actuator’, *NEC Technical Journal*, 1(5), pp. 82-86.

Zavracky, P.M., Majumder, S. and McGruer, N.E. (1997) ‘Micromechanical switches fabricated using nickel surface micromachining’, *Journal of Microelectromechanical Systems*, 6(1), pp. 3–9.

Zavracky, P.M., McGruer, N.E., Morrison, R.H. and Potter, D. (1999) ‘Microswitches and microrelays with a view toward microwave applications’, *International Journal of RF and Microwave Computer-Aided Engineering*, 9(4), pp. 338–347.

Zhou, Y. (2008) Microjoining and Nanojoining, in *Woodhead Publishing Series in Welding and Other Joining Technologies*, United States.

Zhu, Y. and Espinosa, H.D. (2004) ‘Reliability of capacitive RF MEMS switches at high and low temperatures’, *International Journal of RF and Microwave Computer Aided Engineering*, 14(4), pp. 317–328.

Satish, B.S., Shetty, S., Shafiuddin, S. and Shahabuddin, S.K., ( 2012) ‘Nanorelays-Power Driver of the Next Decade’, *Proceedings of 2<sup>nd</sup> International Conference on Environment Science and Biotechnology*, 48(31), pp. 161-168.

## Appendix A

### Newton-Raphson Method

The equation is solved using Newton-Raphson method. This is a simple, iterative and powerful technique to solve the equations numerically.

$$f(V_b) = \left[ (\gamma_i + K e^{-E_{gd}/V_b}) \left( e^{Apg e^{(-Bpg_d/V_b)}} - 1 \right) \right] - 1 = 0 \quad (\text{A.1})$$

where  $f(V_b)$  be a well-behaved function, and  $r$  be a root of the equation  $f(V_b) = 0$ . Let  $V_{b_1}$  be initial guess of  $r$  and let  $r = V_{b_1} + h$ . Since the true root is  $r$ , and  $h = r - V_{b_1}$ , the number  $h$  measures how far the estimate  $V_{b_1}$  is from the truth. Since  $h$  is 'small,' tangent line approximation can be used to conclude that

$$0 = f(r) = f(V_{b_1} + h) \approx f(V_{b_1}) + hf'(V_{b_1}) \quad (\text{A.2})$$

And therefore, unless  $f'(V_{b_1})$  is close to 0,

$$h \approx -f(V_{b_1})/f'(V_{b_1}) \quad (\text{A.3})$$

It follows that

$$r = V_{b_1} + h \approx V_{b_1} - f(V_{b_1})/f'(V_{b_1}) \quad (\text{A.4})$$

Our new improved estimate  $V_{b_2}$  of  $r$  is therefore given by

$$V_{b_2} = V_{b_1} - f(V_{b_1})/f'(V_{b_1}) \quad (\text{A.5})$$

The next estimate  $V_{b_3}$  is obtained from  $V_{b_2}$

$$V_{b_3} = V_{b_2} - f(V_{b_2})/f'(V_{b_2}) \quad (\text{A.6})$$

If  $V_{b_n}$  is the current estimate, then the next estimate  $V_{b_{n+1}}$  is given by

$$V_{b_{n+1}} = V_{b_n} - f(V_{b_n})/f'(V_{b_n}) \quad (\text{A.7})$$

## Appendix B

### MATLAB M-file code for Breakdown Voltage

```
%%%%%%%%%%%%%%%%%%%%%%%%%%%%%%%%%%%%%%%%%%%%%%%%%%%%%%%%%%%%%%%%%%%%%%%%
%%%%%%%%%%%%%%%%%%%%%%%%%%%%%%%%%%%%%%%%%%%%%%%%%%%%%%%%%%%%%%%%%%%%%%%%
% Solution for an implicit equation
%
% \gamma*A*p*d* exp(-B*p*d/vb) + k*A*p*d* exp(-[(B*p*d)+D*d]/vb) = 1
%
% solve vb for given d

% Equ. 16
%f_old = (gamma+K*exp(-D*d/vb_old))*(exp(A*p*d*exp(-B*p*d/vb_old))-1)-1;

% Equ. 17
% f_old = gamma*A*p*d*exp(-B*p*d/vb_old) + K*A*p*d* exp(-(D*d+B*p*d)/vb_old)
- 1;
%
%%%%%%%%%%%%%%%%%%%%%%%%%%%%%%%%%%%%%%%%%%%%%%%%%%%%%%%%%%%%%%%%%%%%%%%%
%%%%%%%%%%%%%%%%%%%%%%%%%%%%%%%%%%%%%%%%%%%%%%%%%%%%%%%%%%%%%%%%%%%%%%%%

% for eq. 16 only
clear all;
clc;

A= 15;      % cm/torr
B= 365;     % volt/cm-torr
K= 10^7;    %
p= 760;     % 760 torr is one atm. pressure

phi= 4;     % ev
beta= 50;
gamma= 0.035;

D= 6.85*10^7*(phi^(3/2))/beta;

fac_micron = 10^(-4); % in microns (but multiple of cm here due to cgs units)

% % Test case
% d= 1*fac_micron; % vary this
% vb_old=50;      % guess
```

```

% prefac*dmax= gives maximum d insteps of prefac

prefac=0.5;
dmax=60;

d_vb=[];
%vb_old=50;

% vary d
for di=1:1:dmax

d= prefac*di*fac_micron;

vb_old=300; % have to use correct guess or may be by trial-error

% loop to start vb calculation for a given d
iter=1;
while(iter<30)

vb1=vb_old;
vb2=vb_old+1e-8;

f_old = (gamma+K*exp(-D*d/vb_old))*(exp(A*p*d*exp(-B*p*d/vb_old))-1)-1;
f1= (gamma+K*exp(-D*d/vb1))*(exp(A*p*d*exp(-B*p*d/vb1))-1)-1;
f2 = (gamma+K*exp(-D*d/vb2))*(exp(A*p*d*exp(-B*p*d/vb2))-1)-1;

dfdv= (f2-f1)/(vb2-vb1);

vb_new = vb_old - (f_old/dfdv);

% condition to terminate the loop
if(abs(vb_new-vb_old)<0.1)
vb_old=vb_new;
iter=100;
break;

else
iter=iter+1;
vb_old=vb_new; % re-assigning
end;
end;

d_vb=[d_vb,[prefac*di,vb_new]];

```

```

end;
d_vb

% plot d vs. Vb

beginx=0.14;
beginy=0.16;
xsize=0.84;
ysize=0.82;
figure6= figure('Color',[1 1 1]);
axes6 =
axes('fontsize',24,'LineWidth',1.5,'Parent',figure6,'Yscale','linear','XScale','linear',...
    'XTick',[0 5 10 15 20 25 30 35],'YTick',[0 200 400 600 800 1000],...
    'Position',[beginx beginy xsize ysize]);
box(axes6,'on');
hold(axes6,'all');
Position = [360 302 560 420];
set(gcf,'Position',Position);
xlabel('electrode gap, d (\mu m)','fontsize',24)
ylabel('break down voltage (V_b)','fontsize',24)

npoint=4;

h(1)=plot(d_vb(:,1),d_vb(:,2),'bo','linewidth',2.5,'markersize',npoint,'markerfacecolor','b','
    DisplayName','A_{bulk}');hold on

xlim([0 31])
ylim([0 1100])

```

## Appendix C

### Maxwell's Equation

The electric field distribution is obtained based on Maxwell's equations (Kara, Kalenderli, and Mardikyan, 2006)

$$\nabla \times E = 0 \quad (C.1)$$

$$\nabla \cdot D = \rho \quad (C.2)$$

$$D = \varepsilon E \quad (C.3)$$

$$E = -\nabla V \quad (C.4)$$

Poisson's scalar equation is obtained as

$$-\nabla \cdot (\varepsilon \nabla V) = -\nabla \cdot (\varepsilon_0 \varepsilon_r \nabla V) = \rho_{qs} \quad (C.5)$$

Where  $\varepsilon_0$  is the permittivity of free space,  $\varepsilon_r = \varepsilon_r(E, x, y, z)$  is the relative permittivity,  $E$  is the electric field,  $\rho_{qs}$  is the space charge density,  $D$  is the electric displacement,  $\varepsilon$  is the dielectric permittivity of the material. If the permittivity  $\varepsilon$  is constant such as in the isotropic dielectrics,

$$\Delta V = -\rho_{qs} / \varepsilon \quad (C.6)$$

For space charge free ( $\rho_{qs} = 0$ ) fields, field is expressed by Laplace's equation as

$$\Delta V = 0 \quad (C.7)$$

In rectangular coordinates (x, y, z), three-dimensional expression of Laplace's equation is

$$\frac{\partial^2 V}{\partial x^2} + \frac{\partial^2 V}{\partial y^2} + \frac{\partial^2 V}{\partial z^2} = 0 \quad (C.8)$$

$$C_{OFF} = Q_c / V \quad (C.9)$$

Where  $Q_c$  is the magnitude of charge stored in electrode.

Initial voltage  $V = 0V$ , Boundary condition: Top electrode:  $V = V_A$  (applied voltage),

Bottom electrode:  $V = 0V$

## Appendix D

### Linear Elasticity

The FEM simulation uses the following linear elasticity equations (Slaughter, 2001) to obtain the radius of the contact spot as a function of force

$$F = -\nabla \cdot \sigma \quad (D.1)$$

$$\sigma = s \quad (D.2)$$

$$s - S_0 = \overset{\dots}{C} : (\varepsilon - \varepsilon_0 - \varepsilon_{inel}) \quad (D.3)$$

$$\varepsilon = \frac{1}{2} \left[ (\nabla u)^T + \nabla u \right] \quad (D.4)$$

Where  $\sigma$  is the Cauchy stress tensor,  $\varepsilon$  is the infinitesimal strain tensor,  $u$  is the displacement,  $C$  fourth order stiffness tensor,  $F$  force per unit volume and  $\rho_m$  is the mass density.

Initial Force  $F = 0 \text{ Nm}$ , Boundary Condition: Top Electrode:  $F = F_A$  (applied voltage), Bottom Electrode:  $u = 0$  (Fixed)

## Appendix E

### Electrothermal Analysis

The Joule heating  $Q$  of the micro electrical contact is given as (Long, Liao, and Zhou, 2012)

$$Q = J \times E \quad (E.1)$$

$$E = -\nabla V_c \quad (E.2)$$

Where  $J = I_c / m^2$  is the current density,  $E$  the electric is field and is a gradient of contact voltage  $V_c$ .  $\nabla$  is the gradient operator and is determined by an electrical conductivity  $\sigma$  and current density  $J$  At steady state

$$\nabla(\sigma \cdot \nabla V - J) = 0 \quad (E.3)$$

The distribution of temperature is given by

$$\rho c \frac{\partial T}{\partial t} = \nabla \cdot (k_T \nabla T) + Q \quad (E.4)$$

Where  $k_T$  heat transfer coefficient, maximum anode temperature  $T$ , current density  $J = (\sigma \cdot \nabla V_c)$ .

Initial condition: At time  $t = 0s$ ,  $T_{(x,y,z,t)} = T_0$ , where  $T_0$  is the atmospheric temperature of 273K. Electric insulation  $nJ = 0$ , Initial Voltage  $V = 0V$ .

Boundary condition: Thermal insulation  $-n \cdot (-k \nabla T) = 0$  (All sides except left side of the anode), Current density  $J = J_A$  (Anode of the microelectrical contact)

## Appendix F

### 3D Heat transfer Equation

The anode temperature of an electrode is modeled by considering the 3D time-dependent heat equation in rectangular coordinates  $(x, y, z, t)$ . The anode temperature ( $T$ ) dependence on the thermo-physical coefficients of the electrode material (Carslaw and Jaeger, 1986)

$$\rho c \frac{\partial T}{\partial t} = \frac{\partial}{\partial x} \left( k \frac{\partial T}{\partial x} \right) + \frac{\partial}{\partial y} \left( k \frac{\partial T}{\partial y} \right) + \frac{\partial}{\partial z} \left( k \frac{\partial T}{\partial z} \right) \quad (F.1)$$

Where  $\rho_d$ ,  $c$  and  $k$  are the density, heat capacity and thermal conductivity of the electrode material respectively.  $x$ ,  $y$  and  $z$  are the axial coordinates and  $t$  is the time. The heat equation is simplified by considering the material to be isotropic and homogeneous. Thus

$$\rho c \frac{\partial T}{\partial t} = k \left( \frac{\partial^2 T}{\partial x^2} + \frac{\partial^2 T}{\partial y^2} + \frac{\partial^2 T}{\partial z^2} \right) \quad (F.2)$$

$$\rho c \frac{\partial T}{\partial t} = k \nabla^2 T \quad (F.3)$$

$$\nabla^2 T = \frac{\partial^2 T}{\partial x^2} + \frac{\partial^2 T}{\partial y^2} + \frac{\partial^2 T}{\partial z^2} \quad (F.4)$$

The Equation governing transient temperature is given by

$$\rho c_p \frac{\partial T}{\partial t} + \rho c_p u \cdot \nabla T = \nabla \cdot (k \nabla T) + Q \quad (F.5)$$



Boundary Conditions:

$$-n \cdot (-k \nabla T) = \frac{q}{A} \quad (\text{F.6})$$

Heat flux  $q = P$ , where  $P$  is in watts. (At the left side of the anode)

Thermal insulation  $-n \cdot (-k \nabla T) = 0$  (All sides except left side of the anode)

Initial condition:

At time  $t = 0s$ ,  $T_{(x,y,z,t)} = T_0$ , where  $T_0$  is the atmospheric temperature of 273K.

The Mesh structure of microelectrical contact is shown in Figure F.1.

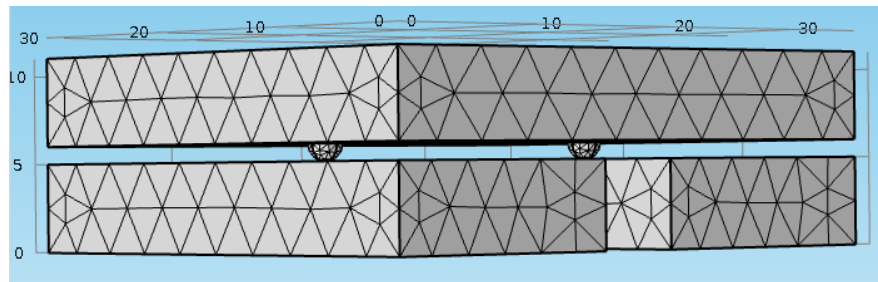


**Figure F.1:** Mesh structure of 3D microelectrical contact

# LIST OF PUBLICATIONS

## Journal Publications

1. Femi R, Agrawal A and Clement S. (2016) ‘An FEM study of the electrothermal properties of microelectrical contacts for application in the design of arcless switches’, *IEEE Transactions on Components, Packaging and Manufacturing Technology*, 6(3), pp. 407- 417.
2. Femi R, Agrawal A and Clement S. (2016) ‘An FEM study of the effect of temperature on the design of reliable micro electrical contact’, *Sensors & Transducers*, 202(7), pp. 51-58.
3. Femi R, Clement S, Agrawal A and Prince A. A. (2014) ‘Investigation of microelectromechanical switches for next generation DC power distribution system’, *International Journal of Emerging Electric Power Systems*, 15(6), pp. 591–605.
4. Femi R, Agrawal A and Clement S., ‘Effect of power, voltage and electric field on the design of arc-less micro electrical contact’, *Journal of Electrical Systems*. (Communicated)
5. Femi R, Agrawal A and Clement S., ‘Electromechanical modeling, design and analysis of scalable arcless micromechanical switch for power application’ *IEEE Transactions on Components, Packaging and Manufacturing Technology*. (Communicated)

## Conference Proceedings

1. Femi R, Clement S, Agrawal A and Prince A. A. (2014), ‘Effect of electric field on electrical breakdown arc behavior of micro contact gaps: A 3D

approach', *Proceedings of 6<sup>th</sup> IEEE PES Asia-Pacific Power and Energy Engineering conference, Hong Kong*, pp.1-6.

2. Femi R, Clement S, Agrawal A and Prince A. A. (2014), 'Cross tied array of electrostatically actuated micro-electromechanical switches for AC circuit breaking applications', *Proceedings of IEEE International Conference on Magnetism, Machines & Drives, Kerala*, pp.1-6.

### **Workshops Attended:**

1. INUP Familiarization workshop on "Nanofabrication Technologies", Centre of Nano Science and Engineering, Indian Institute of Science, Bangalore (CeNSE), May 21-23, 2014.
2. COMSOL Workshop, Birla Institute of Technology and Science, Pilani, K.K. Birla Goa Campus, 22<sup>nd</sup> February 2013.

### **Training Attended:**

1. INUP Hands-on Training on "MEMS Cantilever and Micro Nano Characterization Techniques", Centre of Nano Science and Engineering, Indian Institute of Science (CeNSE), Bangalore, May 21-29, 2015.
2. Hands-on training on "Coventor MEMS+", Birla Institute of Technology and Science, Pilani, K.K. Birla Goa Campus, 19<sup>th</sup> and 20<sup>nd</sup> August 2012.

### **Conferences Attended:**

1. 6<sup>th</sup> IEEE PES Asia-Pacific Power and Energy Engineering conference, Hong Kong, 7-10 December 2014.
2. IEEE International Conference on Magnetism, Machines & Drives, Kerala, 24-26 July 2014.

## **BRIEF BIOGRAPHY OF CANDIDATE**

**Femi R** received her Bachelor of Engineering degree in Electrical and Electronics Engineering, Master of Engineering in Power Electronics and Drives from Anna University, Chennai in 2006 and 2008 respectively. At present she is working as a lecturer in Birla Institute of Technology and Science, Pilani, K. K. Birla Goa Campus, India and also pursuing Ph.D. Her research interest includes power Electronics, microelectrical contacts and miniaturization of electrical components.

## **BRIEF BIOGRAPHY OF SUPERVISOR**

**Clement S** received Bachelor of Engineering in Mechanical Engineering from Bharathiar University in 1991, Master of Technology, Mechanical Engineering from Kerala University in 1998 and Ph.D. from Indian Institute of Technology Kanpur in 2006. He joined Birla Institute of Technology and Science, Pilani, K.K. Birla Goa campus in 2006. Currently, he is Associate Professor and the Head of the mechanical engineering department. His areas of research are thermodynamics, heat transfer, jet acoustic study and nanofluids.

## **BRIEF BIOGRAPHY OF CO-SUPERVISOR**

**Agrawal A** received Bachelor of Engineering, Masters of Engineering and Ph.D in Electronics Engineering from Government College of Engineering, Amravati, India in 1989, 1996 and 2009 respectively. She has 18 Years of teaching and research experience. Currently she is working as an Assistant Professor at Birla Institute of Technology and Science, Pilani, K.K.Birla Goa Campus, India. Her research interest includes Microelectronics, Instrumentation and VLSI.